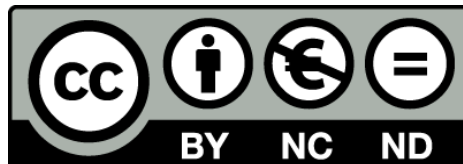


Galaxy evolution: A new version of the Besançon Galaxy Model constrained with Tycho data

Maria A. Czekaj



Aquesta tesi doctoral està subjecta a la llicència **Reconeixement- NoComercial – SenseObraDerivada 3.0. Espanya de Creative Commons.**

Esta tesis doctoral está sujeta a la licencia **Reconocimiento - NoComercial – SinObraDerivada 3.0. España de Creative Commons.**

This doctoral thesis is licensed under the **Creative Commons Attribution-NonCommercial-NoDerivs 3.0. Spain License.**

Universitat de Barcelona
Departament d'Astronomia i Meteorologia

**Galaxy evolution : A new version of the Besançon
Galaxy Model constrained with Tycho data**

Memòria presentada per
Maria A. Czekaj

per optar al grau de
Doctor per la Universitat de Barcelona

Barcelona, juliol de 2012

.

Programa de doctorat en Física

Galaxy evolution : A new version of the Besançon Galaxy Model constrained with Tycho data

Memòria presentada per
Maria A. Czekaj

per optar al grau de
Doctor per la Universitat de Barcelona

Directors de la tesi:

Dra. Annie C. Robin
Dra. Francesca Figueras
Dr. Xavier Luri

Acknowledgments

First of all I would like to thank to my supervisors Dra. Francesca Figueras, Dra. Annie C. Robin and Dr. Xavier Luri for the knowledge they have passed me, their time and support and for the four fruitful years of our collaboration. Special thanks to Annie for arranging my visits to Besançon and for being so hospitable that I could feel like at home. That place has a special energy and will always remain close to me. Special thanks to Francesca for her didactic approach, patience to explain and teach, and for her great support in the last weeks and days before delivering this thesis. And also special thanks to Xavier for helping me with the code development tasks and to manage heavy computations and also for showing me many times that the best solutions are the simplest ones and they can be found with calm.

Thanks to Dr. Jordi Torra, as Scientist in Charge for the Barcelona University in the ELSA Marie Curie Research Training Network, for accepting me as ELSA PhD fellow and giving me this great opportunity of studying in Barcelona.

Big thanks to all the members of the Gaia team and all colleagues at the University of Barcelona and as well to my colleagues at the Observatory of Besançon.

Special thanks to Dr. Misha Haywood and Dr. Luis Aguilar for their support and for sharing their knowledge and experience with me.

Many thanks to my teachers and professors in Poland for guiding me towards this PhD project, especially to prof. Sławomir Breiter for his support, humor and constant correspondence.

I would also like to thank to my wonderful family for their love and for being so close to me although physically I am always far away. Big thanks to all my friends and especially to Pat for making home with me here in Barcelona.

I dedicate the fruit of my work to people who have dedicated their lives to help other people. For that my very special thanks to maestro Son Kye-Dong, dear Babaji Jose and my Omi. They will probably never read this thesis, but a written word keeps its energy forever, so I would like to thank them for curing my body and inspiring the evolution of my inner self.

I dedicate the following words of Alan Wilson Watts to all my colleagues who at daily basis are struggling with the Universe:

“Through our eyes, the universe is perceiving itself. Through our ears, the universe is listening to its harmonies. We are the witnesses through which the universe becomes conscious of its glory, of its magnificence.”

I hope that one day we all will see the universes that are within us.

Resumen

Uno de los principales objetivos de la misión Gaia (ESA, lanzamiento previsto para otoño de 2013) es avanzar en el conocimiento del origen y la evolución de nuestra Galaxia. Para poder realizar una óptima explotación científica de los datos que aportará este satélite es fundamental disponer de modelos y códigos que permitan contrastar varias hipótesis y escenarios sobre los procesos de formación y evolución de las componentes galácticas. Cada una de estas componentes - disco delgado, disco grueso, halo y bulbo - viene caracterizada por una ley de densidad (recuentos estelares) y unas propiedades cinemáticas. Son también ingredientes fundamentales del modelo las propiedades de las estrellas, caracterizadas a partir de los modelos de evolución estelar y los modelos de atmósfera. Así también, un correcto tratamiento de los sistemas binarios en función de los parámetros físicos estelares es esencial en este tipo de estudios. Todo este conjunto de ingredientes permiten caracterizar las poblaciones estelares a nivel global y, de aquí, inferir la distribución total de masa y el potencial gravitacional galáctico.

Para abordar este objetivo, en la presente tesis doctoral nos hemos propuesto optimizar el llamado modelo de síntesis de poblaciones estelares de Besançon, cuya primera versión fue desarrollada por A. Robin en 1986. En particular nos hemos centrado en la componente del disco delgado de la Vía Láctea. Cuando iniciamos nuestro trabajo, hace ya cuatro años, dicho modelo simulaba el contenido estelar en una dirección del cielo dado usando los llamados diagramas de Hess. Para una población dada, este diagrama estaba fijado, y se calculaba imponiendo, de antemano, una función inicial de masa (IMF), una historia de formación estelar (SFR), un modelo de evolución estelar y una relación metalicidad-edad. Ello conllevaba que cualquier generación de un catálogo estelar mediante dicha versión mantuviese fijos ingredientes tan fundamentales y poco conocidos como son la IMF o la SFR, parámetros que Gaia deberá redefinir en la próxima década.

Esta tesis ofrece una nueva versión del modelo de Besançon. Hemos diseñado, desarrollado, implementado y testado una nueva estructura de generación de las estrellas del disco delgado, una estructura que permite, mediante la comparación de los datos observados y los generados, encontrar la mejor combinación de IMF y SFR que ajusta a las observaciones. Como se detalla en el capítulo 2, el código que presentamos permite imponer la autoconsistencia dinámica en el proceso de generación estelar. Esta se realiza siguiendo los modelos propuestos por Bienayme et al. (1987). Para cada nuevo escenario de evolución (IMF, SFR, modelos de evolución estelar, ...) se recalcula el potencial galáctico y de aquí las leyes de densidad que nos per-

mitirán generar un catálogo dinámicamente autoconsistente. La segunda aportación importante de esta tesis es la capacidad del nuevo modelo de Besançon de generar sistemas binarios. Hasta la fecha, dicho modelo, disponible en la web y de uso libre para toda la comunidad internacional, solo permitía la generación de estrellas individuales (Robin et al. 2003). Si bien el simulador de Gaia, cuya descripción del contenido estelar ha sido recientemente publicada en Robin et al. (2012), incluía ya la generación de sistemas binarios, tampoco contemplaba algo tan fundamental como es la autoconsistencia dinámica, es decir la conservación de la masa total observada en el entorno solar. En la versión que se presenta en esta tesis doctoral este tema ha sido tratado y testeado con rigor de forma que podemos afirmar que el contenido estelar que genera el nuevo modelo mantiene las restricciones de la densidad local observada, restricciones que se derivan de la función de luminosidad observada en el entorno solar.

Los capítulos 2 y 3 incluyen una descripción detallada de la nueva estructura del código, de las actualizaciones de todos los ingredientes del modelo de acuerdo con los avances en los últimos diez años en astrofísica galáctica y evolución estelar, así como de los procesos de generación de sistemas binarios. En el capítulo 4 discutimos los dos elementos observacionales clave para el ajuste entre modelo y observación: la función de luminosidad observada en el entorno solar y el catálogo de Tycho, ambas aportaciones relevantes de la misión Hipparcos de la ESA (Perryman et al., 1997). Una vez desarrolladas las herramientas que permiten este ajuste entre modelo y observables (ver capítulo 4), en el capítulo 5 pasamos a seleccionar los escenarios de evolución estelar y galáctica que permiten un mejor ajuste del modelo a los datos observacionales. Dicho capítulo muestra otro de los logros de la presente tesis doctoral: por primera vez hemos conseguido un ajuste aceptable a los recuentos estelares y distribuciones de color observados por Hipparcos hasta magnitud visible aparente 11. En este capítulo mostramos los efectos que resultan de variar cada uno de los ingredientes básicos del modelo, desde el cambio de los modelos de atmósfera o los modelos de evolución estelar al uso de uno u otro modelo de extinción interestelar. También, como ejemplo, en esta sección se han analizado los efectos en los recuentos estelares derivados de imponer una u otra masa dinámica del sistema galáctico. En conclusión, esta tesis nos proporciona una visión global no solo de los ingredientes que componen el puzzle del disco delgado de nuestra Galaxia sino también de los efectos que cada uno de estos produce en la componente estelar que observamos en una dirección del cielo dada.

Para concluir, queremos mencionar que el código que aquí presentamos supone una mejora substancial al modelo de síntesis de poblaciones estelares más usado por la comunidad astronómica internacional. El ajuste de sus ingredientes básicos al catálogo Tycho aporta resultados tan relevantes como es la confirmación de que el ritmo de formación estelar en el disco galáctico no ha sido constante sino decreciente desde los inicios de la formación de esta estructura. Sin duda, la futura generación de catálogos sintéticos a partir de este código y su comparación con catálogos estelares más profundos como GSC2 o PanStars supondrá un paso significativo hacia el conocimiento de los procesos de evolución de los discos galácticos.

Abstract

The construction of a dynamical model of the Milky Way from the upcoming Gaia data will require a complex comparison between models and data in the space of the observables. To be ready for this challenge, in this PhD thesis, we have optimized the Besançon stellar population synthesis model. The new version of the model has been constructed and ingredients as critical as the IMF, the SFR, the binary fraction, the age-metallicity relation and the age-kinematic relation can now be fitted to the observed data. The optimization includes also the use of most updated evolutionary tracks and model atmospheres. Various scenarios for those parameters have been checked against the Tycho-2 data.

The author was supported as an Early Stage Researcher of the Marie Curie Research Training Network "European Leadership in Space Astrometry" (ELSA) MRTN-CT-2006-033481 of the VIth Framerwork Programm - European Community and the MICINN (Spanish Ministry of Science and Innovation) - FEDER through grant AYA2009-14648-C02-01. This thesis has been carried out at the Department d'Astronomia i Meteorologia (Universitat de Barcelona) and the Observatoire de Besançon (France). This study was partially supported by the Gaia Research for European Astronomy Training (GREAT) 08-RNP-118 European Science Foundation (European RNP FP7) and the MICINN - AYA2009-08488-E/AYA.

Contents

1	Introduction	15
2	The Besançon Galaxy Model - the code	19
2.1	The Besançon Galaxy Model up to now	19
2.2	A new approach to the BGM	26
2.2.1	The overall structure	26
2.2.2	Determination of the mass model	30
2.3	The code and its implementation	38
2.3.1	The thin disc treatment	38
2.3.2	Binarity	45
2.4	New processing modes	46
3	The update of model's inputs	51
3.1	The Initial Mass Function	51
3.2	The Star Formation Rate	56
3.3	Evolutionary tracks sets	59
3.4	Binarity	63
3.5	Atmosphere models	63
3.6	Age-metallicity relation	65
3.7	Dynamical mass and age-velocity relation	68
3.7.1	Dynamical mass	68
3.7.2	Age-velocity dispersion relation	69
4	Observables and tools	71
4.1	Observables	71
4.1.1	The local luminosity function	71
4.1.2	The Tycho-2 Catalogue	73
4.2	Tools	78
4.2.1	The processing pipeline - whole sky simulations	78

4.2.2	WEKA	79
4.2.3	Post-processing	80
5	Results	81
5.1	The old model vs. Tycho-2 vs. new model	82
5.2	The impact of the model's inputs on the results	86
5.2.1	The local stellar mass density	88
5.2.2	The IMF and the SFR	99
5.2.3	Binarity	110
5.2.4	The age of the thin disc	112
5.2.5	The thick disc	114
5.2.6	Extinction model	116
5.2.7	Atmosphere models	118
5.2.8	Evolutionary tracks	120
5.2.9	Age-metallicity relation	122
5.2.10	The total local dynamical mass	124
5.2.11	Age-velocity relation	127
5.2.12	Radial scale length	130
5.3	Looking for the best fit with Tycho-2 data	133
6	Conclusions	141
7	Bibliography	145
A	Appendix A: Constant vs. decreasing SFR	153
B	Appendix B: Kroupa-Haywood IMF vs. Tycho-2	163

Chapter 1

Introduction

The understanding of the origin and evolution of the Milky Way is one of the primary goals of the Gaia mission (ESA, launch autumn 2013). In order to study and analyse fully the Gaia data it will be useful to have a Galaxy model able to test various hypothesis and scenarios of galaxy formation and evolution. Kinematic and star count data, together with the physical parameters of the stars - ages and metallicities-, will allow to characterize our galaxy's populations and, from that, the overall Galactic gravitational potential. One of the promising procedures to reach such goal is to optimize the present Population Synthesis models (Robin et al. (2003)) by fitting, through robust statistical techniques, the large and small scale structure and kinematics parameters that best will reproduce Gaia data. This PhD thesis was focused on the optimization of the structure parameters of the Milky Way Galactic disc. We aim to improve the Besançon Galaxy Model and then by comparing the simulations to real data study the process of Galaxy evolution.

The Besançon Galaxy Model is a stellar population synthesis model, built over the last two decades in Besançon (Robin and Crézé (1986); Robin et al. (2003)). Until now the star production process in that model was based on the drawing from the so called Hess diagrams. Each Galaxy population had one such a diagram, which was calculated once given a particular Initial Mass Function (IMF), Star Formation Rate (SFR), evolutionary tracks and age-metallicity relation and since then remained fixed in the model (more detailed explanation in section 2.1). As that feature was not enabling to test any other scenario of Galaxy evolution, because none of the evolutionary parameters could be modified, it was one of the biggest weaknesses of the Besançon Galaxy Model. It has served us as a motivation to dedicate this PhD project to the construction of a new version of the model, which would be able to handle variations of the SFR, IMF, evolutionary tracks, atmosphere models among others (see chapters 3 and 5). When the evolutionary parameters are being changed one must repeat the process of accomplishing the dynamical self-consistency of the model as described in Bienayme et al. (1987). For that we have recalculated the Galactic gravitational potential for all new evolutionary scenarios, which have been tested. The second very important improvement of the model, which is delivered in this thesis, is the implementation of the stellar binarity. That is, the new version of Besançon Galaxy Model presented here is not any more a single star generator, but it considers binary systems maintaining constraints on the local mass density. This is an important change since binaries can account for about 50 % of the total stellar content of the Milky Way.

Once we had developed the tool our first interest was to test several possible scenarios of IMF

and SFR in the Solar Neighborhood and in the identification of those which best reproduce the Local Luminosity Function and Tycho-2 data, the two most important observational constraints available at present. The Tycho-2 catalogue was chosen to be our primary data set serving us for intensive comparisons with simulations.

The Besançon Galaxy Model was intensively tested against data of various types during the last two decades, however up to now it was most usually done for some particular regions or towards specific directions along the line of sight, where model and data were compared up to faint magnitudes. The model was also compared with all sky surveys, such as GSC2 and 2MASS, but the bright stars such as A and F type stars were never deeply studied. In this PhD project we have accomplished this unprecedented task using the new version of Besançon Galaxy Model, namely we have performed whole sky comparisons for a magnitude limited sample in order to study the bright stars. The Tycho-2 catalogue turned out to be an ideal sample for that task due to its two important advantages, the homogeneity and completeness until $V_T \sim 11$ mag.

Different techniques and strategies were designed and applied when comparing the simulated and the real data. We have looked at small and specific Galactic directions and also performed general comparisons with a global sky coverage. In order to increase the efficiency of numerous simulations and comparisons, a processing pipeline based on C, Java and scripting programming languages has been developed and applied. It is a fully automated, portable and robust tool, allowing to split the work across several computational units. The cluster of the Departament d'Astronomia i Meteorologia (32 nodes) has been used for that purpose.

We present the comparison of the new release of the Besançon Galaxy Model with Tycho-2 data, however, the tool is ready and in the near future it can be compared with other data sets available at present. The same processing pipeline can be applied in those comparisons.

Summarizing, we expect that our work on the improvement of the model and of the methods of comparisons with large data sets can contribute to the scientific community such that we will be more prepared for an optimum exploitation of the huge amount of data that Gaia will provide. The aims of our project are depicted in Fig. 1.1.

To be prepared for an optimum exploitation of the huge amount of Gaia data.

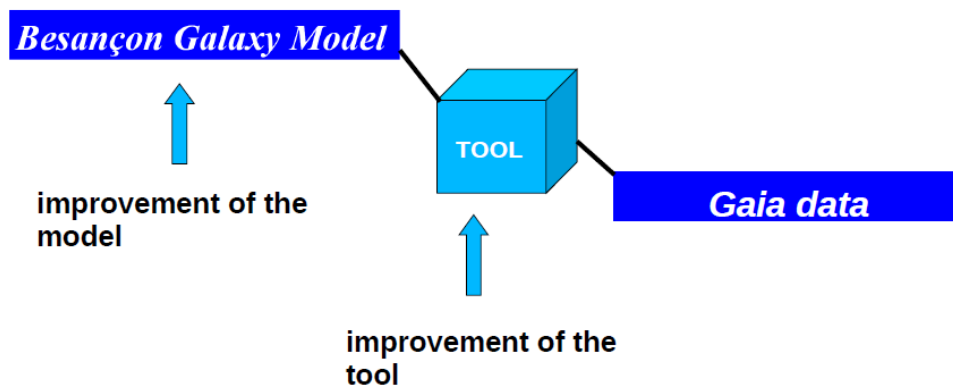


Figure 1.1: The graphical representation of our aims: the improvement of the Besançon Galaxy Model and the construction and improvement of the tool which serves for the comparison with large data sets.

Chapter 2

The Besançon Galaxy Model - the code

2.1 The Besançon Galaxy Model up to now

The Galaxy Model developed over more than two decades in Besançon is based on the approach of stellar population synthesis and predictions of star counts towards different lines of sight. It is described at length in a series of articles out of which Robin and Crézé (1986) is the first one and Robin et al. (2003) presents the last published release of the model. Since that last release there have been several changes applied in the model and the log of them is presented online on the official web site of the model, see BGM website.

It was constructed by putting the knowledge on the formation and evolution of our Galaxy together with theories of stellar formation and evolution, stellar atmosphere models and dynamical constraints. The idea is to start with some a priori knowledge or assumptions, model the Galaxy and then by performing vast comparisons with the observational data deduce the real nature of several parameters involved in the Galaxy modelling. This powerful testing tool allows comparisons with large photometric (multi-wavelength) and astrometric catalogues, thus providing new constraints to our knowledge of the structure and kinematics of our Galaxy.

The organization of the model is such that the stellar ages are the link between the kinematics and dynamics and the stellar evolution. A model of Galaxy evolution is used to obtain the age distribution in the Solar Neighborhood (SN). An important and original feature of the Besançon Galaxy Model is its large degree of approximation of dynamical self-consistency, see section 2.2.2 and Bienayme et al. (1987). It is achieved through the Jeans equation in such a way that the scale heights of the Galactic disc population are constrained by their velocity dispersions and the potential of the Galaxy mass model. The model is able to produce the kinematic parameters of stars as proper motions and radial velocities. The interstellar extinction distribution throughout the disc is also included.

The basic concept underlying the model predicting the Galactic star counts is the fundamental equation of stellar statistics:

$$A(m) = \int_r \phi(M)\rho(r)r^2\omega dr, \quad (2.1)$$

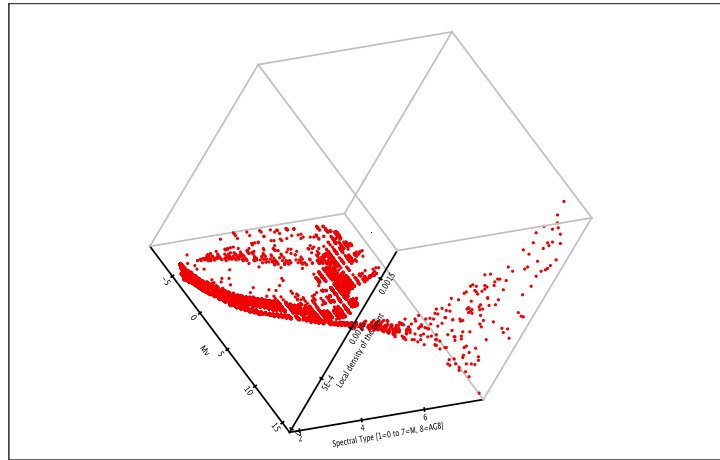
where $A(m)$ is the number of stars with apparent magnitude m found inside of the solid angle ω , M is the absolute magnitude and r the heliocentric distance. Equation 2.1 is the product of the density law $\rho(r)$ and the luminosity function $\phi(M)$. The scheme of the synthetic approach is to first make assumptions on both functions and then by trial and error tune them, such that they reproduce the $A(m)$ best. The luminosity function as well as the density law are distinct for each population and for that Eq. 2.1 has to be treated separately for each component. In general the synthesis of Galaxy populations is a process of gradual transformation of the mass of the gas cloud into stars. This process of star creation is expressed by the means of the IMF and SFR. Since their birth, stars evolve on the evolutionary tracks and populate the HR diagram, leading to the present-day state of the Milky Way. Nowadays, the luminosity function and the chemical composition of the stars are known only for the Solar Neighborhood. In order to extrapolate those distributions to any position within the Galaxy, one must provide the model with the density laws.

In the model it is assumed that stars belong to four basic populations: the thin disc, the thick disc, the stellar halo and the bulge. Additionally, the thin disc is divided into seven subpopulations of different ages ranging from 0 to 10 Gyr. Each of the four main components is characterized by its own SFR, IMF, age range, evolutionary tracks, stellar atmosphere models, kinematics, age-metallicity relation and density laws. The white dwarfs population is taken into account separately, nevertheless it is included in the dynamical considerations.

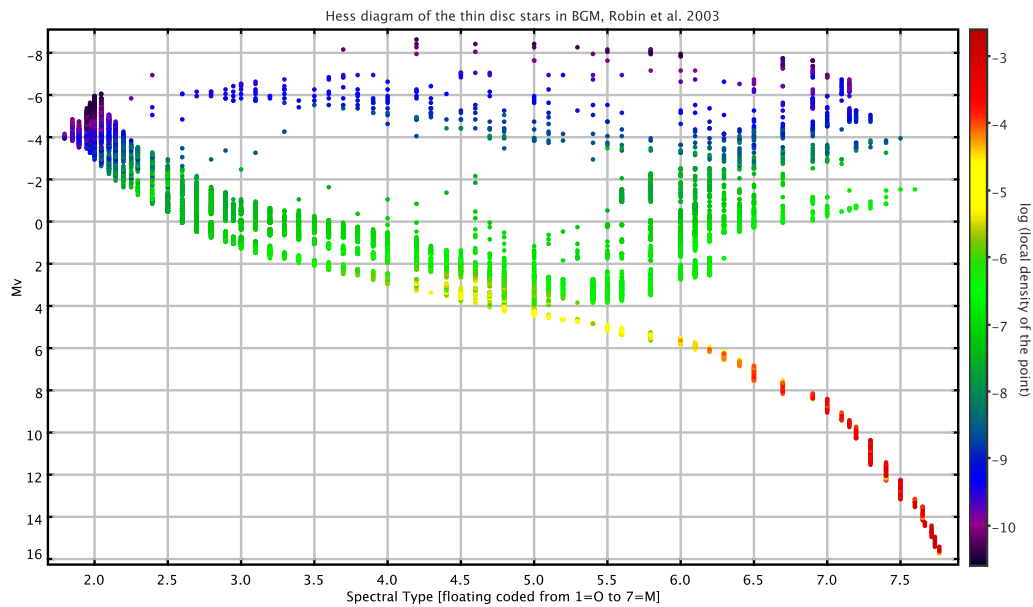
Summarizing the main model's inputs are:

- star formation rate
- initial mass function
- evolutionary tracks
- chemical evolution
- atmosphere models
- density laws
- interstellar extinction model.

As already explained, the parameters describing these inputs are specified for each population separately. In the Besançon Galaxy Model presented in Robin et al. (2003) the scenarios of the thin disc IMF and SFR as well as the evolutionary tracks sets are fixed. In the work of Haywood et al. (1997b) various values for the disc evolution parameters were tested by fitting to the observational data. Those which provided them best fit, were used to compute the stellar content at each epoch and saved in the form of so called "Hess diagram", which serves as the input for the Besançon Galaxy Model. That diagram could be explained as the three dimensional HR diagram, where every point (M_v ; Spectral type) is associated with a density of stars existing there ($stars/pc^3$) or even a multidimensional color-magnitude diagram, because the density value of each point is normalized to one and split over the seven age bins referring to seven disc subcomponents. Haywood (1994) gives an excellent explanation of how such a distribution can be obtained for the Galactic disc once the SFR, IMF and the evolutionary tracks are defined. The graphical representation of the thin disc Hess diagram used in Robin et al. (2003) is showed in Fig. 2.1.



a)



b)

Figure 2.1: The Hess Diagram of the thin disc population used in the Besançon Galaxy model, A. Robin et al.(2003). a) A three dimensional picture of the Hess diagram in question. b) On the x axis we have the spectral type as a floating number coded from 1=O to 7=M. The y axis corresponds to absolute visual magnitude M_V , while z is the logarithm of the local density of a given point. The diagram consists of 9288 points which have been computed from standard inputs: the IMF, SFR and evolutionary tracks (see M. Haywood et al.(1997)).

	Age (Gyr)	$[\frac{Fe}{H}]$ (dex)	$\frac{d[Fe/H]}{dR}$	IMF	SFR
Disc	0-0.15	0.01 ± 0.12	-0.07	$dn/dm \propto m^{-\alpha}$ $\alpha = 1.6$ for $m < 1M_{\odot}$ $\alpha = 3.0$ for $m > 1M_{\odot}$	constant
	0.15-1	0.03 ± 0.12			
	1-2	0.03 ± 0.10			
	2-3	0.01 ± 0.11			
	3-5	-0.07 ± 0.18			
	5-7	-0.14 ± 0.17			
	7-10	-0.37 ± 0.20			
Thick disc	11	-0.78 ± 0.30	0.00	$dn/dm \propto m^{-0.5}$	one burst
Stellar halo	14	-1.78 ± 0.50	0.00	$dn/dm \propto m^{-0.5}$	one burst
Bulge	10	0.00 ± 0.40	0.00	$dn/dm \propto m^{-2.35}$ for $m > 0.7M_{\odot}$	one burst

Figure 2.2: Table 1 from Robin et al. (2003), which gives the age, the mean metallicity $[\frac{Fe}{H}]$ and the mean dispersion about the mean, the radial metallicity gradient (dex/kpc), initial mass function (IMF), and the star formation rate (SFR) for all stellar components.

The SFR and IMF formulas, which served to calculate that multidimensional color-magnitude diagram are listed in the Table 1 of Robin et al. (2003), which we reproduce in Fig. 2.2. As one can notice, a two slope IMF and a constant SFR was assumed for the thin disc. We find there also the ages, metallicities and radial metallicity gradients for all components. The values of the age-metallicity relation have been updated since that time. For the thin disc the age-metallicity relation from Haywood (2006) is used. The mean metallicity of the thick disc was taken from Bensby et al. (2007) and Fuhrmann (2011), while for halo the values from Ž. Ivezić et al. (2008).

We show the Eq.2.1 in a slightly different form, which explains better the general scheme of the BGM:

$$A(m) = \sum_{i=1}^n \int_0^{r_{max}} \phi(M_v, Teff, Age) \rho_i(R, \theta, z, Age) \omega r^2 dr, \quad (2.2)$$

where n indicates the Galaxy population. The information on the luminosity function $\phi(M_v, Teff, Age)$ comes from the Hess diagram. If we express the solid angle in terms of the Galactic coordinates we get:

$$A(m) = \sum_{i=1}^n \int_0^{r_{max}} \int_b \int_l \phi_i(M_v, Teff, Age) \rho_i(R, \theta, z, Age) r^2 \cos(b) dl db dr. \quad (2.3)$$

It holds the main idea of the model, which is to provide the number of stars in a given direction of the sky and up to a specified distance r_{max} , by extending the knowledge gathered in the SN to the remote parts of our Galaxy. The summation of all Galactic components is done ($n = 4$). We see that the Hess diagram provides us the information on the $\phi(M_v, Teff, Age)$, the number of objects per cubic parsec in a given cell of the HR diagram, and in a given age bin, in the Sun's vicinity and assumed to be the same for all the Galactic thin disc. The density has to be treated twofold, by combining the information on the local density and the density laws suitable for each Galactic population. The local mass density in stars in the SN is derived

	Age (Gyr)	ρ_0 ($M_{\odot}\text{pc}^{-3}$)	σ_W (km s^{-1})	ϵ
Disc	0-0.15	4.0×10^{-3}	6	0.0140
	0.15-1	7.9×10^{-3}	8	0.0268
	1-2	6.2×10^{-3}	10	0.0375
	2-3	4.0×10^{-3}	13.2	0.0551
	3-5	5.8×10^{-3}	15.8	0.0696
	5-7	4.9×10^{-3}	17.4	0.0785
	7-10	6.6×10^{-3}	17.5	0.0791
	WD	3.96×10^{-3}		
Thick disc	11	1.34×10^{-3}		
	WD	3.04×10^{-4}		
Stellar halo	14	9.32×10^{-6}		0.76
Dark matter halo		9.9×10^{-3}		1.
ISM		2.1×10^{-2}		

Figure 2.3: Table 2 from Robin et al. (2003). The local density for different model components. In the third column the W -velocity dispersion σ_W (from Gómez et al. (1997)) used in the process of approximating the dynamical self-consistency and in the fourth column values of ϵ , which are the disc axis ratios resulting from that process (ϵ is defined in Eq. 2.6).

from the observations (Crézé et al. (1998); van Leeuwen (2007)) and in the BGM this value is used together with other mass components (ISM, stellar halo, bulge and dark halo) to calculate the Galactic potential, and from that, to constrain the scale heights of the disc via the Jeans equation up to second order in the moments of the velocity distribution. This is an iterative process, which approximates the dynamical consistency (see 2.2.2). For the values of the local mass density assumed for each stellar component see Table 2 of Robin et al. (2003), which is copied here in Fig. 2.3. Once the density values in the solar neighborhood are fixed one can derive the density elsewhere in the Galaxy by providing a suitable mathematical expression. The list of the density laws and their associated parameters chosen for the four Galactic populations of BGM can be found in Fig. 2.4, which is Robin et al. (2003) Table 3. The density model of the bulge has been recently updated in Robin et al. (2012).

As the basic concepts of the stellar population synthesis have been explained together with the main inputs of the BGM, one can easily understand the structure of the model presented in the flowchart in Fig. 2.6 (source Robin and Crézé (1986)). The outermost loop is the distance loop and a simple integration along the line of sight is performed. Then successively each population is treated. At each distance step the volume element is calculated and the corresponding Hess diagram is scanned in order to get a number of stars together with their intrinsic parameters at that particular position. Subsequently, the metallicity is drawn and the observable values are derived. The extinction at each volume element is calculated according to the specified law and the corrections for extinction are done. The model permits to use a simple Einasto extinction law, Drimmel and Spergel (2001) extinction model or a 3D model from Marshall et al. (2006). If needed, the observational errors are computed. The output of the simulations can be: multi-dimensional histograms of intrinsic star properties or observable properties, a catalog of pseudo observations, or the integrated luminosity in a specified photometric band. The thin disc pop-

density law		
Disc	$\rho_0/d_0 \times \{\exp(-(a/h_{R_+})^2) - \exp(-(a/h_{R_-})^2)\}$ with $h_{R_+} = 5000$ pc, $h_{R_-} = 3000$ pc	if age ≤ 0.15 Gyr
	$\rho_0/d_0 \times \{\exp(-(0.5^2 + a^2/h_{R_+}^2)^{1/2}) - \exp(-(0.5^2 + a^2/h_{R_-}^2)^{1/2})\}$ with $h_{R_+} = 2530$ pc, $h_{R_-} = 1320$ pc	if age > 0.15 Gyr
Thick disc	$\rho_0/d_0 \times \exp(-\frac{R-R_\odot}{h_R}) \times (1 - \frac{1/h_z}{x_l \times (2+x_l/h_z)} \times z^2)$ $\rho_0 \times \exp(-\frac{R-R_\odot}{h_R}) \times \frac{\exp(x_l/h_z)}{1+x_l/2h_z} \exp(-\frac{ z }{h_z})$ with $h_R = 2500$ pc, $h_z = 800$ pc	if $ z \leq x_l$, $x_l=400$ pc if $ z > x_l$
Spheroid	$\rho_0/d_0 \times (\frac{a_c}{R_\odot})^{-2.44}$ $\rho_0 \times (\frac{a}{R_\odot})^{-2.44}$	if $a \leq a_c$, $a_c = 500$ pc if $a > a_c$
Bulge	$N \times \exp(-0.5 \times r_s^2)$ $N \times \exp(-0.5 \times r_s^2) \times \exp(-0.5(\frac{\sqrt{x^2+y^2}-R_c}{0.5})^2)$ with $r_s^2 = \sqrt{[(\frac{x}{x_0})^2 + (\frac{y}{y_0})^2]^2 + (\frac{z}{z_0})^4}$	$\sqrt{x^2+y^2} < R_c$ $\sqrt{x^2+y^2} > R_c$
ISM	$\rho_0 \times \exp(-\frac{R-R_\odot}{h_R}) \times \exp(-\frac{ z }{h_z})$ with $h_R = 4500$ pc, $h_z = 140$ pc	
Dark halo	$\frac{\rho_c}{(1+(a/R_c)^2)}$ with $R_c = 2697$ pc and $\rho_c = 0.1079$	

Figure 2.4: Table 3 from Robin et al. (2003). Density laws and associated parameters for all model components. The density model of the bulge has been updated in Robin et al. (2012).

ulation includes the warp and flare structures, which are discussed in Reylé et al. (2009). The Gómez et al. (1997) velocity ellipsoid is applied for the disc. The asymmetric drift is included in the considerations, but not the vertex deviation. The summary of kinematic parameters for each population is given in the Table 4 of Robin et al. (2003), which we present in Fig. 2.5.

	Age (Gyr)	σ_U (km s ⁻¹)	σ_V (km s ⁻¹)	σ_W (km s ⁻¹)	V_{ad} (km s ⁻¹)	$\frac{d \ln(\sigma_U^2)}{dR}$
Disc	0-0.15	16.7	10.8	6	3.5	-2×10^{-1}
	0.15-1	19.8	12.8	8	3.1	
	1-2	27.2	17.6	10	5.8	
	2-3	30.2	19.5	13.2	7.3	
	3-5	36.7	23.7	15.8	10.8	
	5-7	43.1	27.8	17.4	14.8	
	7-10	43.1	27.8	17.5	14.8	
Thick disc		67	51	42	53	0
Spheroid		131	106	85	226	0
Bulge		113	115	100	79	0

Figure 2.5: Table 4 from Robin et al. (2003). Velocity dispersions, asymmetric drift at the solar position and velocity dispersion gradient.

An important feature of the model up to now is that it produces single stars only, no binary or multiple stars are produced.

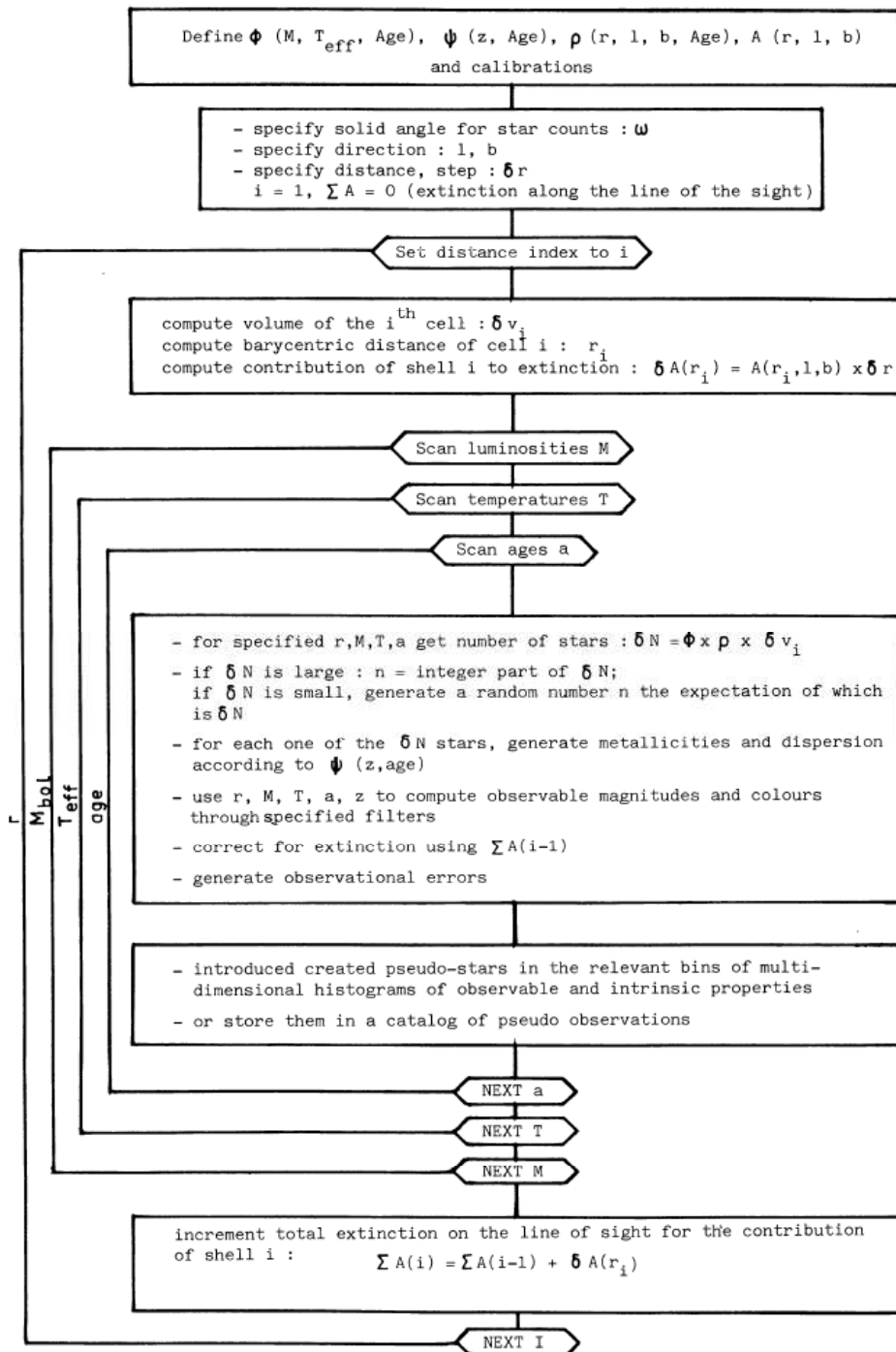


Figure 2.6: Fig. 1 from Robin and Crézé (1986). Flowchart of the algorithm.

2.2 A new approach to the BGM

In our work we have focused on the Galactic thin disc, thus the reasoning presented here concerns the treatment of that population only. For the other three components, the bulge, the thick disc and the halo, we have maintained the scheme of the old model presented in Fig. 2.6. For those three populations a single burst was assumed and the corresponding Hess diagrams were made from single isochrones. In this research we have kept fixed them without applying any changes.

2.2.1 The overall structure

The general diagram of the new model's `mevol` (code model name) constitution can be found in Fig. 2.7. Before explaining in detail its ingredients, let us shortly discuss the scheme of the star production history.

The BGM presented here is based on the new approach to the star production philosophy. As explained in the section 2.1, our starting point was a model which is based on fixed Hess diagrams for each population (Robin et al. (2003)). Its internal loop is the summation on the Hess diagram. Our main goal was getting rid of those fixed Hess diagrams and turning the IMF, SFR and evolutionary tracks into the free user-specified parameters. That meant constructing a model which takes the scenario of star creation process throughout the age of the Galactic disc, the IMF, SFR and age-metallicity relation, and using some particular sets of evolutionary tracks, extract from them the necessary information during the run time and create stars, reject the dead ones and save those which can be observed at present. In practice, to build a Galaxy from the fundamental building-blocks, we had to reconstruct the previous model and apply important changes in the code arrangement. That required to understand well the underlying relations between all mentioned components.

Consider Fig. 2.8. This is the graphical representation of the relationships between the theoretical IMF, SFR, evolutionary tracks and the observed LF (luminosity function) and the PDMF (present-day mass function).

The stellar birthrate function $b(m, t)dm dt$ (see Tinsley (1976)) gives the mathematical description of the star production process. It defines the number of disc stars born in the mass interval $(m, m + dm)$ in the interval of time $(t, t + dt)$. Knowing it precisely we could tell much about the evolution of the Milky Way. However, the nature of that function is unknown and due to the dependency on both variables, the time and the mass, the stellar birthrate function is not very convenient to work with. For that it is customary to replace it with the product of two independent functions, time and mass. This separation is only valid when one assumes that the ratio of stars being born in a given mass interval to those born at other mass value, is fixed in time.

The field star IMF, $\phi(m)$, is the total number of stars at their birth per unit mass. In other words one could say that it specifies the distribution of mass of a freshly formed stellar population (Binney and Merrifield (1998)). If the IMF is constant in time, as commonly assumed, its shape at any time is the same as the IMF of all stars ever formed. Thus it is also common to define the IMF simply as the mass distribution of a given population of stars. While the Star Formation Rate, $\Psi(t)$ represents the total mass of stars born per unit time per unit mass of Galaxy. Following that notation the stellar creation function can be converted to

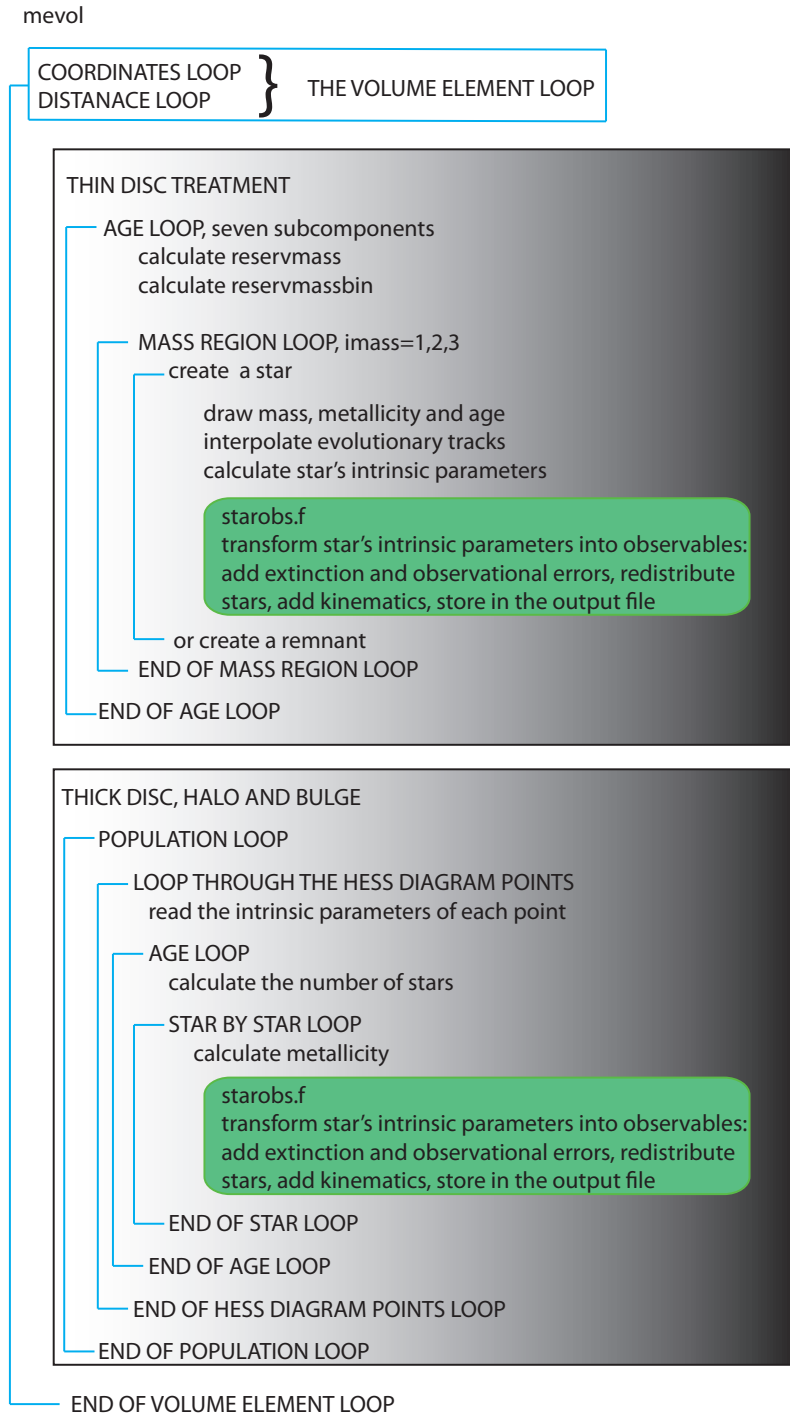


Figure 2.7: The general scheme of the new BGM. The concept of reservmass and reservmassbin is explained at the end of this section and also in the section 2.3. Generally, both variables refer to the pool of mass calculated, at the given volume element and for a given disc subpopulation.

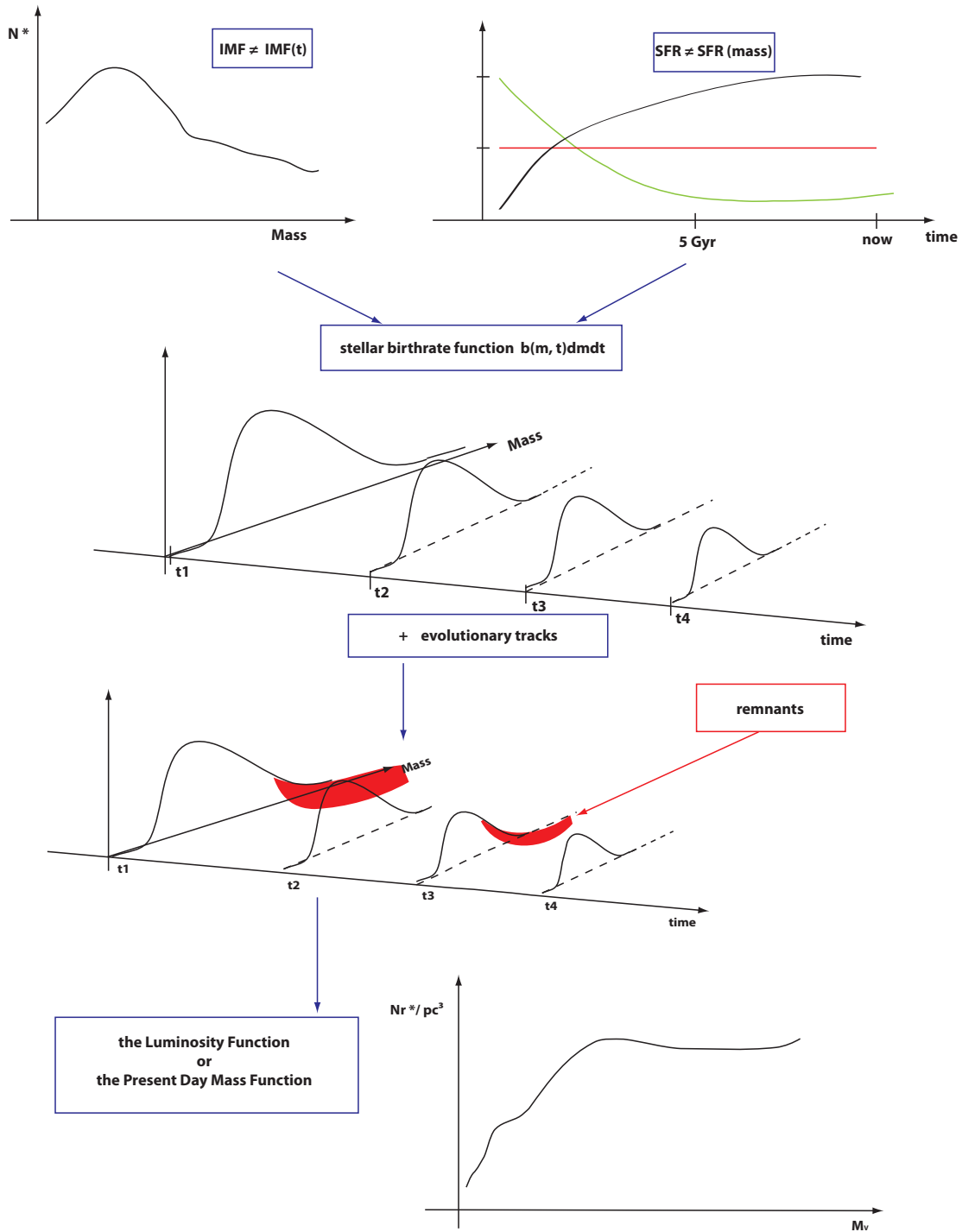


Figure 2.8: The graphical representation of the relationships between the theoretical IMF, SFR, evolutionary tracks and the observed LF or the PDMF.

$$d^2N = \phi(m)\Psi(t)dmdt. \quad (2.4)$$

Thus one can imagine the total number of stars ever produced in the disc as the product of the IMF and SFR continuous activity over the age of the Galactic disc (see the two dimensional graph in Fig. 2.8). During that process of creation stars evolve on their evolutionary tracks and populate the HR diagram. Their lifetimes depend on their initial masses and initial chemical compositions. Many of the stars created throughout the evolution of the Galactic disc have already died, or have moved to the later evolutionary stages. At the same time, among the alive stars we can observe many of the old objects, including some as old as the Galactic disc itself. This is due to the wide range of lifetimes, which the stars span. Applying the knowledge on the stellar evolution to the Eq. 2.4 one can get to know the distributions of stars, which have been already sent to the remnants pool, dead by now (objects marked in red in Fig. 2.8) and the stars expected to be still observed at present (the LF or PDMF).

The Fig. 2.9 presents a simple scheme of the new model's ingredients and the information they provide. The IMF, SFR, age-metallicity relation, evolutionary tracks sets, atmosphere models and space density distributions are specified previous to simulations. Firstly we draw the mass, the age and the metallicity of an object according to the chosen functions and for the obtained values we search for the solution interpolating the evolutionary tracks. If such a solution is found a star with the given L/L_{\odot} , $\log g$ and T_{eff} is created. Using the atmosphere models we convert its intrinsic parameters into the observed ones including the extinction effect and optionally the observational error estimations. From the a priori knowledge on the space density distributions we know how many objects are to be created at various distances within the Galactic disc. Combining all informations we get the nowadays picture of the thin disc. The stars for which the solution on the tracks was not found, meaning that the combination of their age and mass does not correspond to an alive star, have already evolved off the main sequence and giant branches and moved to the remnants cemetery. In the new BGM the remnants we consider are the white dwarfs. We neglect the density in neutron stars and stellar black holes.

That was the general scheme describing the ingredients needed to build up the evolutionary model. Now, we will explain the basic concepts of the new BGM and how we have implemented them. While in the following section 2.3, we discuss in detail the code organization.

The simulations start with establishing the direction of the sky, where the star counts are going to be predicted. The most outer loops of the new code have not changed and similarly like in Robin et al. (2003) they are the coordinates and distance loops. Together they form the volume element loop. As explained in 2.1 the BGM thin disc is divided into seven age subcomponents. That division is maintained in the new model and for that the thin disc treatment is performed separately for each of these subpopulations. Once entered the age loop, the mass available to be spent on stars production in a given volume element has to be calculated. We have named this value the *mass reservoir*. It is an amount of mass that is expected to be found in stars at the specified position (volume element) according to the predefined evolutionary (IMF, SFR) and density (density laws) parameters. It is calculated from the formula

$$\text{mass reservoir} = dV \times \rho(x, y, z, i), \quad (2.5)$$

where i denotes the thin disc age subcomponent. Eq. 2.5 is the spine of the thin disc arrangement. It expresses how the density is treated in the new code and carries the information about various processes and parameters that were taken into consideration throughout our

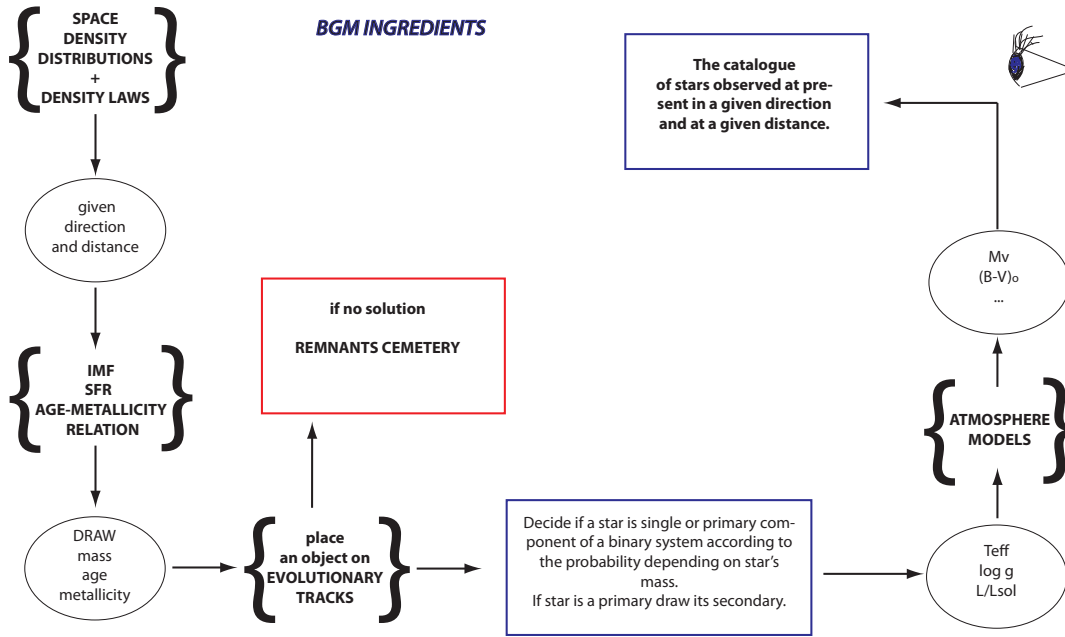


Figure 2.9: The general scheme describing the ingredients needed to build the evolutionary model and the information they provide.

reasoning. Its importance arises from the fact that it is where the star formation history, the density distributions in our Galaxy and finally the Galactic potential meet altogether. Our approach to density calculation is fully explained in the following subsection.

2.2.2 Determination of the mass model

As explained in Robin and Crézé (1986) defining the density $\rho(r, l, b, i)$ for each age subcomponent i requires:

1. an estimation of the density of each component at the Sun position
2. a mathematical law capable of reproducing the trend of the density from the solar neighborhood to remote distances
3. evaluations of the scale heights and scale lengths of each subcomponent in order to constrain free parameters of the mathematical expression.

The thin disc in the BGM is modelled by Einasto density laws. That mathematical model describes how the density of ellipsoidal systems changes with the distance from the Galactic center. It was chosen to represent the thin disc, because it assures the continuity and derivability in the plane. The form and associated parameters of the density laws are presented in Table 3 of Robin et al. (2003), which we discussed in section 2.1 (see Fig. 2.3).

The parameter corresponding to the Einasto representation is

$$a^2 = R^2 + \frac{z^2}{\epsilon^2}, \quad (2.6)$$

where R is the galactocentric distance, z is the height above the Galactic plane, and ϵ is the axis ratio (eccentricity of the ellipsoid). It is also common to use the ellipticity parameter e when describing the density ellipsoids. The relation between ellipticity and eccentricity of an ellipsoid is the following

$$\epsilon = \sqrt{1 - e^2}. \quad (2.7)$$

In the BGM the ϵ variables for all thin disc subcomponents are obtained from dynamics considerations as it is explained later on in this section. Applying the Einasto law we calculate the relative density at the (x, y, z) position. Depending on the age subcomponent and the user's specifications it may include the warp, flare and spiral arms influence. In order to get the absolute density one must normalize the density at the (x, y, z) position to the value at the Sun's position.

When testing new evolutionary scenarios for the Galactic thin disc the idea is to change the model's ingredients several times. Each time we change any of the inputs we get a slightly new definition of the model leading to different results. Then, by comparing those differences we may learn what is the impact of each model's ingredient and what are the interactions between all of them. It is important to know that each time the definition of the model changes the mass model has to be derived. Generally, the process of mass determination in our model consists of three main parts, see the scheme presented in Fig. 2.10. Block A it is a local mass normalization which provides the values of local volume density (at the Sun position) $\rho_{\odot}(i)$ for each age subcomponent i . Part B is where we perform the simulations of the local neighborhood and derive the percentage of alive and dead stars for each thin disc subcomponent. While in the third part C we consider the dynamics to get the parameters of the vertical density distribution. The whole procedure is a normalization iterative process, which using the observational and dynamical constraints provides the values of $\rho_{\odot}(i)$ and $\epsilon(i)$ and for that constructs the mass model to be applied in simulations.

As we explained at first model's ingredients are specified. We start with the local mass normalization. A more detailed scheme for that part is presented in Fig. 2.12. The values of eccentricities $\epsilon(i)$ for each age bin i are the input for this part and they come from the potential calculations. At the beginning some guess values are assigned to them. The other inputs are the SFR, the local surface density Σ_{\odot}^{all} , which initially is being assigned a guess value and local volume density ρ_{\odot}^{all} , which consists of the observed volume density ρ_{\odot}^{obs} and a fraction representing volume density of stars which already went to remnants. For ρ_{\odot}^{obs} we adopt from observations the value of $0.039M_{\odot}/pc^3$ (white dwarfs excluded) and how we get ρ_{\odot}^{dead} we explain in the part B. Due to the subdivision of the thin disc into seven age subcomponents the SFR is introduced to our model by the means of the intensity of star formation rate at each epoch SFR(i). Those seven dimensionless values correspond to the proportion of stars in each disc subcomponent. The way they are calculated is discussed in the section 3.2.

The secular evolution makes the stars evolve on secular orbits. The velocity dispersion increases with time after the star birth because of secular evolution (disc heating). Hence, the older stars have larger scale heights and larger velocity dispersion. When performing any evaluations of the density of stellar content in the SN one must account for it. As the antecedents, in our deliberation we focus on the thin disc population only and consider a cylindrical volume

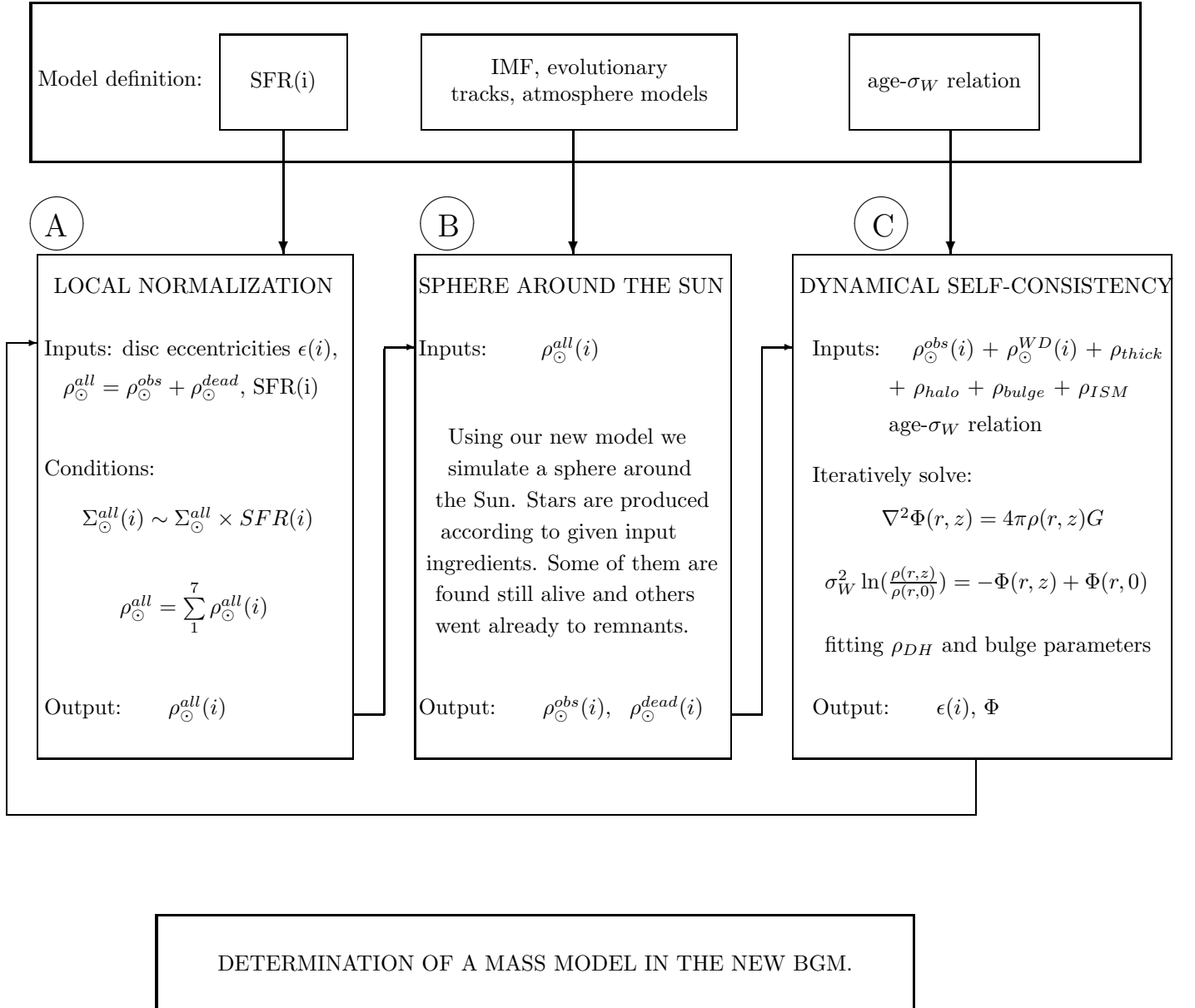


Figure 2.10: The normalization iterative process to derive the mass model in the new BGM.

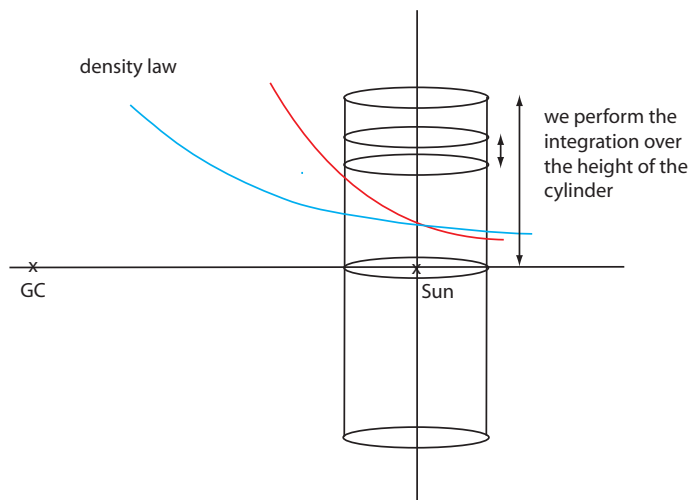


Figure 2.11: In order to perform a normalization of the local volume density we consider a thin disc population enclosed within the cylindrical volume perpendicular to the Galactic plane and with its axis passing through the Sun.

perpendicular to the Galactic plane and with its axis passing through the Sun, see Fig. 2.11. The normalization of the local density refers to the normalization of the volume and surface densities of each age subcomponent in the solar neighborhood. We know from observations the value of the local volume density in stars ρ_{\odot}^{obs} (at all ages), thus the procedure described here is nothing but splitting that value into seven disc subpopulations according to the SFR and including the secular heating process, thus to get $\rho_{\odot}^{obs}(i)$. Due to the construction of our model we need to consider a density of remnants at this point as well. From the density that is provided the model will create alive and dead stars according to the imposed evolutionary tracks and other parameters. That is why we introduce the ρ_{\odot}^{all} , whose value is enlarged such that after simulations of the local neighborhood (part B), in the catalogue of thin disc alive stars we will get the value $0.039M_{\odot}/pc^3$.

Assuming the $\epsilon(i)$ for each population and using the Einasto law we integrate the density $\rho(r, l, b, i)$ in the vertical direction and compute what we call the ratio of surface to volume density $RSVd(i)$. The variables $RSVd(i)$ are conceptually equal to scale heights. It would be correct to call them the scale heights only if we would use exponential laws for density. However, we chose the Einasto description in our model and instead of the scale heights its characteristic parameters are the eccentricities of the density ellipsoids.

Then an iterative process starts. We calculate the surface and volume stellar mass densities for all thin disc subcomponents, $\Sigma_{\odot}^{calc}(i)$ and $\rho_{\odot}^{calc}(i)$ respectively and sum them to get Σ_{\odot}^{calc} and ρ_{\odot}^{calc} . The condition one requires the surface density of each age subcomponent to be proportional to the intensity of SFR in its corresponding age bin. The calculated total volume density ρ_{\odot}^{calc} is compared to the imposed value ρ_{\odot}^{all} checking the fit to observations. If they are different the local surface density will be modified slightly and all calculations will be repeated. When the iteration finishes we get the local volume density split into seven components $\rho_{\odot}^{all}(i)$.

Table 2.1 presents the inputs and outputs of the normalization process in question.

Density normalization	
INPUTS	
$\rho_{\odot}^{obs} = 0.039 M_{\odot}/pc^3$	the total (all ages) volume mass density observed in the SN (white dwarfs not included)
$\rho_{\odot}^{all} = \rho_{\odot}^{obs} + \rho_{\odot}^{dead}$	the total volume mass density in the SN including alive stars and remnants
Σ_{\odot}^{all}	the total (all ages) surface density in the SN; initially a guess and then its value is obtained through the fitting
SFR scenario and corresponding SFR(i) vector	7 dimensionless factors normalized to unity, reflecting the intensity of the SFR acting during each age interval
$\epsilon(i)$	eccentricity of each density ellipsoid resulting from the dynamical-self consistency calculations
OUTPUTS	
$\rho_{\odot}^{all}(i)$	the local volume mass density for each age bin; the normalization factor needed to calculate the <i>mass reservoir</i> (see Eq. 2.5)

Table 2.1: The inputs and outputs of the density normalization process.

Once the values of $\rho_{\odot}^{all}(i)$ are known the second part of the procedure takes place, see block B in the scheme 2.10. We perform the simulations of a sphere around the Sun in order to get the values of local volume density of alive stars split into seven components $\rho_{\odot}^{obs}(i)$. Our model given some specific IMF, SFR, evolutionary tracks, age-metallicity relation, atmosphere models and other ingredients produces stars. Some of those stars are found to be still alive and they will be saved in the output catalogue. Others for whom the age and mass combination was not found on the evolutionary tracks are considered to be remnants. That is why in the local normalization part we are working with the total density value ρ_{\odot}^{all} , which is fitted in such a way that in the output of a sphere simulations we want to find $\rho_{\odot}^{obs}(i) = 0.039M_{\odot}/pc^3$.

The output of part B serves as an input to the C part where we perform the dynamical considerations. There dynamical constraints are used to calculate the disc eccentricities $\epsilon(i)$ and to assure of the dynamical self-consistency. The full description of this process is given in Bienayme et al. (1987), where the authors have studied the mass density in Milky Way and from that produced a consistent dynamical model up to the first moment. Since we have used the

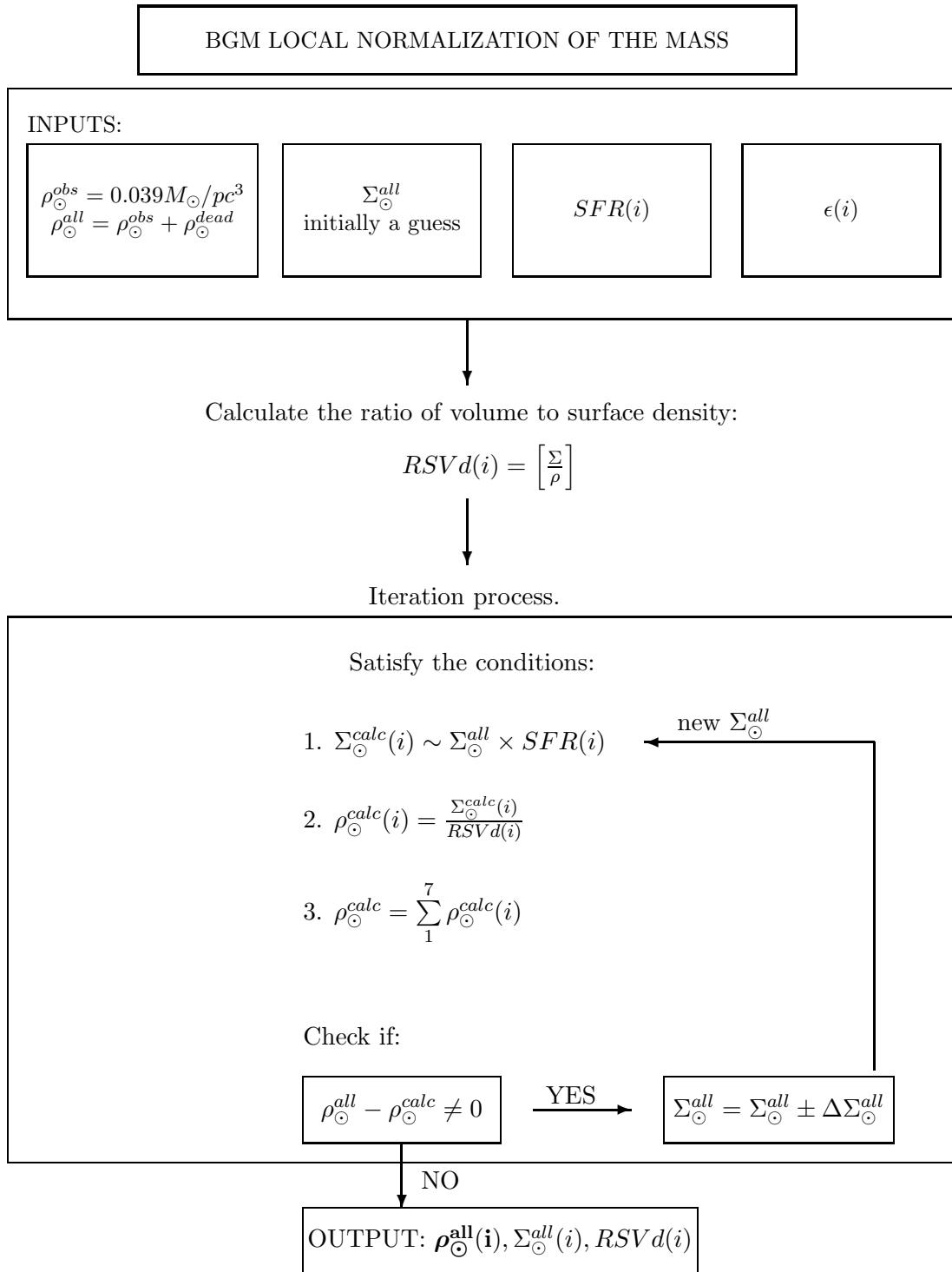


Figure 2.12: The process of local mass normalization in the BGM.

same approach we give here a brief overview of those calculations.

At the beginning we do not assume any a priori potential and we assign some estimated values to the eccentricities $\epsilon(i)$. The stellar content of the thin disc is simulated using the BGM (block B of Fig. 2.10) and supplemented by the thick disc, stellar halo, bulge and remaining mass components:

- interstellar matter
- dark halo
- and optionally additional local dark matter (it can be set to zero or for example it can reflect the unseen brown dwarfs).

As described in Bienayme et al. (1987) the bulge is modeled by a central point and its mass M_B is the parameter, which will be fitted. The parameters of the dark halo, which will be adjusted are its radius r_c and the central density ρ_c . Initially some guess values are assigned to those dark halo and central mass parameters. All mentioned mass components enter the Poisson's equation and impose the potential:

$$\nabla^2\Phi(r, z) = 4\pi\rho(r, z)G, \quad (2.8)$$

where r refers to Galactic radius and z is the height above the Galactic plane, while $\Phi(r, z)$ is the potential and $\rho(r, z)$ is the density distribution of all included mass components. From that we get a first guess of the potential and the radial force $K_r(r, z)$ and we move to the part where that potential is constrained by the observed Galactic rotation curve. The circular velocity of the model is calculated from the formula:

$$V_{cir}(r) = (-K_r(r, z = 0)r)^{1/2}. \quad (2.9)$$

The central mass and corona parameters are adjusted until the potential reproduces the observed rotation curve. That results in the new potential, which satisfies the first dynamical constraint. Subsequently, it is inserted into the first order moment of the Boltzmann collisionless equation for an isothermal and relaxed stellar population (Mihalas and Routly (1968)):

$$\sigma_W^2 \ln\left(\frac{\rho(r, z)}{\rho(r, 0)}\right) = -\Phi(r, z) + \Phi(r, 0), \quad (2.10)$$

where $\rho(r, z)$ is the mass density of that population and σ_W its mean W velocity dispersion. The approximation of isothermality and relaxation is fulfilled within each sub-component of the disc of age larger than 0.15 Gyr. The values of the σ_W velocity dispersion for each subcomponent i are adopted from observations and are the inputs of our model, see section 3.7.

The disc eccentricities $\epsilon(i)$ are adjusted until the Eq. 2.10 is accurately satisfied. Modifying the eccentricities we are changing the mass distribution on the left side of the equation, until it fits the potential on the right side. In the presented strategy, the Eq. 2.8 and 2.9 are being solved separately from the Eq. 2.10, what does not lead to a potential satisfying both constraints. In order to achieve that the process must be iterated. Therefore, having the new eccentricities, we again calculate the potential and fit the central mass and corona parameters using the constraints from the Galaxy rotation. Then the Boltzmann equation is solved and again new values for $\epsilon(i)$

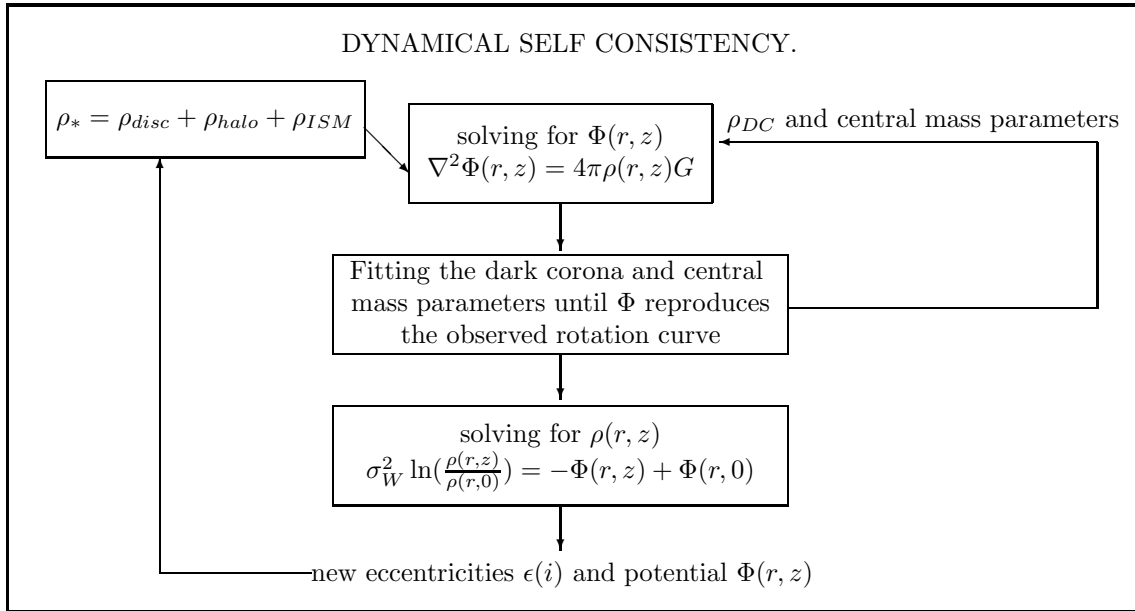


Figure 2.13: Dynamical considerations in the BGM.

are adjusted. The process is repeated until the changes in the potential and other parameters are less than 1 %. In that way following the Bienayme et al. (1987) procedure we produce a self-consistent model. That process has to be repeated each time the evolutionary parameters the SFR, IMF and age- σ_W relations change.

2.3 The code and its implementation

2.3.1 The thin disc treatment

The BGM gives the star counts predictions towards the indicated direction in the sky. Either a line of sight or a zone can be chosen. The most outer loop is the volume element loop, thus stars are produced with distance steps while moving from the Sun till the chosen limiting value. At each volume element the objects belonging to the four basic Galactic components are generated subsequently. As explained in previous sections, we have rebuilt the thin disc treatment and here we present and discuss its new structure. We start with the general outline of the new model's thin disc treatment, which is sketched in the Fig. 2.14.

The most outer loop of the thin disc treatment is the age loop. Each disc's subcomponent, that is from the first to the seventh age bin is simulated separately. At small distances from the Sun the volume elements we construct are small too. In those cases the mass available to spend on stars is small as well and they lead to a tendency of creating more abundantly less massive objects than the more massive ones. Whenever the mass was not sufficient to produce a more massive star too many low mass ones were drawn and in turn it would bias the shape of the IMF. We have investigated that the bias introduced this way is significant and for that we developed two prevention mechanisms. The first one is a simple correction for the small volume elements. We enlarge the volume element by a given factor (estimated through fitting) and draw the masses from that enlarged pool. It assures that the mass calculated for that enlarged volume element is big enough for different masses to be drawn with no bias. However, not all drawn masses are kept as we have enlarged the volume element. For the further calculations we keep only a factor of drawn objects, which correspond to the original small volume element. This treatment protects from the underestimation of the stars from the high-mass IMF tail. As already mentioned, in the new model we introduce the idea of mass reservoir. The pool of mass available at the specified position within the Galactic disc is calculated from the formula 2.5 splitting it into seven subcomponents. As explained in the previous section $\rho_i(x, y, z)$ is obtained taking into account the density law, SFR and secular heating corresponding to a given i -th subcomponent and local mass normalizations. Then, the mass reservoir expressed in M_\odot and calculated for a given volume element and disc subcomponent is divided into three bins corresponding to three IMF ranges, see section 2.3.1. By construction our model works with three mass ranges and it permits introduction of at most three-slope IMF. In practice it means that the IMF can have one, two or three slopes and previously to simulations it will be divided into three ranges. Consider Fig. 2.15. This division is our second prevention mechanism against underestimating the high-mass stars and biasing the IMF. The drawing of the stars is done separately for each mass region starting always from the high mass area, then moving to intermediate masses and finishing at the low masses (see the mass range loop in Fig. 2.14). In order to divide the mass reservoir into three parts corresponding to three IMF regions we have derived formulas for the mass normalization factors. They are presented in 2.3.1.

Once we are inside the mass range loop the stars production proceeds until there is no more mass to translate into stars (mass reservoir=0). Firstly, the mass of an object is drawn from the given IMF. Details of this procedure are presented in the 2.3.1. Then, it is checked if the reservoir of mass is sufficient to create a drawn object. The high mass region corresponds to the long and steep tail of IMF, so in that case it is likely that a mass drawn for a star candidate will exceed the total mass available, although resources are relatively big. A similar situation applies

THIN DISC TREATMENT

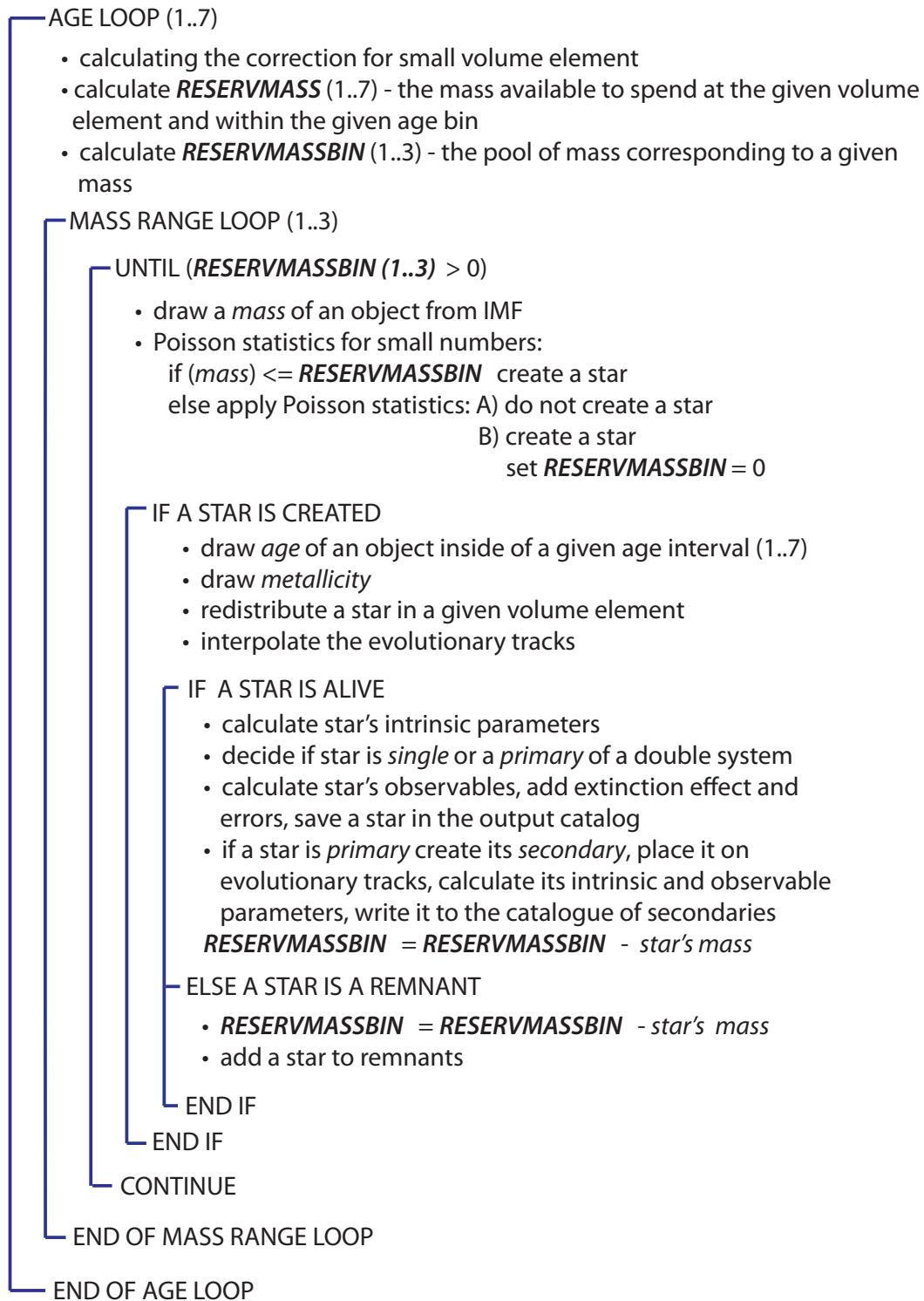


Figure 2.14: The organigram of the new model's thin disc treatment.

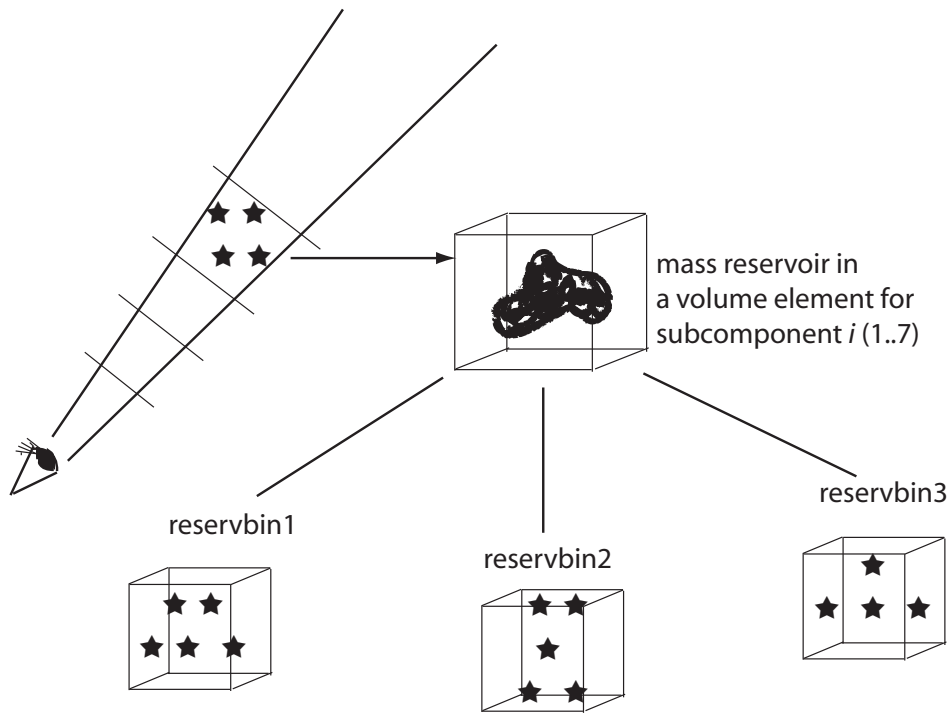


Figure 2.15: The mass reservoir calculated in the given volume element and for a given disc subcomponent is divided into three bins corresponding to three IMF ranges, which will be high mass area, intermediate and low masses. By construction, our model permits introduction of up to three-slope IMF.

to the remaining two mass regions, but with smaller rate of occurrence. Losing that mass would after all produce a bias in the mass distribution. To correct for that we have introduced the Poisson statistics for small numbers. Our approach consists of three possible actions. If there is enough mass in the pool for the star to be created, it will be created in an ordinary way. If the mass of drawn object exceeds the reservoir mass the Poisson statistics will be applied and as a consequence a star may be created in an extraordinary way or it might be rejected. The procedure is depicted in the tree graph in Fig. 2.16. The standard way of creating a star implies that the mass of the object will be subtracted from the total mass available to spend, while in the extraordinary case after creating the object the total mass will be set to zero. If the path of not creating a star at all is followed the mass which was left in the pool is lost and the mass reservoir is set to zero.

If an object was created we assign to it an age and metallicity. The ages are drawn randomly from the uniform distribution between the ranges of the given age subcomponent. Once the age is known the metallicity is calculated according to the specified age-metallicity relation. Then, the object is redistributed in the given volume element. When the age, mass and metallicity are established we interpolate the evolutionary tracks and find the position of the star on the HR diagram. If such a solution was found we consider that a star is alive and we will move on with the calculations of the observed parameters for that star, while if the solution was not found the star is added to the remnants counter. If the star is alive its intrinsic parameters are calculated and then according to a given probability it is decided if that star is single or it is

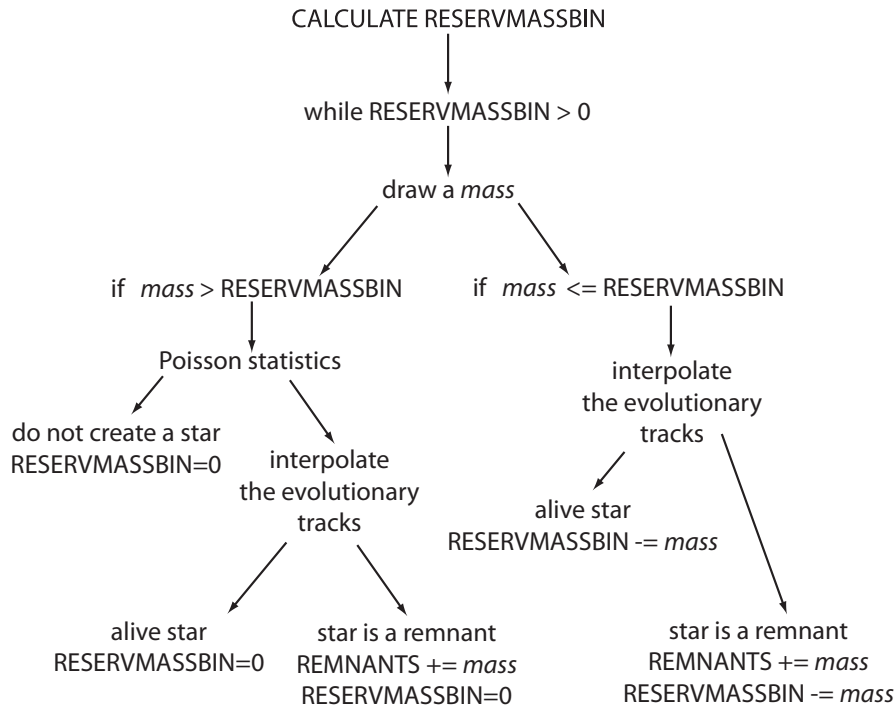


Figure 2.16: The Poisson statistics for treating small values of mass reservoir. A star can be created in a standard way or an extraordinary way when the available resources were not enough or it can be rejected.

a primary component of a binary system. Subsequently, the observables are assigned to that object, optionally the extinction and errors are added and the star is written to the catalogue. If the produced star was flagged as a primary (see section 2.3.2) we create its secondary, place it on the evolutionary tracks, calculate its intrinsic parameters and write it to the catalogue of secondaries. The merging of binary systems is performed outside the simulations in the post processing. More details about the binarity implementation in the section 2.3.2.

We proceed producing stars subsequently from the three mass ranges as long as there is mass left in the given pool. The procedure continues for all age subcomponents and for all volume elements.

We have chosen the standard power law as the IMF representation

$$\phi(m) = m^{-(1+x)}, \quad (2.11)$$

where m is the mass and x is the slope. It is also common to denote $(1+x)$ as α parameter, so then we have

$$\phi(m) = m^{-\alpha}. \quad (2.12)$$

Our code is designed to deal with three slope initial mass function as it is visualized in Fig. 2.17. It is very important to note that the Eq. 2.11 returns the number of objects in a given mass interval, thus to get that number one must integrate it on that interval

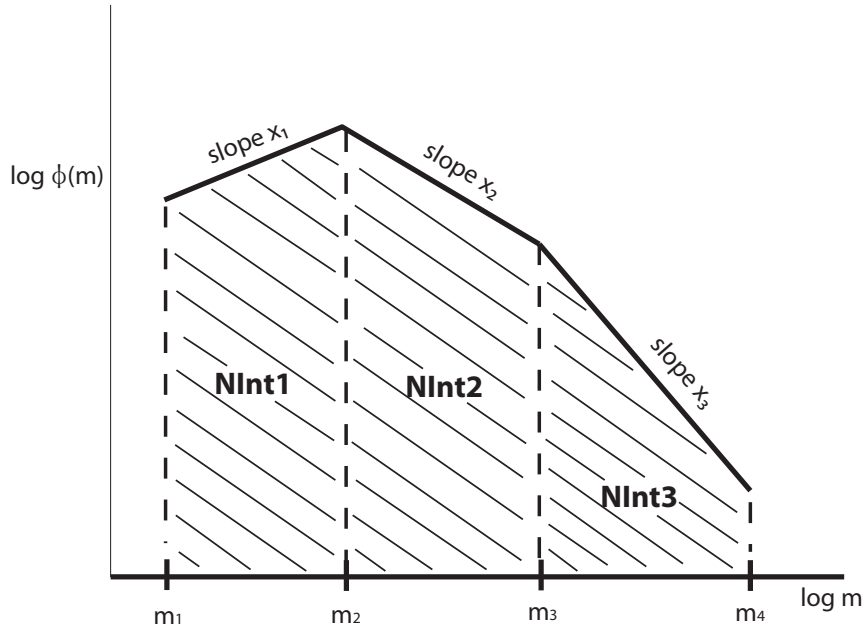
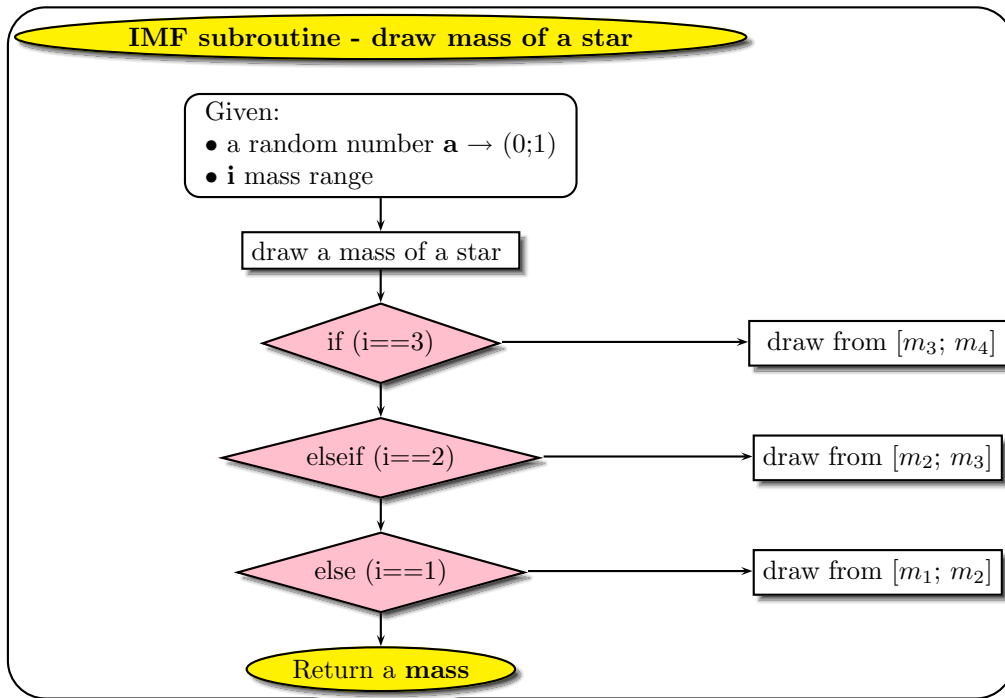


Figure 2.17: Schematic representation of IMF. By construction our model works with three mass ranges and it permits introduction of at most three-slope IMF.

$$NInt_i = \int_{m_i}^{m_{i+1}} \phi(m) dm = \int_{m_i}^{m_{i+1}} m^{-(1+x)} dm = \frac{1}{-x_i} (m_{i+1}^{-x_i} - m_i^{-x_i}). \quad (2.13)$$

$NInt_1$, $NInt_2$ and $NInt_3$ depicted in Fig. 2.17 are the integrals corresponding to the three areas bounded by the IMF and their values express the number of objects in each mass range. Those values are used to draw the mass of each particular star.

In the flowchart below we present a simple scheme of drawing the mass of an object from the IMF, which is applied in our model.



Subsequently, we show how we have derived the expression to draw the mass of an object in each mass range. Our IMF from the Eq. 2.11 is a 1-dimensional distribution function. We impose that

$$\int_0^{\infty} \phi(m) dm = 1. \quad (2.14)$$

Then, we define the normalized, cumulative distribution function

$$F(m) = \int_{-\infty}^m \phi(m) dm = \int_{-\infty}^m m^{-(1+x)} dm, \quad (2.15)$$

and after integrating we get

$$F(m) = \frac{m^{-x}}{-x} = \frac{m\phi(m)}{-x}. \quad (2.16)$$

We create a random realization of a uniform probability distribution in F and we use it to draw a mass of an object

$$\frac{m^{-x}}{-x} = \frac{m_1^{-x}}{-x} + a \left(\frac{m_2^{-x}}{-x} - \frac{m_1^{-x}}{-x} \right), \quad (2.17)$$

where a is a random value from a range $(0; 1)$. Then, by multiplying both sides by $(-x)$ we have

$$m^{-x} = m_1^{-x} + a (m_2^{-x} - m_1^{-x}), \quad (2.18)$$

so to draw the mass m we use the expression:

$$m = [m_i^{-x_i} + a (m_{i+1}^{-x_i} - m_i^{-x_i})]^{-1/x_i} \quad (2.19)$$

for $i = 1, 2, 3$, each of the mass intervals.

Using Eq. 2.13 we have

$$m = [m_i^{-x_i} - a x_i NInt_i]^{-1/x_i}. \quad (2.20)$$

On the other hand, to get the mass locked within each mass interval one must solve

$$\int m \phi(m) dm = \int m m^{-(1+x)} dm \quad (2.21)$$

for all three ranges. The sum of those three numbers must be normalized to one such that

$$\int_{m_1}^{m_4} m \phi(m) dm = 1 \quad (2.22)$$

where m_1 and m_4 are the minimum and maximum masses between which the IMF is defined.

In order to fulfill the continuity condition it must occur that:

$$m \phi(m_2) = K_1 m_2^{-(1+x_1)} = K_2 m_2^{-(1+x_2)} \quad (2.23)$$

and

$$m \phi(m_3) = K_2 m_3^{-(1+x_2)} = K_3 m_3^{-(1+x_3)}. \quad (2.24)$$

K_1 , K_2 and K_3 are the continuity coefficients and they have such values that

$$K_1 \int m \phi(m_1) dm + K_2 \int m \phi(m_2) dm + K_3 \int m \phi(m_3) dm = 1. \quad (2.25)$$

Thus the relative mass locked within each mass interval is computed as:

$$K_i \int_{m_i}^{m_{i+1}} m \phi(m) dm = MInt_i. \quad (2.26)$$

As explained in the previous subsection, the *mass reservoir* needs to be divided into three parts. This imposes a requirement that the normalization must be done on the mass and it is achieved by applying the Eq. 2.26. The sum of those values is normalized to one, so when we multiply the *mass reservoir* (total mass in a given volume element) by each of them we distribute the available mass over three ranges in a given volume element for a given subpopulation.

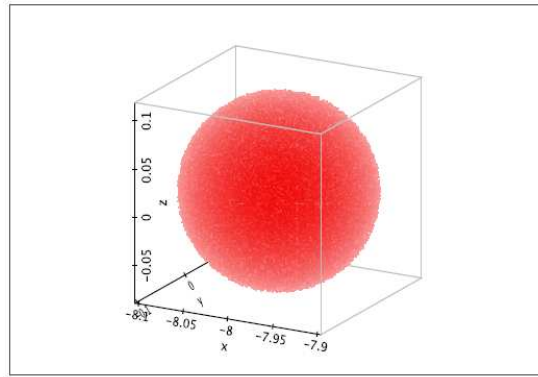
The integrals, continuity coefficients and normalization factors are calculated in a separate piece of code previously to simulations and serve as input values for the model. Whenever we decide to change the characteristics of the IMF we have to recalculate those parameters.

2.3.2 Binariness

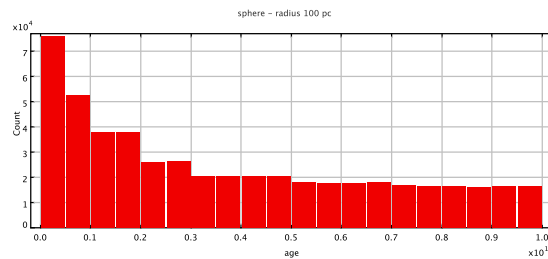
The new Besançon Galaxy Model is not any more a generator of single stars only, but it produces binary systems as well. We have implemented the binarity in the code following the scheme proposed by Arenou (2010), which is applied in the Gaia simulator. The procedure is quite straightforward, see the core of the thin disc treatment in Fig. 2.14. The age, mass and metallicity of an object are drawn and then it is placed on the evolutionary tracks. If the star is found to be alive, we calculate its intrinsic parameters and decide if it is single or a primary component of a double system. This decision is made according to the probability, which depends on the object's mass and luminosity class, see section 3.4. At this stage a star is marked by a flag if it is single or a primary component of a double system. If the star, which has just been created was a primary, we subsequently create its secondary and this is achieved in few steps. First, the separation of the system is estimated. Next using a first guess secondary mass and system's separation the period is calculated from the Kepler's third law. Then, knowing the period and the M_1 mass of the primary we derive the M_2 mass of the secondary. We perform a check if there is enough mass in the corresponding *mass reservoir* to create the secondary star. If the mass left in pool is not sufficient to create a secondary object, the primary is converted into single star and if the secondary is created successfully we assign it the same age and the same metallicity as of primary object. Then the observables of the primary are calculated and it is written to the catalogue. Similarly like for the primary component, the secondary is placed on the evolutionary tracks and its intrinsic parameters are determined. We are not considering interactive binaries which have perturbations on their evolutionary tracks due to the presence of the primary. In our algorithm the secondary star will always be found alive since at that point it was already checked that its primary which is more massive is alive. Then we derive the observables of the secondary star and save it in a separate catalogue. In our scheme merging of systems is done outside the model in the post processing. That is why if the binarity option is switched on by the user two catalogues will be created, one with single and primary stars and other with secondary components. As well the extinction effect and photometric errors will not be added directly in the simulations but saved in the catalogues. They will be applied in an independent merging code. As explained above during simulations each binary system is assigned a separation. In order to decide whether it will be resolved or not, we first randomly incline it with respect to the line of sight and then project the system on the sky. Subsequently the angular separation is computed and the decision if the system is going to be merged or separated depends on the imposed resolution of the catalogue.

In the future the merging part can be incorporated into the model, however at the moment such an arrangement has a quite convenient advantage, namely it allows us to apply several catalogue spatial resolutions to one simulated sample.

It must be emphasized that we have implemented binarity remaining in agreement with the total mass in stars. It is a big advantage of the new BGM's scheme that the total mass is constrained previously to simulations, throughout the dynamical self-consistency calculations. That means that the mass is established before and the stars, single or double, are created from the available *mass reservoir*. Each time a star or a remnant is created we subtract its mass from the total pool. This is the part which the Gaia simulator presently lacks.



a) A sphere of 100 pc radius around the Sun.



b) The age distribution of a 100 pc radius sphere.

Figure 2.18: Simulations with a sphere mode. Option added to the model for fitting the simulations to the local luminosity function.

2.4 New processing modes

The BGM has several different modes in which simulations can be performed and stars created. One can choose between histograms of star counts, stars along a line of sight or in the zone of the sky, integrated light or densities on the line of sight. Since in our project we are working with stars production concepts we have encountered a strong need of performing a volume limited simulations in the SN. Especially there are two cases when we were interested in limiting our samples by its volume, when reproducing the local observed luminosity function and reconstructing the imposed SFR.

In the task of fitting the local luminosity function one usually considers a sphere at the Sun, while for studying the SFR a cylindrical volume centered at Sun is the best. Inspired by that we have incorporated two new processing modes inside the model, such that we can simulate a sphere or a cylinder centered at the Sun position.

In the case of a sphere the same density is assumed for all the volume. This approximation is valid when performing a task of fitting the simulations to the local LF. There is just one volume element imposed by the user, by the means of the radius. Simulations are done in one step, meaning there is no second step in coordinates or distance. Therefore once we arrive to the thin disc treatment, the calculations are done once for each of the thin disc subcomponents. The produced stars are then randomly redistributed around the Sun. In Fig. 2.18 a we see

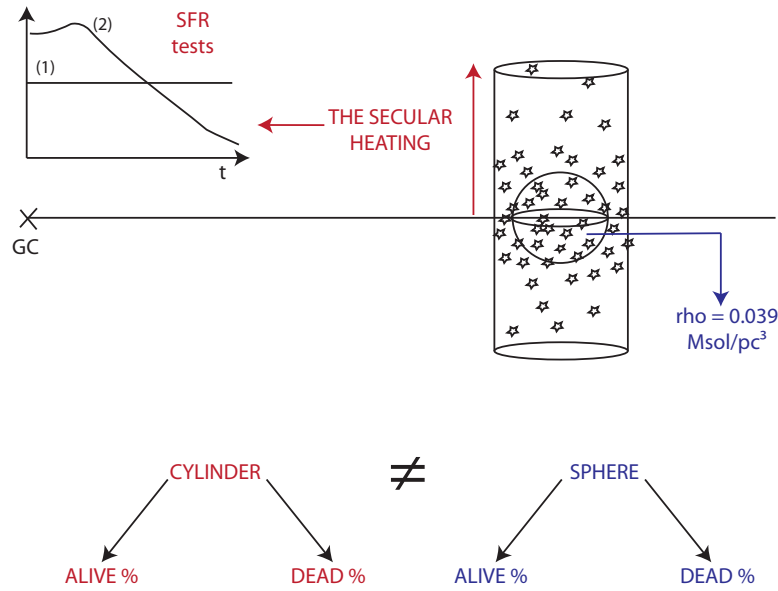


Figure 2.19: A concept of two new processing modes for stars production. A sphere is used to reproduce the local volume density and to test the LF, while a cylinder is used to test if a model is able to reproduce an imposed SFR.

an example of sphere of a radius 100 pc simulated around the Sun and in Fig. 2.18 b the age distribution of this sample.

As the sphere mode is a perfect tool for the task of luminosity function reproduction, it is a completely wrong approach when testing the SFR. Even if one would consider all stars ever born within a sphere around the Sun, one would not reproduce the original SFR when looking at their age distribution, because of the disc heating process and its dependence on scale heights. Stars are born within the plane where the gas is and then throughout their life, with each revolution around the Galaxy center their orbits get more elliptical and the corresponding velocity dispersion increases as well as the scale height. This is why the higher from the plane we move the older stars we find or in other words the old stars are supposed to be spread vertically more than the young stars. More massive stars live shorter than low mass objects thus we observe the high-mass stars strongly concentrated towards the Galactic plane, while low-mass stars are found within the plane and several parsecs outside the disc. In order to recover the SFR (which represent the value at birth) we need to deduce the distribution of stars in age after the secular heating has taken place, and at different height from the plane. This is done by correcting the number of stars of each age in the Galactic plane from the SFR, which gives the values as integrated in the solar cylinder (perpendicular to the Galactic plane and with its axis passing through the Sun). Then the number of stars of a given age at different heights will be computed from the new distribution in age at $z=0$ multiplied by the density law (which depends on the age).

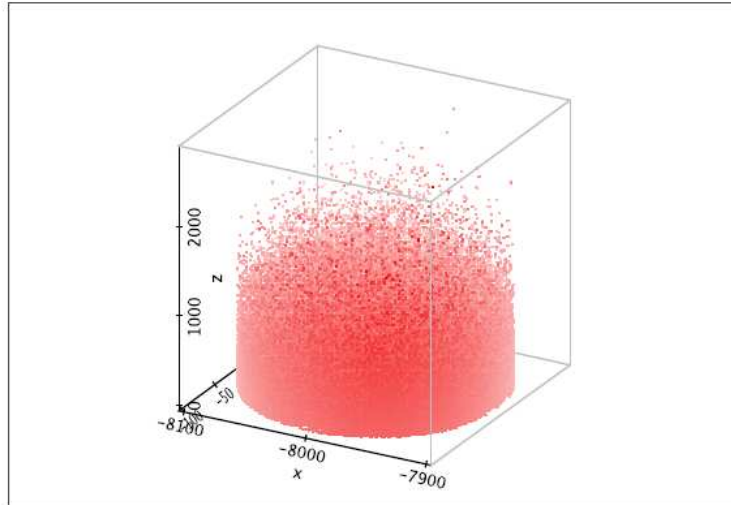
Consider Fig. 2.19 where we illustrated the usefulness of both modes. The concept of a sphere is used to reproduce the local volume density and local LF, while a cylinder is used to

test if a model is able to reproduce an imposed SFR.

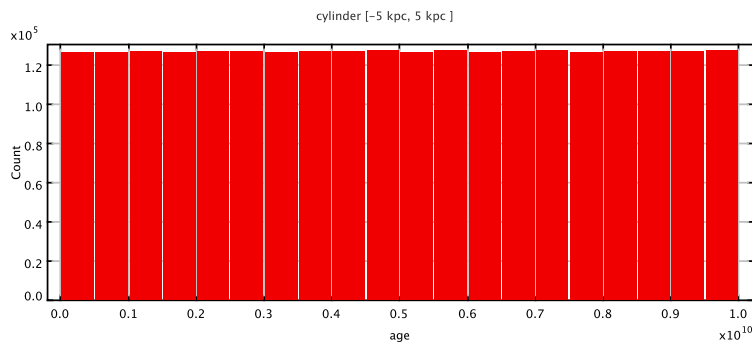
When simulating a cylindrical volume we need to go high enough to cover all seven disc subcomponents. As they differ in ages, the oldest will be found furthest from the plane. In Fig. 2.20 a you can see an example of a simulated cylinder.

Although in simulations we have set the maximum height of a cylinder to 5 kpc, we see a strong drop in density of stars already at 2 kpc. It will depend on the scale heights or eccentricities imposed in the model, but 3 kpc seems to be fair enough for the values of scale heights we have tested in our model.

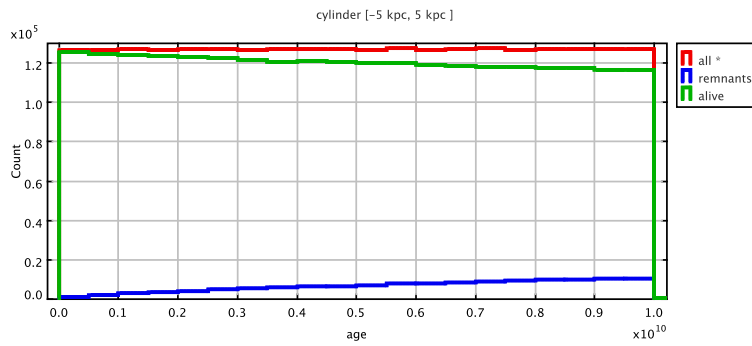
Using a cylinder mode we have tested our algorithms of stars production and checked if we are able to reproduce the imposed theoretical SFR. In Fig. 2.20 b we show the age distribution corresponding to the simulation from Fig. 2.20 a. This is when a constant SFR was imposed and of course all stars ever born are taken into account here, meaning stars which are still alive and those who moved already to remnants. In Fig. 2.20 c we distinguish in colour the age distribution of remnants and alive stars.



a) cylinder [-5 kpc, 5 kpc]



b) the age distribution of cylindrical volume



c) age distribution: remnants (blue) and alive stars (green)

Figure 2.20: A cylinder mode around the Sun. Radius - 100 pc, height - 5kpc. A test of reproducing a constant SFR.

Chapter 3

The update of model's inputs

We remind that our work was dedicated to the thin disc, thus all presented considerations refer to that population only.

3.1 The Initial Mass Function

We have tested several scenarios of the IMF in our simulations. Below we give a list of the ten most interesting IMF that have been applied, five are from the literature and the other five are our propositions. All the considered IMFs have a power-law form presented in the Eq. 2.12 and they differ only in the number and values of slopes and corresponding mass ranges.

1. Haywood et al. (1997a)

$$\alpha = \begin{cases} 1.7 & 0.09 \leq M/M_{\odot} < 1.0 \\ 2.5 & 1.0 \leq M/M_{\odot} < 3.0 \\ 3.0 & 3.0 \leq M/M_{\odot} < 120 \end{cases}$$

2. Haywood et al. (1997b) + correction of one slope in Robin et al. (2003), hereafter called Haywood-Robin

$$\alpha = \begin{cases} 1.6 & 0.09 \leq M/M_{\odot} < 1 \\ 3.0 & 1 \leq M/M_{\odot} \leq 120 \end{cases}$$

3. Vallenari et al. (2006) + our extension of mass range
their original function:

$$\alpha = \begin{cases} 1.1 & 0.2 \leq M/M_{\odot} < 0.8 \\ 2.3 & 0.8 \leq M/M_{\odot} \leq 120 \end{cases}$$

and because they do not specify the slope for masses below $0.2 M_{\odot}$, we simply extended the mass range to $0.09 M_{\odot}$:

$$\alpha = \begin{cases} 1.1 & 0.09 \leq M/M_{\odot} < 0.8 \\ 2.3 & 0.8 \leq M/M_{\odot} \leq 120 \end{cases}$$

4. Kroupa (2008)

$$\alpha = \begin{cases} 1.3 \pm 0.3 & 0.09 \leq M/M_{\odot} < 0.5 \\ 2.3 \pm 0.5 & 0.5 \leq M/M_{\odot} \leq 150 \end{cases}$$

5. Just and Jahreiß (2010)

$$\alpha = \begin{cases} 1.25 & 0.09 \leq M/M_{\odot} < 1 \\ 2.35 & 1 \leq M/M_{\odot} < 2 \\ 3.0 & 2 \leq M/M_{\odot} \leq 100 \end{cases}$$

6. Kroupa-Haywood v1

$$\alpha = \begin{cases} 1.3 & 0.09 \leq M/M_{\odot} < 0.5 \\ 2.3 & 0.5 \leq M/M_{\odot} < 1.53 \\ 3.0 & 1.53 \leq M/M_{\odot} \leq 120 \end{cases}$$

7. Kroupa-Haywood v4

$$\alpha = \begin{cases} 1.3 & 0.09 \leq M/M_{\odot} < 0.5 \\ 2.3 & 0.5 \leq M/M_{\odot} < 1.53 \\ \mathbf{3.5} & 1.53 \leq M/M_{\odot} \leq 120 \end{cases}$$

8. Kroupa-Haywood v6

$$\alpha = \begin{cases} 1.3 & 0.09 \leq M/M_{\odot} < 0.5 \\ \mathbf{1.8} & 0.5 \leq M/M_{\odot} < 1.53 \\ \mathbf{3.2} & 1.53 \leq M/M_{\odot} \leq 120 \end{cases}$$

9. Kroupa-Haywood v7

$$\alpha = \begin{cases} 1.3 & 0.09 \leq M/M_{\odot} < \mathbf{0.8} \\ 2.3 & \mathbf{0.8} \leq M/M_{\odot} < 1.53 \\ 3.0 & 1.53 \leq M/M_{\odot} \leq 120 \end{cases}$$

10. Kroupa-Haywood v8

$$\alpha = \begin{cases} \mathbf{1.1} & 0.09 \leq M/M_{\odot} < 0.5 \\ \mathbf{2.1} & \mathbf{0.8} \leq M/M_{\odot} < 1.53 \\ 3.0 & 1.53 \leq M/M_{\odot} \leq 120 \end{cases}$$

The IMF called Kroupa-Haywood v1 was proposed by us and investigated throughout this research. As its name suggests it was obtained by combining two literature IMFs, the Kroupa (2008) and Haywood-Robin IMF. The motivation for constructing that function were our preliminary results obtained when comparing simulations to data. We decided to keep and merge the parts of both functions where they perform better in those comparisons. Thus we kept the IMF from Haywood et al. (1997b) for the most massive stars and Kroupa (2008) for the rest.

Fitting and arriving to those conclusions is explained at length in the chapter 5. At this point we are just going to describe the construction of that function.

We were interested in the comparison of the IMF functions we have chosen for our research with the log-normal distribution of IMF proposed by Chabrier. In the paper Chabrier (2003) the author specifies that IMF should be well described by power-law form for $M > 1M_{\odot}$ and a log-normal form below that limit.

The analytical expression he specifies for the low masses ($M < 1M_{\odot}$) is expressed in $(\log M_{\odot})^{-1}pc^{-3}$ and has a form:

$$\xi(\log m) = C \times \exp\left(-\frac{(\log m - \log(m_c))^2}{(2 \times \sigma^2)}\right), \quad (3.1)$$

where C is a constant, m_c is a center mass of a distribution and σ a variance in logarithmic mass. The values of those parameters determined from the observed LF were: $C = 0.158$, $m_c = 0.08$ and $\sigma = 0.69$.

In Chabrier (2005) the IMF for $M < 1M_{\odot}$ was revised and due to new data constraints the parameters of Eq. 3.1 were changed to the form

$$\xi(\log m) = 0.093 \times \exp\left(-\frac{(\log m - \log(0.2))^2}{(2 \times 0.55^2)}\right), \quad (3.2)$$

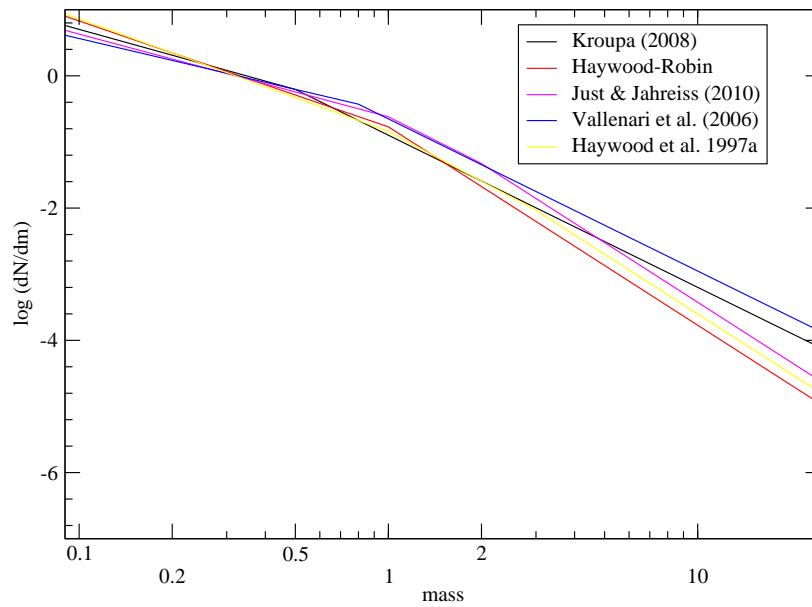
while for the $M > 1M_{\odot}$ he proposes the simple power law $0.041 m^{-1.35}$.

In the range of $0.5 M_{\odot}$ and $1.0 M_{\odot}$ the log-normal IMF of Chabrier (2005) gets very close to the Kroupa (2008) IMF. We have checked and it is shown later on that in that range Kroupa (2008) IMF reproduces the observational data very well. While Haywood-Robin IMF reproduces best the high masses tail. In order to merge the two functions we looked for their intersection above $1 M_{\odot}$. It was found to be at $1.53 M_{\odot}$. Below that value we kept the IMF of Kroupa (2008) and above the one of Haywood-Robin IMF.

Subsequently we have checked what will be the influence on the simulated star counts and colour distributions, when changing the values of slopes or mass ranges for that function. In the list of IMFs presented at the beginning of this subsection we give five different versions of Kroupa-Haywood IMF and in bold we mark the parameter, which was modified with respect to the reference first version of this function. In the chapter 5 we present the influence of those changes on the resulting simulations and discuss how those results perform when compared to observations.

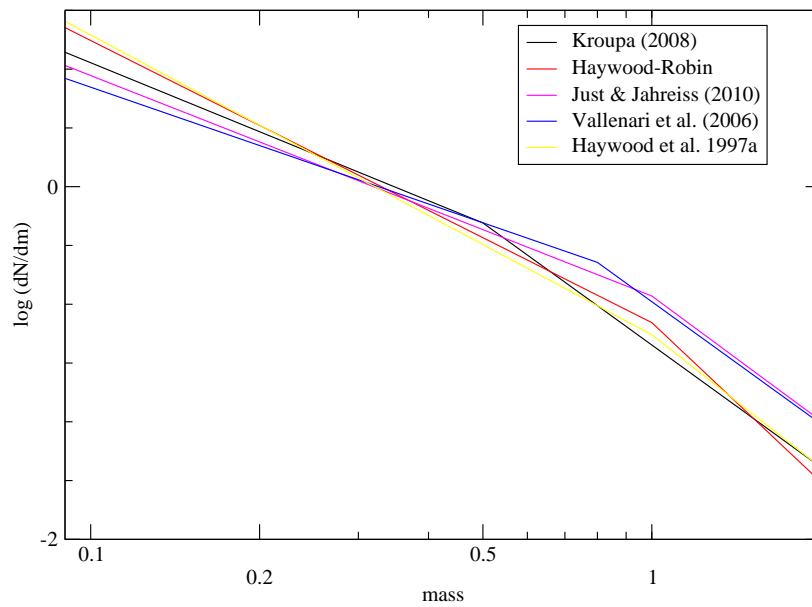
In Fig. 3.1 we present five IMF from literature that we have tested in our research .

Five Initial Mass Functions from literature that we have tested.



a) $0.09 - 25 M_{\odot}$

Five Initial Mass Functions from literature that we have tested.



b) $0.09 - 2.0 M_{\odot}$

Figure 3.1: Five IMF from literature that we have tested in our research.

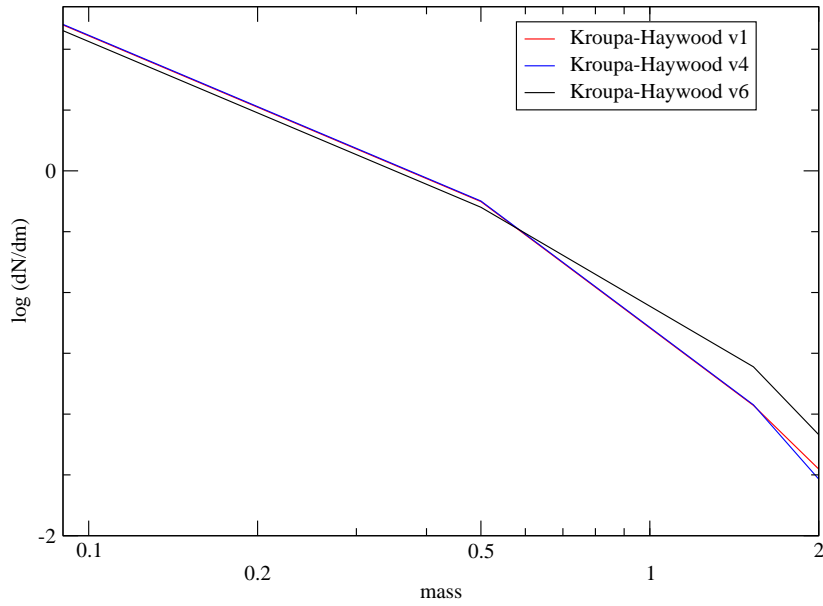
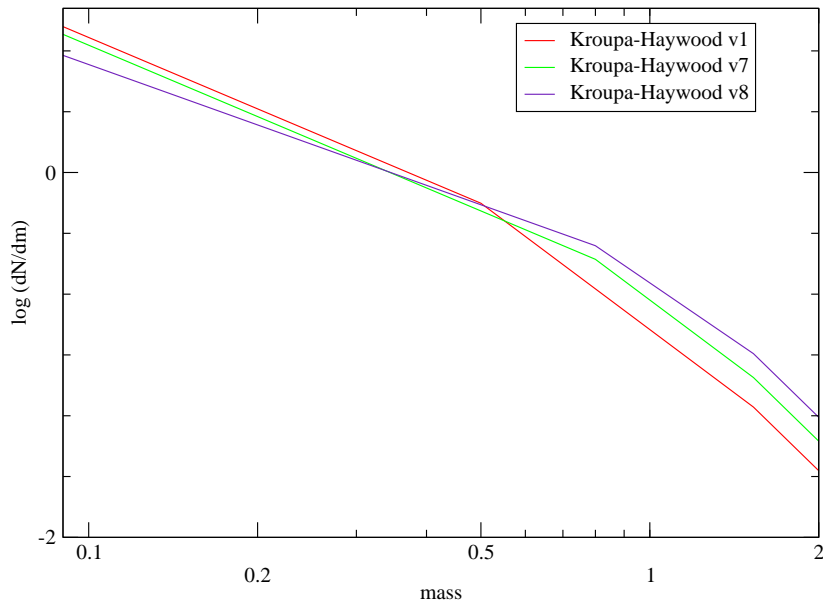
a) $0.09 - 2.0 M_{\odot}$ b) $0.09 - 2.0 M_{\odot}$

Figure 3.2: Five IMF that we have created and tested in our research.

3.2 The Star Formation Rate

In our analysis we have checked both constant and decreasing SFRs. In order to test a declining scenario we followed Aumer and Binney (2009) and as a starting point we chose a simple exponential function

$$SFR(\tau) \propto \exp(\gamma\tau) \quad (3.3)$$

where γ is a parameter and τ is the age. At the beginning we worked with one specific value of γ parameter, namely 0.12. Note that the variable in this equation is age, so the positive value of the parameter γ corresponds to the decreasing SFR. If we would express that equation using the time t variable the minus in the exponent should be added. It is one of the Aumer and Binney (2009) best fits. However, we want to emphasize that the γ parameter is correlated with the values of other parameters used in the model and especially with the slopes of IMF and the age of the disc. This multi-dependency and interplay between different model's ingredients oblige us to always look for the best global fit. In this context one could not give the best solution for a particular variable without correlating it with others. Throughout this research we always kept that in mind. Subsequently we have checked even a more decreasing SFR when $\gamma = 0.25$ and later also a more complex expression, such the input function of the model A from Just and Jahreiß (2010)

$$SFR(\tau) = \langle SFR \rangle \frac{(t + t_0)t_n^3}{(t^2 + t_1^2)^2}, \quad (3.4)$$

where t is time, $\langle SFR \rangle$ is the mean SFR, $t_0 = 5.6$ Gyr, $t_1 = 8.2$ Gyr and $t_n = 9.9$ Gyr. Those three decreasing SFRs, which we have applied in our simulations and tested against the data are depicted in Fig. 3.3 as a function of time, so in the case of exponential expressions a minus was added in the exponent.

After choosing a mathematical expression for the SFR we have to translate it into the representation used in our model. Due to the subdivision of the thin disc into seven age components we work in our new model with seven values of SFR, corresponding to the intensities of SFR in each age interval. In other words those values correspond to the proportion of stars in each disc subcomponent.

In the case of exponential function we obtain those intensities solving the equation

$$SFR(i) = \exp(\gamma \times x_c(i)) \times d, \quad (3.5)$$

where $x_c(i)$ is the age at the center of the i th bin and d is the size of that age bin. A sum of those seven numbers is then normalized to 1. As an example, in the Table 3.1 we give details of those calculations for the $SFR = \exp(0.12 \times \tau)$. While in the Table 3.2 we compare the resulting proportions of stars in each disc subcomponent (SFR intensities) for the four SFR scenarios we have tested in the model.

In the subsection 2.2.2 we have explained how the values of $SFR(i)$ enter the process of density calculations and normalization and pass the information on the SFR to the simulations.

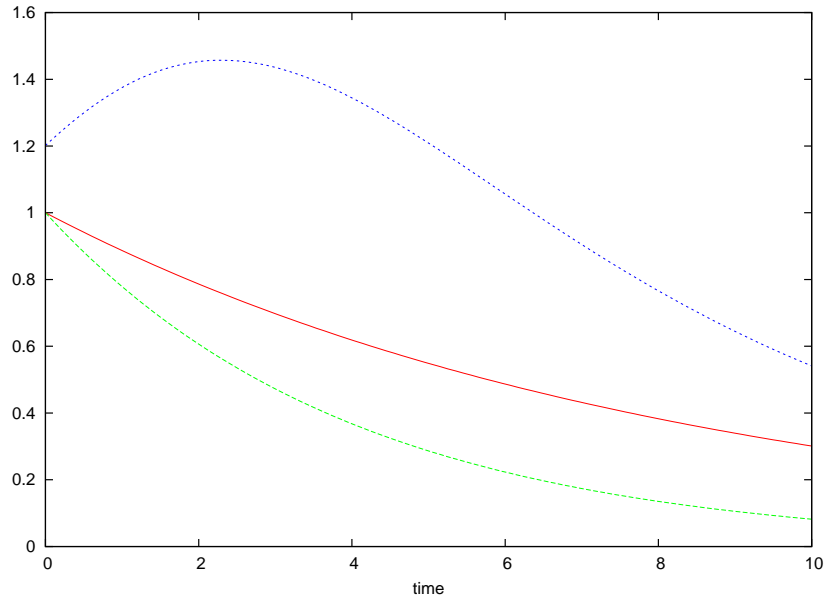


Figure 3.3: Three functions chosen to represent a decreasing SFR as a function of time t . In blue the SFR of the model A of Just and Jahreiß (2010), in red a simple exponential with the γ value 0.12 (proposed by Aumer and Binney (2009)) and in green an exponential with the γ value of 0.25.

decreasing SFR = $\exp(0.12 \cdot \tau)$				
$x_c(i)$ [Gyr]	$\exp(0.12 \cdot x_c(i))$	ageBINsize [Gyr]	SFRnotNorm	SFR normalized
0.075	1.0090	0.15	0.1513	0.0078
0.575	1.0714	0.85	0.9107	0.0472
1.5	1.1972	1	1.1972	0.0621
2.5	1.3498	1	1.3498	0.0700
4.0	1.6161	2	3.2321	0.1677
6.0	2.0544	2	4.1088	0.2132
8.5	2.7732	3	8.3196	0.4317

Table 3.1: Calculating the proportions of stars in each disc subcomponent in case of decreasing SFR.

3 decreasing SFRs				constant SFR
age bin	$\exp(0.12*\tau)$	$\exp(0.25\tau)$	model A SFR from Just and Jahrei (2010)	constant
1	0.0078	0.0034	0.0073	0.015
2	0.0472	0.0215	0.0453	0.085
3	0.0621	0.0331	0.0627	0.1
4	0.0700	0.0425	0.0743	0.1
5	0.1677	0.1237	0.1884	0.2
6	0.2132	0.2033	0.2398	0.2
7	0.4317	0.5716	0.3818	0.3

Table 3.2: The SFR intensities of the four scenarios we have tested.

3.3 Evolutionary tracks sets

In subsequent versions of the Besançon Galaxy Model different evolutionary tracks were used. The Table 3.3 lists different sets, which have been applied since 1986 with the corresponding references.

Evolutionary tracks in BGM	
model version	evolutionary tracks references
Robin and Crézé (1986)	Mengel et al. (1979) for $M < 3 M_{\odot}$; Sweigart and Gross (1978) for the giants; Becker et al. (1977) for $3 - 15 M_{\odot}$ and Chiosi et al. (1978) for $M > 15 M_{\odot}$;
Robin et al. (2003)	(see Haywood et al. (1997a)) Schaller et al. (1992) for stars $M > 1 M_{\odot}$; Vandenberg (private communication) smaller masses; Castellani et al. (1992) for helium-burning stars at masses $1 - 1.7 M_{\odot}$;
new model package A	Chabrier and Baraffe models previous to publication in 1997 for $M < 0.6 M_{\odot}$; Bertelli et al. (1994) for $0.6 M_{\odot} < M < 120.0 M_{\odot}$ (Bertelli et al. (1994) published the isochrones from the evolutionary tracks computed by the Padova group, see http://pleiadi.pd.astro.it/#data2)
new model package B	Chabrier and Baraffe (1997) models for low-mass stars with $M < 0.7 M_{\odot}$; Bertelli et al. (2008) and Bertelli et al. (2009) for high masses with $0.7 M_{\odot} < M < 20 M_{\odot}$; Bertelli et al. (1994) for $20 M_{\odot} < M < 120.0 M_{\odot}$;

Table 3.3: Evolutionary tracks used in subsequent versions of BGM.

In our new model the user has the option of choosing between two evolutionary tracks sets, package A and B. It reflects our progress when updating the model's inputs. At the first moment we have updated the tracks to the package A and later on we have incorporated the newest tracks in the package B.

In Table 3.4 and 3.5 we specify the details of the evolutionary tracks package A.

In order to select the set of new evolutionary tracks from Padova models (Bertelli et al. (2008) and Bertelli et al. (2009)) we have assumed a universal helium enrichment law and the

The main sequence evolutionary models, Padova [1993, 1996].

metallicity sets	available masses [M_{\odot}] (the same for all sets)
$z=0.0004, y=0.23$	0.6, 0.7, 0.8, 0.9, 1.0, 1.1, 1.2,
$z=0.004, y=0.24$	1.3, 1.4, 1.5, 1.6, 1.7, 1.8, 1.9,
$z=0.008, y=0.25$	2.0, 2.5, 3.0, 4.0, 5.0, 6.0, 7.0,
$z=0.02, y=0.28$	9.0, 12.0, 15.0, 20.0 40.0 60.0
$z=0.05, y=0.352$	100.0, 120.0

Table 3.4: The available masses of main sequence and giant branch models of Padova evolutionary tracks, which we have used in the package A.

following linear (Z,Y) relation:

$$Y = Y_p + (\Delta Y / \Delta Z) \times Z. \quad (3.6)$$

Recently, Casagrande et al. (2011) when discussing the chemical evolution of the solar neighbourhood gave constraints for the selection of the best set of (Z,Y) values. Similarly as in that paper, we will proceed as follows:

1. Assume the solar values (Z,Y)=(0.017, 0.26) from Grevesse and Sauval (1998).
2. Fix the slope ($\Delta Y / \Delta Z$) to 2.1 value, which is consistent with the value derived from the studies of metal-rich local K dwarfs (Casagrande et al. (2007)).
3. Derive the Y_p from Eq. 3.6 obtaining $Y_p=0.02243$.
4. Compute the Y values for each of the Z values we had in package B, using the Y_p value.
5. If the derived Y is smaller than 0.23, a value equal to 0.23 is imposed.

The sets of models used in package B are shown in Table 3.6, 3.7 and 3.8.

The Chabrier and Baraffe (1997) low-masses and Bertelli (2008, 2009) high-masses models overlap. We have decided to use the Bertelli sets if the mass $\geq 0.7M_{\odot}$ and Chabrier's models if it is lower. In order to achieve the continuity of solutions on the HR diagram, the $0.7M_{\odot}$ evolutionary track of Chabrier's set was replaced by the Bertelli's solutions for that mass.

The horizontal branch evolutionary models, Padova [1993, 1996].

metallicity sets	available masses [M_{\odot}] (the same for all sets)
z=0.0004, y=0.23 z=0.004, y=0.24 z=0.008, y=0.25 z=0.02, y=0.28 z=0.05, y=0.352	0.5, 0.7, 0.9, 1.0, 1.1, 1.3, 1.5, 1.7, 1.9,

Table 3.5: The available masses of the horizontal branch models (during the core He burning phase) of Padova [1993, 1996]., which we have used in the package A of evolutionary tracks.

The main sequence and giant branch evolutionary models, Bertelli (2008, 2009).

metallicity sets	available masses [M_{\odot}] (the same for all sets)
z=0.0004, y=0.23 z=0.004, y=0.23 z=0.008, y=0.23 z=0.017, y=0.26 z=0.04, y=0.30	0.6, 0.7, 0.8, 0.9, 1.0, 1.1, 1.2, 1.3, 1.4, 1.5, 1.6, 1.7, 1.8, 1.9, 2.0, 2.2, 2.5, 3.0, 3.5, 4.0, 4.5, 5.0, 6.0, 7.0, 8.0, 10.0, 12.0, 15.0, 20.0

Table 3.6: The available masses of the main sequence models of Bertelli et al. (2008) and Bertelli et al. (2009), which we have used in the package B of evolutionary tracks.

The HB evolutionary models, Bertelli (2008, 2009).

z=0.0004 y=0.23	z=0.004 y=0.23	z=0.008 y=0.26	z=0.017 y=0.26	z=0.040 y=0.30
-	-	-	2.0	2.0
-	-	1.9	1.9	1.9
-	1.8	1.8	1.8	1.8
1.7	1.7	1.7	1.7	1.7
1.6	1.6	1.6	1.6	1.6
1.5	1.5	1.5	1.5	1.5
1.4	1.4	1.4	1.4	1.4
1.3	1.3	1.3	1.3	1.3
1.2	1.2	1.2	1.2	1.2
1.1	1.1	1.1	1.1	1.1
1.0	1.0	1.0	1.0	1.0
0.9	0.9	0.9	0.9	0.9
0.8	0.8	0.8	0.8	0.8
0.7	0.7	0.7	0.7	0.7
0.65	0.65	0.65	0.65	0.65
0.6	0.6	0.6	0.6	0.6
0.55	0.55	0.55	0.55	0.55

Table 3.7: The available masses of the the horizontal branch models of Bertelli et al. (2008) and Bertelli et al. (2009), which we have used in the package B evolutionary tracks.

The low-masses main sequence evolutionary models, Chabrier and Baraffe (1997).

metallicity sets	available masses [M_{\odot}] (the same for all sets)
z=0.0006, y=0.25	0.09, 0.1, 0.11, 0.15,
z=0.006, y=0.25	0.2, 0.3, 0.35, 0.4,
z=0.02, y=0.275	0.5, 0.6, 0.7, 0.8

Table 3.8: Details of the Chabrier and Baraffe (1997) models low-masses main sequence evolutionary models used in our model package A and B.

3.4 Binarity

In the scheme adopted from Arenou (2010) the probability of a star to be a binary or single object depends on the object's mass and luminosity class. If the star is on the main sequence he proposes the following probability function

$$f(M_1) = 0.8388 \tanh(0.688M_1 + 0.079), \quad (3.7)$$

where M_1 the mass of the primary. Through the private communication with F. Arenou we have updated the parameters of the expression

$$f(M_1) = 0.85 \tanh(0.55M_1 + 0.095) \quad (3.8)$$

and this formula was implemented in our model. Following the same author we have fixed the probability to 60 % if a star is a giant. The separation of the system is estimated from the distribution of semi-major axis observed in binary systems. For solar type stars the distribution of semi-major axis a is taken from the classical Duquennoy and Mayor (1991) log-normal distribution ($\log a, 1.5, 1.5$) expressed in AU. For brown dwarf binaries a Gaussian($\log a, 0.5, 0.5$) from Close et al. (2003) is assumed and a Gaussian ($\log a, 1, 1$) from Sterzik and Durisen (2004) is applied to M stars.

3.5 Atmosphere models

In our research we have tried three approaches to atmosphere models. First of all we have considered the BaSeL stellar spectral energy distribution (SED) libraries. There are two versions currently in use: the BaSeL 2.2 library (Lejeune et al. (1997), Lejeune et al. (1998)) and the BaSeL 3.1 library (Westera et al. (2002)). As authors explain these are theoretical libraries recalibrated using empirical photometric data, therefore they are called semi-empirical libraries. In the calibration of BaSeL 2.2 library photometric data from solar metallicity stars was used, while BaSeL 3.1 was calibrated metallicity-dependently applying photometric data from globular clusters.

The BaSeL 2.2 and BaSeL 3.1 are comprehensive hybrid libraries based on other original grids of atmosphere models. Since a lot of people are working in that field and various models are being constructed, covering different ranges of stars parameters, the BaSeL team aimed not to create from the beginning their own library, but to collect the best models available at present and merge them into one more complete stellar library.

In the Lejeune et al. (1997) and Lejeune et al. (1998) the team explains that the BaSeL 2.2 stellar library is a compilation of:

1. Kurucz (1995)
2. Bessell et al. (1989,1991)
3. Fluks et al. (1994)
4. Allard & Hauschildt (1995) for the M dwarfs.

Its 3D graphical representation taken from Lejeune et al. (1998) is shown in Fig. 3.4. Two sets of BaSeL 2.2 were published, one corresponds to corrected colours and the other to non-corrected colours. The first one is used in BGM.

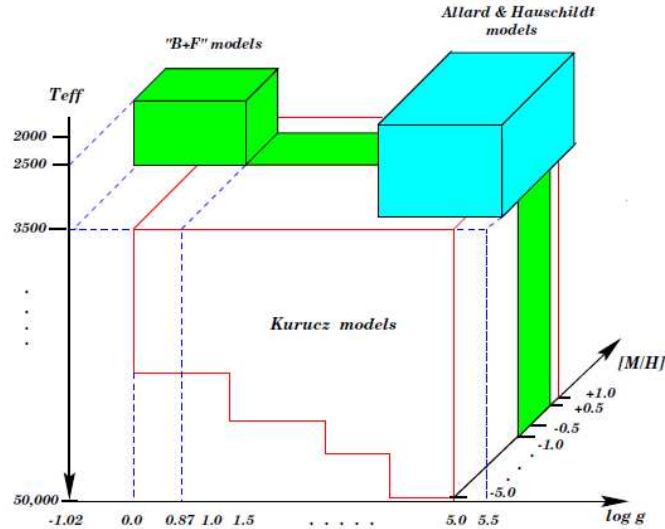


Fig. 1. Coverage of the final combined library in the stellar parameter space. "B+F" models are those constructed for M giants from Fluks *et al.* and BBSW spectra (see LCB97).

Figure 3.4: The BaSeL 2.2 presented in Lejeune et al. (1998). A compilation of other original grids of atmosphere models.

In Westera et al. (2002) the authors explain that although the BaSeL 2.2 library has been applied very widely and successfully in various areas, it shows a weakness at low metallicities. It results from the fact that it was calibrated from solar metallicity data only and it does not perform well at low metallicities ($[\text{Fe}=\text{H}] < -1$). That weakness was corrected in Westera et al. (2002) by extending the colour-calibration to low metallicities. The authors have constructed the new libraries of theoretical stellar energy distributions combining the Kurucz 1995, Allard & Hauschildt 1995 and Scholz 1997 models. To correct for the weakness of the previous version, BaSeL 3.1 libraries have been (UBV RIJHKL) colour-calibrated independently at all levels of metallicity, using the data from the Galactic globular clusters. In our work we use the BaSeL 3.1 "WLBC 99", which reproduces empirical colour-temperature relations and thus is recommended as a tool for investigations on a stellar level and to compare with real observations.

In our new Besançon Galaxy Model the user can choose between the BaSeL 2.2 and BaSeL 3.1 atmosphere models. Alternatively we have also checked the performance of the MARCS grid (Houk et al. (2000)), but only for the giants. Implementing the third option of atmosphere models we combined the solutions of giants from MARCS with BaSeL 3.1 for the rest of stars. It was a very simple treatment and was dictated by our preliminary results, which were showing discrepancies in the colour distribution of giant stars, see section 5.2.7.

3.6 Age-metallicity relation

The values of the age-metallicity distribution we were using at the beginning of our research are given in the Table 3.9 and they come from Twarog (1980). According to the recent work in that field they are far too low, thus we decided to update them. We also found it necessary to change the mechanism of assigning metallicity to stars. The way in which the age-metallicity relation was handled in the model up to now was such that each age bin had a mean metallicity and a dispersion assigned. Consequently for a star belonging to a given age group a value of metallicity was drawn from a corresponding Gaussian distribution. This is why the resulting age-metallicity relation of our simulations had a step-like form. We decided to change that algorithm and draw the value of metallicity taking into consideration the particular age of the star.

	Age-metallicity relation used up to now.						
ageBin [Gyr]	0-0.15	0.15-1	1-2	2-3	3-5	5-7	7-10
mean [Fe/H]	0.150	0.120	-0.050	-0.100	-0.170	-0.280	-0.500
mean σ	0.120	0.120	0.100	0.110	0.180	0.170	0.200

Table 3.9: Age-metallicity relation from Twarog (1980).

We went to the paper of Haywood (2006) where he revises the Galactic chemical evolution and derives a new form of the age-metallicity distribution (AMD). It has changed significantly and compared to the one we were using up to now is almost flat. In Fig. 3.5 we have copied Fig. 13 c of Haywood (2006) where the new determination of AMD is presented.

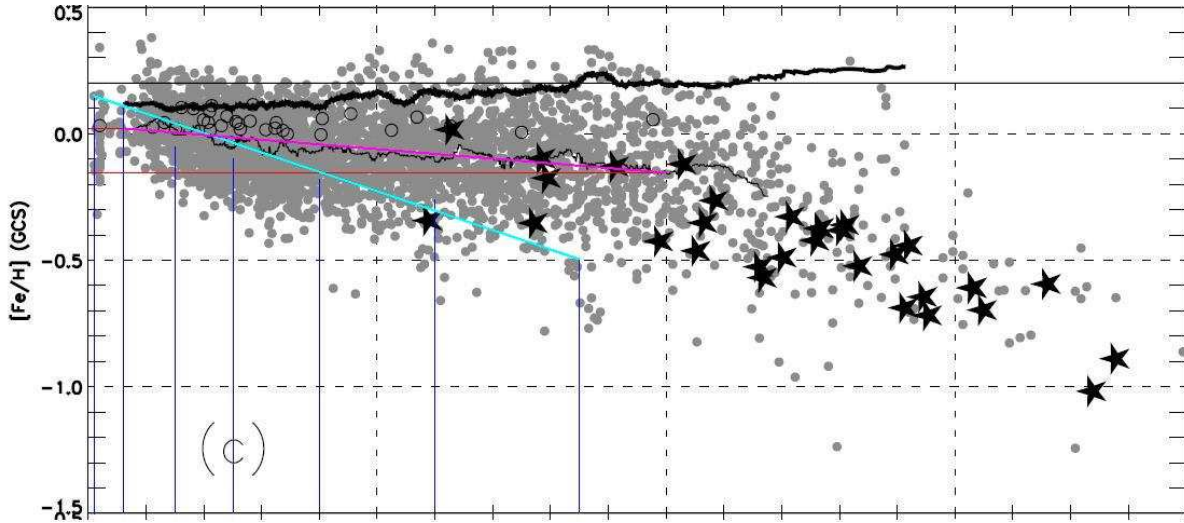


Figure 3.5: **Fig. 13 c) from Haywood (2006). New age-metallicity determination.** The thick curve is the dispersion in metallicity. The solid stars are the thick-disc stars. The thin black line is the new age-metallicity distribution. The violet line is a straight line we have fitted to the new AM curve of Haywood (2006a). The blue line is a approximation of the Twarog (1980) age-metallicity relation (Table 3.9), the BGM used before.

We have fitted the lines to given AMD and dispersions curves and approximated the new

Haywood (2006) age-metallicity relation by:

$$[\text{Fe}/\text{H}] = -0.016 * \text{age} + 0.01 \quad (3.9)$$

and the dispersions curve by

$$\sigma_{[\text{Fe}/\text{H}]} = 0.010 * \text{age} + 0.1. \quad (3.10)$$

Then we have changed the way of assigning the $[\text{Fe}/\text{H}]$ of stars, in such a way that once the age of the star is drawn the metallicity and its dispersion are drawn from those two functions, which are equations of straight lines, Eq. 3.9 and 3.10. In order to test our new algorithm of assigning the metallicity we have fitted a straight line to the previously used age-metallicity relation as well. This is what the light blue line in Fig. 3.5 corresponds to. The same was done for the dispersions in metallicity.

The following equations have been obtained

$$[\text{Fe}/\text{H}] = -0.077 * \text{age} + 0.156 \quad (3.11)$$

and

$$\sigma_{[\text{Fe}/\text{H}]} = 0.010 * \text{age} + 0.1192. \quad (3.12)$$

The outputs of the three following options are compared in Fig. 3.6:

1. the old values of age-metallicity relation (Table 3.9) and the old way of assigning metallicity (seven Gaussian distributions for seven age bins)
2. a line fitted to the old age-metallicity relation (light blue line in Fig. 3.5) and the new way of assigning metallicities (drawing $[\text{Fe}/\text{H}]$ for a specific star's age)
3. a line fitted to the new values of age-metallicity relation (violet line in Fig. 3.5) and the new way of assigning metallicity (drawing $[\text{Fe}/\text{H}]$ for a specific star's age).

The new mechanism of assigning the metallicity diminishes the step-like form and smooths out the resulting relation. In the case of options 1 and 2 we produce almost the same Gaussian distribution (blue and magenta distributions), while for the option 3 the distribution is much different, narrower and shifted towards higher metallicities (red distribution).

The new scheme of metallicity drawing gives much better distributions. This is why we have adopted it together with the new age-metallicity relation from Haywood (2006).

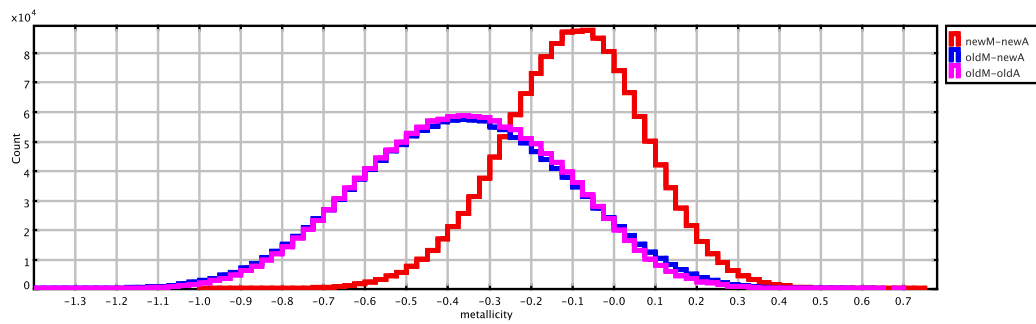


Figure 3.6: Example metallicity distributions resulting from the three options, in magenta and blue options 1 and 2 respectively and in red option 3.

3.7 Dynamical mass and age-velocity relation

Each time that any of the evolutionary parameters of the model (IMF, SFR, evolutionary tracks) is changed the Galactic gravitational potential must be recalculated. We have explained that procedure in the subsection 2.2.2. There are two input parameters derived from observations, which enter the equations in that process of potential recalculation. They are the total dynamical mass density and the values of the age- σ_W velocity dispersion relation, where W is the velocity perpendicular to the Galactic plane.

3.7.1 Dynamical mass

In the model version from Robin et al. (2003) the authors have set the value of the dynamical mass to the one of Cr ez e et al. (1998) and they have used the age- σ_W velocity dispersion relation from G omez et al. (1997). In our work we have enriched the options for those input parameters.

In van Leeuwen (2007) the author has published the new reduction of the Hipparcos data. He has recalculated the value of the total dynamical mass in the solar neighborhood, finding it about 60 per cent higher than the one from Cr ez e et al. (1998):

- M. Cr ez e $0.076 \pm 0.015 M_\odot/pc^3$
- F. van Leeuwen $0.122 \pm 0.019 M_\odot/pc^3$.

In practice, to apply the F. van Leeuwen dynamical mass we have increased the mass density of the interstellar medium, from the previous value of $0.02M_\odot/pc^3$ to the value $0.05M_\odot/pc^3$, as proposed by Binney and Tremaine (2008).

We have set the densities of all mass components as follows:

- thin disc: $0.039 M_\odot/pc^3$ or $0.033 M_\odot/pc^3$
- thin disc white dwarfs: $0.00714 M_\odot/pc^3$
- thick disc: $0.243 \times 10^{-2} M_\odot/pc^3$
- stellar halo: $0.92 \times 10^{-5} M_\odot/pc^3$
- ISM: 0.02 or $0.05 M_\odot/pc^3$
- dark halo: it is recomputed from the process.

Once the density of the dark halo is established in the potential recalculation process one can add up the mass of all components. Depending on which density was assumed for the ISM one will get a total mass density within the error bars of one or the other reference value (Cr ez e et al. (1998) or van Leeuwen (2007)). In our work we have tried both values of that parameter, see section 5.2.10.

In our model the local mass density of the thin disc stellar component is a critical parameter. In Table 3.10 we show three different values of that parameter derived from observations. In section 5.2.1 we show the results of our simulations when these values for the local stellar mass density are applied.

source	Wielen (1974)	Jahreiß and Wielen (1997)	Reid et al. (2002)
main sequence	0.037	0.0323	0.0300-0.0338
giants	0.001	0.0006	
WD	0.007	0.0053	0.004
total	0.045	0.039	

Table 3.10: The values of the thin disc local stellar mass density derived from observations. All values are given in M_{\odot}/pc^3 .

The way in which the local stellar mass density is distributed over the seven subcomponents of the thin disc changes slightly each time that the evolutionary parameters of the model are modified. That is why here we will not specify any exact values for the disc subpopulations, but we just remind that the thin disc cumulative contribution to the total mass density is one of the values.

3.7.2 Age-velocity dispersion relation

In Fig. 3.7 we present the original Fig. 7 of Holmberg et al. (2009) where the authors show the age - σ_W velocity dispersion relation they have obtained. From that plot we have estimated the velocity dispersion σ_W for each age bin of our model.

The values of velocity dispersion in the perpendicular direction σ_W derived for the seven thin disc subcompomponents of our model from the age - σ_W relations of Gómez et al. (1997) and Holmberg et al. (2009) are compared in the Table 3.11.

We have applied both sets of values in our simulations and investigated what is the impact of that parameter on the resulting stars counts and compared the results with the observations, see section 5.2.11.

component of the disc	Age [Gyr]	Gómez et al. (1997) σ_W [km/s]	Holmberg et al. (2009) σ_W [km/s]
1	0-0.15	6.0	6.0
2	0.15-1	8.0	8.0
3	1-2	10.0	10.0
4	2-3	13.2	14.0
5	3-5	15.8	17.5
6	5-7	17.4	21.0
7	7-10	17.5	25.0

Table 3.11: The comparison of the σ_W values derived for the model's thin disc subcompomponents from the age - σ_W relation presented in Gómez et al. (1997) and Holmberg et al. (2009).

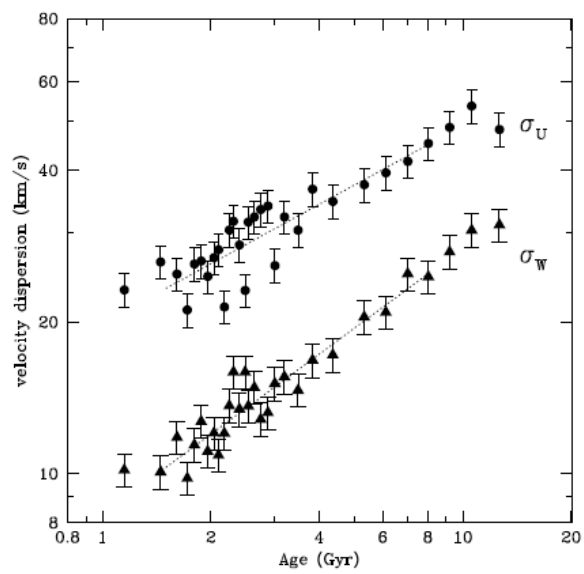


Figure 3.7: It is Fig.7 of Holmberg et al. (2009) showing their σ_W - age relation.

Chapter 4

Observables and tools

In this chapter we present the observables we work with and describe the tools, which have been developed in order to optimize the comparison between the model and data. We decided to constrain our simulations by two observational sets, the local luminosity function and the Tycho-2 data up to magnitude $V_T = 11.0$. Each time that any of the evolutionary parameters in the model was changed (IMF, SFR or evolutionary tracks) the first step to follow was to check how the new mass model fits the local LF. The simulations with the sphere mode were performed (see section 2.4) and using them the synthetic LF was calculated for each model and compared with the observed LF. Secondly we were interested how each of these models performs when compared to Tycho-2. Our strategy was to simulate a few particular regions or the entire sky, look at the results in terms of star counts and the $(B - V)_T$ distributions and compare them with data.

4.1 Observables

4.1.1 The local luminosity function

In section 2.2.2 we have discussed that each time that any of the main ingredients of the new BGM has been changed we have determined a new mass model. Then our intention was to test how those different models perform when compared to real data. The first step was to simulate with each model the sphere around the Sun and from that to calculate the synthetic LF. Subsequently we checked how those synthetic luminosity functions fit the observed ones.

Three observational luminosity functions have been used in our research. As the first data set we have used the LF derived by Jahreiß and Wielen (1997) after Hipparcos data was published. The second one is the LF published by Kroupa (2001), which for $M_v < 11.5$ mag was estimated from Hipparcos data and for fainter magnitudes from ground-based parallax data. Both functions are the nearby single star luminosity functions. The third LF we have used in our comparisons was derived by Reid et al. (2002) and it was obtained by combining data for the Hipparcos 25 pc sample and additional astrometric and spectroscopic observations (Palomar/Michigan State University (PMSU) survey) for fainter stars. This LF as the previous ones includes the contribution of single stars, primaries and resolved companions. In Fig. 4.1 we plot the three functions in question.

It has to be commented that on the bright side the three presented functions differ signif-

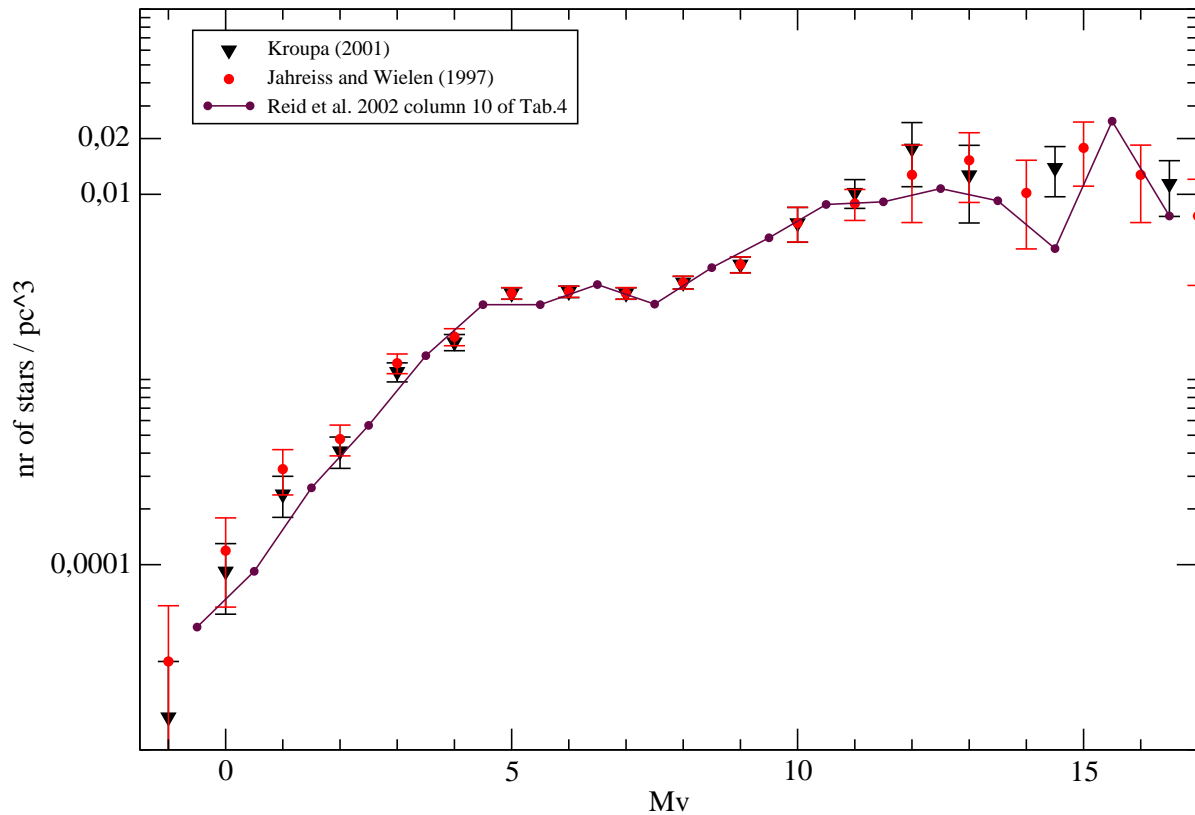


Figure 4.1: Three local luminosity functions derived from observations: in red Jahreiß and Wielen (1997), in black Kroupa (2001) and in violet Reid et al. (2002).

icantly one from another, while all of them are derived from Hipparcos observations. Those discrepancies are caused by the fact that the bright stars are very scarce, so the corresponding observational points were probably derived from few objects. At the same time the bright tail of the LF is compatible with the stars that our Tycho-2 sample contains. The simulations that we perform are magnitude limited ($V_T = 11.0$) and for that our sample falls within the absolute magnitude range $M_V = (0;5)$ mag. Thus it is very interesting that in that range the Tycho-2 data serves us as a stronger constraint and can point out more correct solutions. At the faint end the presented luminosity functions also differ and we do not reach those stars with our Tycho-2 sample. We can constrain them just from the fitting of the synthetic luminosity functions to the observed ones.

4.1.2 The Tycho-2 Catalogue

As explained in the section 1 we aimed in this project to perform whole sky comparisons between the new Besançon Galaxy Model and the real data. The motivation was that until now the model was always being tested against data just in particular regions. As one of our main scientific goals was to study the IMF and SFR functions we found it very interesting to perform the global whole sky analysis when different expressions for these functions are considered. To satisfy the requirements of that task we needed a data set, which is complete and homogenous and such is the Tycho-2 catalogue, Høg et al. (2000). We decided to choose it as our primary data set serving us for intensive comparisons with simulations.

The astrometric reference catalogue, the Tycho-2 Catalogue, provides positions, proper motions, and B_T and V_T magnitudes for the 2.5 million brightest stars across the entire sky. The Tycho-2 data was derived from the original observations collected by the ESA Hipparcos satellite, as was the Tycho Catalogue, but using a new reduction technique. The proper motions are available for nearly all the catalogue stars (96 per cent) with a mean standard error of about 2.5 mas/yr. The completeness of the catalogue is 90 per cent up to magnitude $V_T \sim 11.5$ and 99 per cent up to $V_T \sim 11.0$ magnitude.

Preparation of the Tycho-2 sample for our analysis

In order to perform the comparison of Tycho-2 data with the model we needed to prepare our version of the catalog, meaning to extract the data we were interested in and keep it in a format suitable for the processing. First of all a magnitude selection was done. The criterion was the completeness of the catalog. Stars until magnitude $V_T \sim 11.0$ were chosen (completeness to ~ 99 per cent). The number of objects left for our analysis was 864816. In Fig. 4.2 we have plotted the distribution of selected objects over the whole sky. We extracted from the catalog positions, proper motions and photometry of the stars. In the second step two kinds of data transformations were done. Positions and proper motions have been transformed from the equatorial coordinate system to the Galactic one and the photometry transformations between Tycho and Johnson photometric systems were investigated. We have decided to work in the space of observables, so we have transformed our simulations done in Johnson into the Tycho-2 photometric system. The sky was divided into 472 fields with approximately the same number of objects and for each region we compared the star counts and $(B - V)_T$ colour distributions.

Photometry transformations

In order to find the best transformation between the Johnson and Tycho systems and transform the photometry of our simulations into the space of observables we have followed four different approaches to the photometric transformation in question. The first three transformations were found in the literature and are given to transform from the Tycho-2 system to the Johnson system. Thus first we have compared their performance transforming data to Johnson system, then we chose the best one and inverted it.

In the guide to the Tycho-2 catalog the standard transformation between the Tycho and Johnson Cousins photometric systems is presented

$$V_J = V_T - 0.090(B_T - V_T),$$

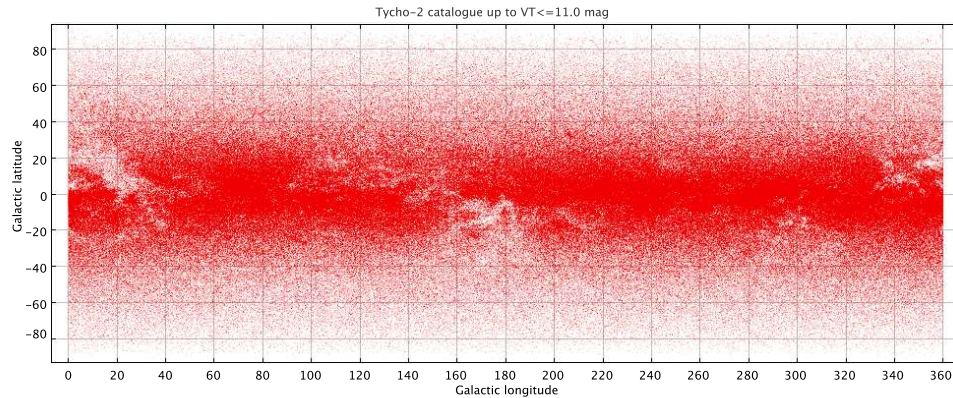


Figure 4.2: The distribution over the sky of the stars we have selected from the Tycho-2 catalogue to compare with the model. Low density regions trace the high interstellar extinction in these directions.

$$B_J - V_J = 0.850(B_T - V_T). \quad (4.1)$$

It was the first method that we have applied. However authors recommend consulting Vol. 1 of ESA (1997) (Sections 1.3 and 2.2) for more details. There they explain that these standard equations are a rough approximation because they impose the same transformation for all types of stars.

Subsequently they suggest a more sophisticated method of transformation, which is the linear interpolation of the values specified in their Table 1.3.4. copied here in Fig. 4.3.

Table 1.3.4. Transformation from the Tycho photometric system to Johnson. The points given can be used in a linear interpolation, with deviations less than 0.005 mag from a more accurate spline fit.

$(B - V)_T$	≤ -0.2	0.1	0.5	1.4	≥ 1.8	
$V_J - V_T + 0.090(B - V)_T$	0.014	0.000	-0.005	-0.005	-0.015	
$(B - V)_J - 0.85(B - V)_T$	-0.006	0.000	0.046	-0.008	-0.032	
G-factor	0.85	0.87	0.97	0.79	0.79	0.85

Figure 4.3: Table1.3.4 from ESA (1997).

This was our second approach to the transformation. In this case the slope of the $(B - V)_J$ versus $(B_T - V_T)$ relation, the so called G-factor is different in each of the six presented colour intervals.

In reality the photometric transformation depends on the detailed spectrum of the star,

especially on luminosity class and interstellar and circumstellar reddening. Different relations for various spectral ranges and luminosity classes are also presented in the ESA (1997) book and consequently one should use them to minimise errors of conversion if one has information about star's luminosity.

When transforming data to Johnson we did not have that information, so we have decided to make use of the following conclusion of the authors: "When no luminosity classification was available, the relation defined for luminosity class III giants was used." Thus our third approach was to use the following equations of giant-like stars (luminosity class III with low reddening) for the whole sample

$$B_T - V_T < 0.65 :$$

$$\begin{aligned} (B_J - V_J) &= (B_T - V_T) - 0.010 - 0.060z - 0.14z^3 \\ z &= B_T - V_T - 0.22 \end{aligned} \quad (4.2)$$

$$0.65 < B_T - V_T < 1.10 :$$

$$\begin{aligned} (B_J - V_J) &= (B_T - V_T) - 0.113 - 0.258z + 0.40z^3 \\ z &= B_T - V_T - 0.95 \end{aligned} \quad (4.3)$$

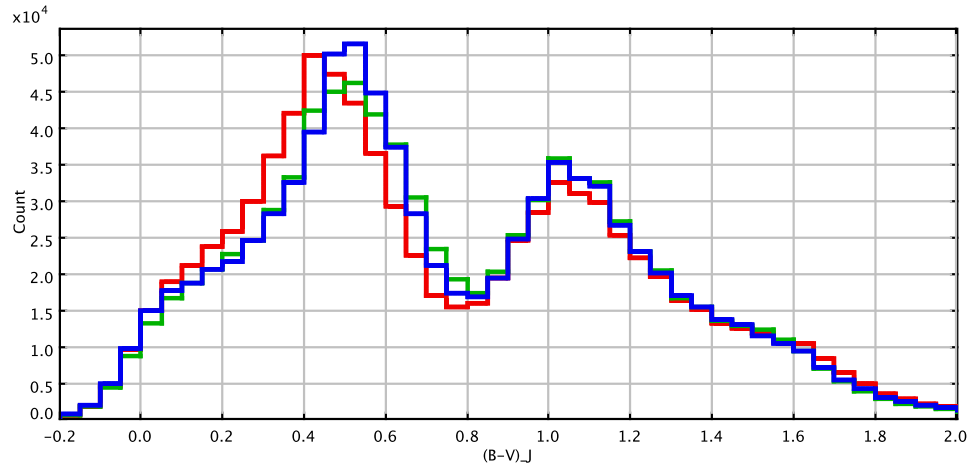
$$1.10 < B_T - V_T :$$

$$\begin{aligned} (B_J - V_J) &= (B_T - V_T) - 0.173 - 0.220z + 0.01z^3. \\ z &= B_T - V_T - 1.20 \end{aligned} \quad (4.4)$$

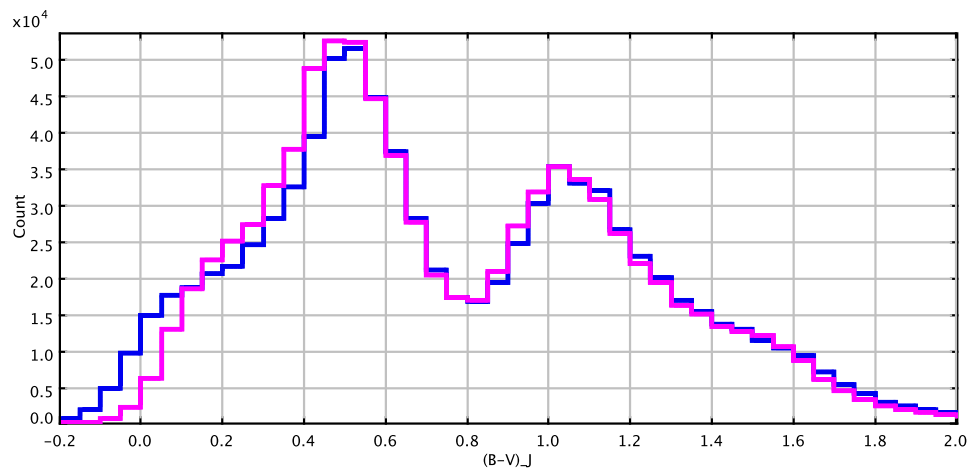
The fourth method of transformation comes from the study of Mark Kidger. On his website (<http://www.britastro.org/asteroids/Tycho%20Photometry.htm>) he derives the following relations:

$$\begin{aligned} (B_T - V_T) &= 1.28899(B_J - V_J) - 0.1031 \\ V_J &= V_T - 0.016 - 0.0741 \times (B_T - V_T). \end{aligned} \quad (4.5)$$

In Fig. 4.4 we present the $(B - V)_J$ distributions of our Tycho sample (cut at $V_T \leq 11$ mag) transformed to Johnson system by the four discussed methods. The giants and interpolation methods show very similar results for the giants peak while in the blue peak of the colour distribution we see some differences. This is of course caused by the fact that using the giants transformation we have transformed the blue peak dominated by main-sequence stars with the equations for giants. The standard transformation, which is less recommended by authors gives the $(B - V)_J$ distribution which is outstanding quite significantly from the remaining transformations. We conclude that the interpolation transformation is the most reliable. When we compare it to the transformation proposed by Mark Kidger, see Fig. 4.4 b), we can notice that they perform differently on the blue side of the colour distribution. That difference can be also seen in Fig. 4.5 b) where we show the comparison of the $(B - V)_J$ versus $(B_T - V_T)$ relation for both methods. In our work we have decided to use the linear interpolation transformation method, so we have inverted it and transformed the photometry of our simulations from Johnson to Tycho-2 system.



a) standard (red), interpolation (blue) and giants (green) methods



b) interpolation (blue) and Mark Kidger's (magenta) methods

Figure 4.4: The $(B - V)_J$ distribution of our Tycho-2 catalogue (after cutting at $V_T = 11$ mag) transformed using four different photometry transformations.

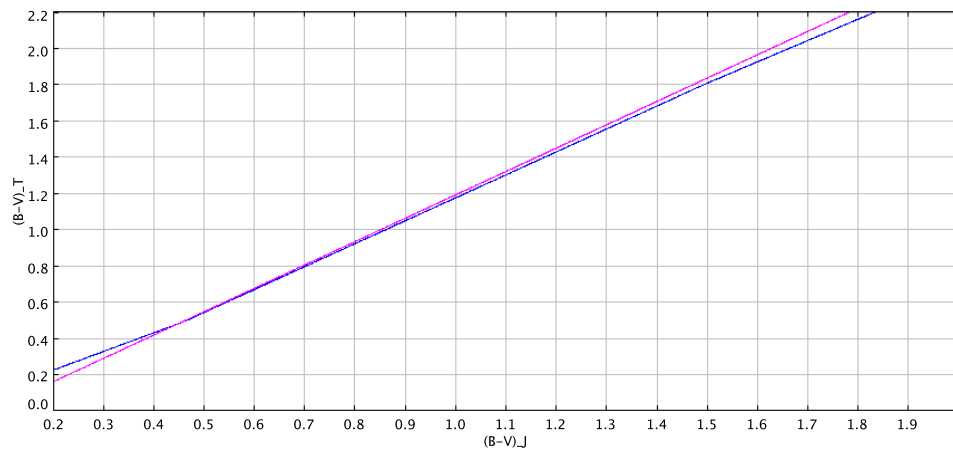


Figure 4.5: The $(B - V)_J$ versus $(B_T - V_T)$ relation of our Tycho sample transformed using two different transformation methods.

4.2 Tools

Different techniques and strategies were designed and applied when comparing the simulated and real data. We were interested not only in looking at small and specific Galactic directions, but also in a more general comparison with a global sky coverage.

At the beginning of our project we have performed the whole sky comparison of the old version of the model and Tycho-2 data. At that time a powerful tool facilitating that task was developed and it was our processing pipeline, see section 4.2.1. The idea was to simulate the whole sky, region by region, and then compare it with our Tycho-2 sample. The clustering algorithm was applied to simulations and data in order to distinguish A and F type main-sequence stars from giants (see section 4.2.2). The final step of the pipeline was to paint the whole sky maps of mean colours and relative number of objects separately for the two groups of stars in order to track the large scale structures (examples of the sky maps in Fig. 5.1 and 5.2 of section 5.1).

Then we have focused on the development of the new model and once it was finished we again wanted to compare it with our Tycho-2 sample. However this time we have significantly enriched the possibilities of different analysis that could be performed. Turning the evolutionary parameters into model's inputs and updating several other ingredients of the model has expanded the field of our investigation. We were interested in testing different scenarios of many inputs of the model and we wanted to check if they can be constrained by Tycho-2 data. At that point our strategy of comparison has changed. It was not needed to perform the whole sky analysis each time that one of the model's ingredients was modified. Additionally, it would be very time consuming task. In most of the cases the simulations towards few regions were sufficient to derive valuable conclusions. Consequently, the comparison between our new model and Tycho-2 data is done in the context of star counts and $(B - V)_T$ distributions for few specific regions, each time that any model's input alters (the strategy we followed in chapter 5). Whenever we have seen that a more general comparison was required we have performed the whole sky analysis, but it concerns few cases. In the future we plan to extend it to more cases. We want to perform the whole sky χ^2 tests for each model presented in chapter 5 and draw the sky maps for them.

In our new model binaries are created by default unless the user specifies differently. As it was explained in section 2.3.2 two catalogues are created during the simulations. One contains single and primary stars of the thin disc and stars of older populations and the second catalogue contains only the secondaries. The merging of binaries is done in the post-processing code, which we shortly describe in the section 4.2.3.

4.2.1 The processing pipeline - whole sky simulations

In order to increase the efficiency of numerous comparisons, a processing pipeline based on C, Java and scripting programming languages has been developed and applied, see Fig. 4.6. It is a fully automated, portable and robust tool, allowing to split the work across several computational units. We are able to repeat all sky processing with different settings of the model. The cluster of the Departament d'Astronomia i Meteorologia (32 nodes) has been used for that purpose. That pipeline can be applied in the future to test the model against any other data catalogue.

The procedure of obtaining the whole sky analysis starts with the division of the sky into regions. Then, for each region from the list the same treatment will be performed. The data from the catalogue is extracted and the simulations are generated. Once both samples are in place

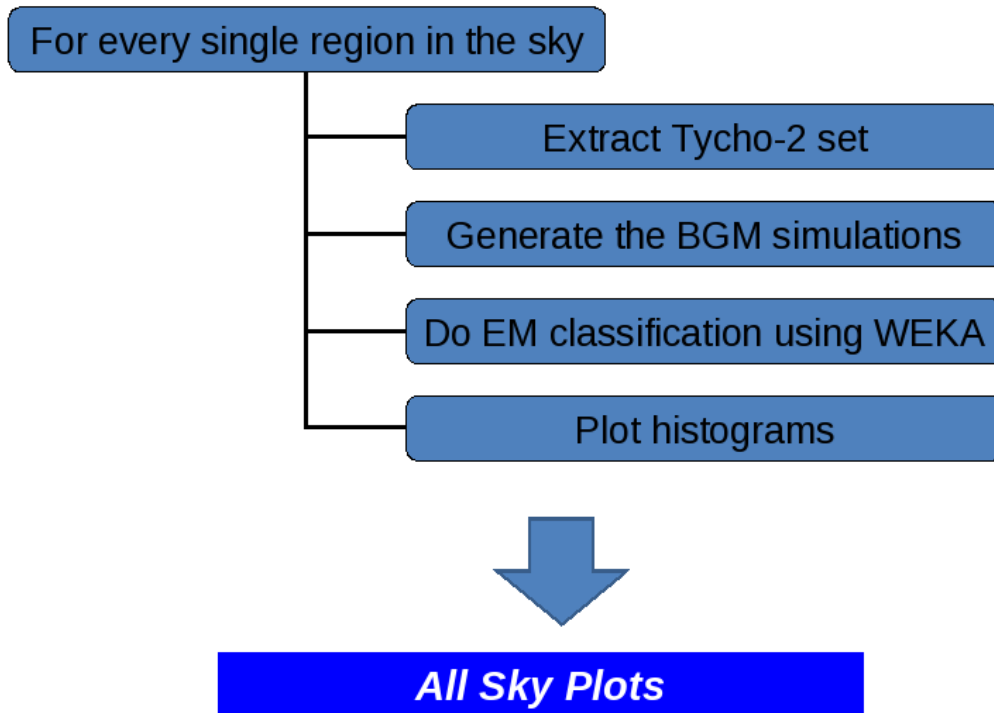


Figure 4.6: Our processing pipeline.

they are converted into a specific format and the clustering is performed in order to distinguish between two different groups of stars we work with, see the subsection below 4.2.2. Afterwards, for each region the colour histogram is plotted. When the calculations are done for the entire sky we do the sky maps using our Java code developed applying the Java Free Chart library (David Gilbert).

4.2.2 WEKA

The $(B - V)_T$ histograms we obtain for each region show a bi-modal distribution. This is because our sample is magnitude selected and we cut at apparent magnitude $V_T = 11$. We get in the colour distribution two peaks corresponding to hot and the cool stars what is easy to understand when looking at the HR diagram and imaging the cut. In the blue peak we mainly have A and F type main-sequence stars, which are on average young, while in the red peak dominate on average old giant stars, but covering a wide age range in fact. We have used the WEKA Software (University of Waikato), a collection of machine learning algorithms for data mining tasks, to perform clustering. More exactly, the separation into two clusters was performed applying the Expectation Maximization (EM) method, which is a part of the software package. This algorithm uses the finite Gaussian mixture model and assumes that all attributes of the sample, which will serve in clustering are independent random variables. A given sample is represented by a mixture of N probability distributions and each distribution is

called a cluster. The method assigns to an individual instance the probability of belonging to a given cluster. The user may specify a priori how many clusters are to be generated or the EM method can decide it by cross validation.

In our work we have used the $(B - V)_T$ data as attributes for clustering, thus the samples were divided according to those values only. In the future it will be possible to provide proper motion information to the algorithm. We imposed two clusters to be created and the whole sky maps were done separately for these two families (hot and cool stars).

4.2.3 Post-processing

The output of the new model are two catalogues, one contains only secondary components of binary systems which have been created and the other contains all the rest of stars. A special code was developed in order to process both catalogues, perform the merging of binaries and other necessary treatments. In section 2.3.2 we already explained how the binary systems are merged. First of all one must assume the resolution of the catalogue, which is going to be produced (also see section 3.4). Then the binaries are processed one by one. During simulations each was assigned a separation and in order to decide if it will be merged or resolved we randomly incline the system and project it on the sky. Subsequently the angular separation is computed and compared to the spatial resolution of the catalogue. If stars are decided to be merged we simply add their fluxes. In the next steps of post-processing the extinction effects and photometric errors are added. Afterwards the Johnson photometry is transformed to Tycho-2 system and additionally the error of photometric transformation is added. In Fig. 4.7 we present a simplified scheme of post-processing.

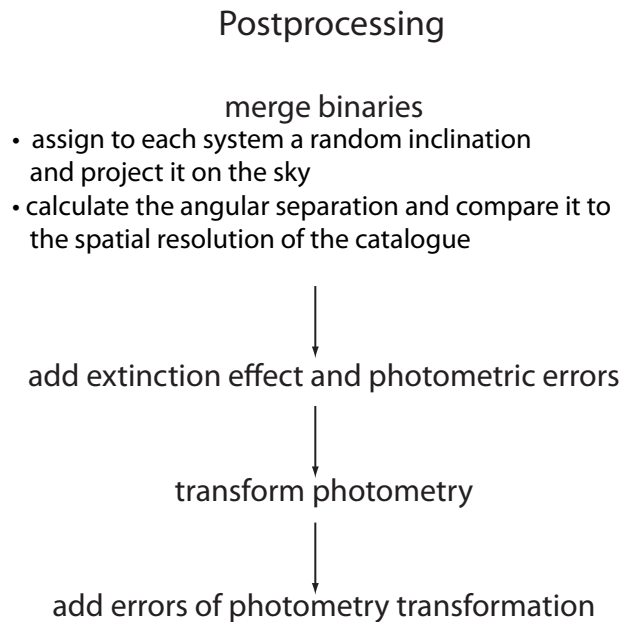


Figure 4.7: The scheme of post-processing applied to our simulated samples.

Chapter 5

Results

In this chapter we firstly show the results of the whole sky comparison between the old model and our Tycho-2 set, which was done at the very beginning of this project (see section 5.1). The methodology we followed in that comparison consists of three parts, the cumulative whole sky $(B - V)_T$ distribution, the fit to the local LF and the whole sky maps of the difference in the mean $(B - V)_T$ and relative number of objects. As it was said in chapter 4 we made a decision to show our colour histograms in Tycho-2 system, thus to transform the photometry of the model into the space of observables.

Afterwards we present our new default model and compare its most important ingredients with those of the old model. Then in section 5.2 we discuss subsequently each ingredient of the new model and the possible values that we have assigned to its parameters. The model's building blocks, which we studied are the local stellar mass density, IMF, SFR, evolutionary tracks, age-metallicity relation, atmosphere models, binarity, the age of the thin disc, thick disc, extinction model, total dynamical mass, age-velocity relation and the scale length of the disc. To investigate what is the impact of each ingredient on the results we have changed subsequently each of them keeping the rest of the inputs fixed as in our default new model. After demonstrating how in our analysis the best values are assigned to all model's inputs we finally arrive to the whole sky comparison between the old and new model and Tycho-2 data, see section 5.3.

The strategy, which has been followed in the comparison of the new model and Tycho-2 data was already discussed in chapter 4, where we present the tools and observational constraints serving us for all analysis. In cases where different scenarios of the thin disc evolution have been tested the fitting to the local LF was performed. In our reasoning we have always considered the single star LF. Whenever any of the model's inputs was modified and we wanted to study its influence on the resulting star counts and colour distributions, the simulations towards three standard regions were performed and compared to data. In the critical cases the whole sky simulations were done and the whole sky comparisons to data was accomplished.

We remind to the reader that our work was constrained to the thin disc only. The other populations are treated in the same way as in the old model.

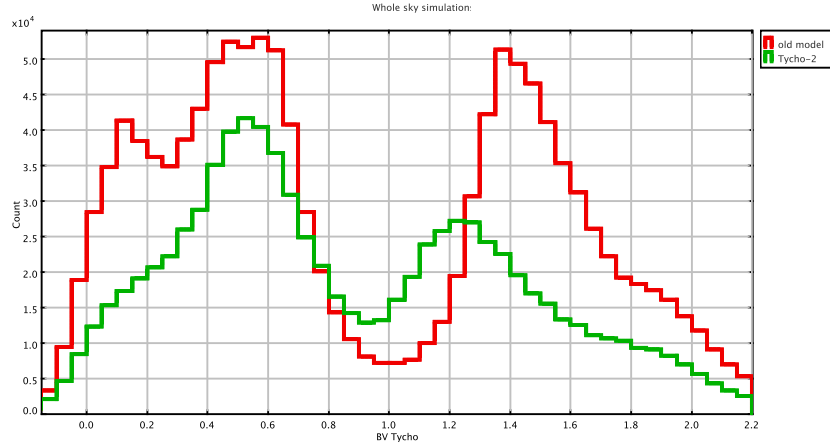
5.1 The old model vs. Tycho-2 vs. new model

In Fig. 5.1 and 5.2 we present the results of comparison between the old model (Robin et al. (2003)) and Tycho-2 data, which were the starting point of our project. We have used the Drimmel and Spergel (2001) extinction model in those simulations.

We show here the cumulative whole sky $(B - V)_T$ distribution of the old model and the Tycho-2 data, the comparison of the synthetic LF produced by the old model with the observed LF and then the sky maps of differences of mean colour and relative number of objects drawn separately for two groups of stars found in our sample (blue mainly main-sequence and red mainly giant stars). In section 4.2.2 we have explained that those two peaks were separated applying a clustering algorithm.

When comparing the old model to Tycho-2 data we can notice several discrepancies:

1. The red peak of the $(B - V)_T$ distribution is shifted of about 0.2 mag.
2. The excess of the total number of stars; the model produces two times more stars than our Tycho-2 sample in spite that the data sample is complete until $V_T = 11$ mag.
3. The excess of the blue stars around $(B - V)_T \sim 0.15$ mag.
4. The presented comparison of the observed and simulated LF (from Robin et al. (2003)) points out the importance of the slope of IMF at low masses. We remind that a constant SFR was assumed in that version of BGM. The figure starts at $M_V = 5$ mag, so it does not show all the range corresponding to our Tycho stars.
5. The Galactic plane is obviously the most problematic zone due to high interstellar extinction and its nonuniform distribution. The differences in the mean colour between the model and data $\Delta(B - V)_T$ reach 0.5 mag. The relative number of objects $((\text{BGM-Tycho})/\text{Tycho})$ can reach a factor up to 7. The discrepancies in the mean colours are correlated with the discrepancies in the relative number of objects. A higher relative number of objects (more objects simulated by the BGM than observed in Tycho-2) corresponds to bluer mean colour of that region.



A. C. Robin et al.: Structure and evolution of the Milky Way

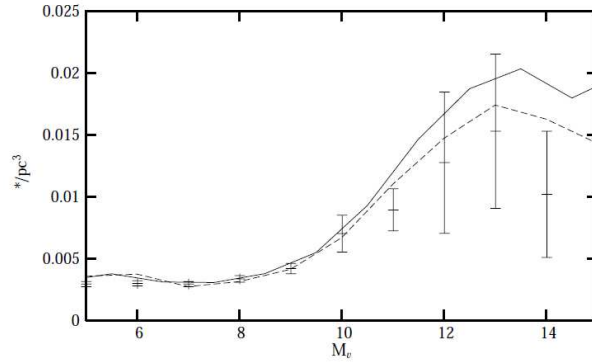


Fig. 1. Luminosity function in the V band in the solar neighbourhood. Crosses with Poisson errors: Jahreiss determination from the revised Catalogue of Nearby Stars; Lines: model LF assuming an IMF slope of $\alpha = 1.7$ (solid line) and 1.6 (dashed line) at $m < 1 M_{\odot}$.

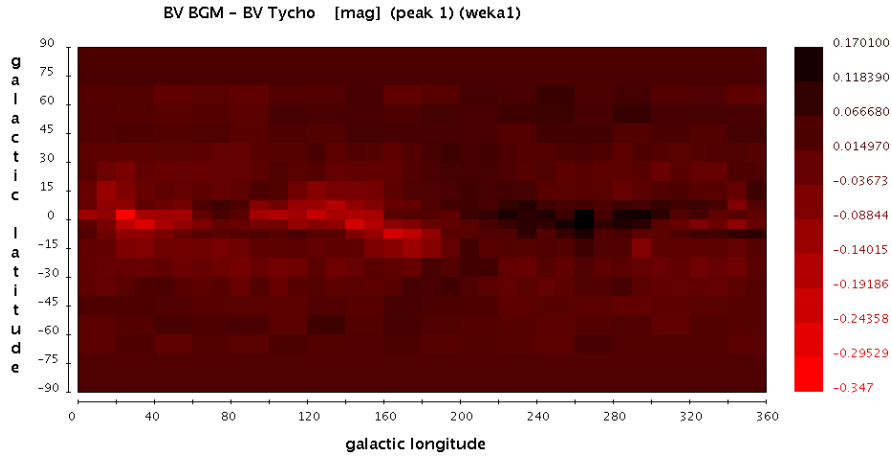


Figure 5.1: Top: cumulative whole sky $(B - V)_T$ distribution of the old model and the Tycho-2 data up to magnitude $V_T = 11$; middle: Comparing the LF of the old model (the dashed line) with the local LF (figure from Robin et al. (2003)); bottom: the map of the differences in the mean $(B - V)_T$ colour between the old BGM model and data for the stars belonging to the blue peak of our colour distribution (mainly A and F type main-sequence stars). The two peaks were separated applying a clustering algorithm, see section 4.2.2.

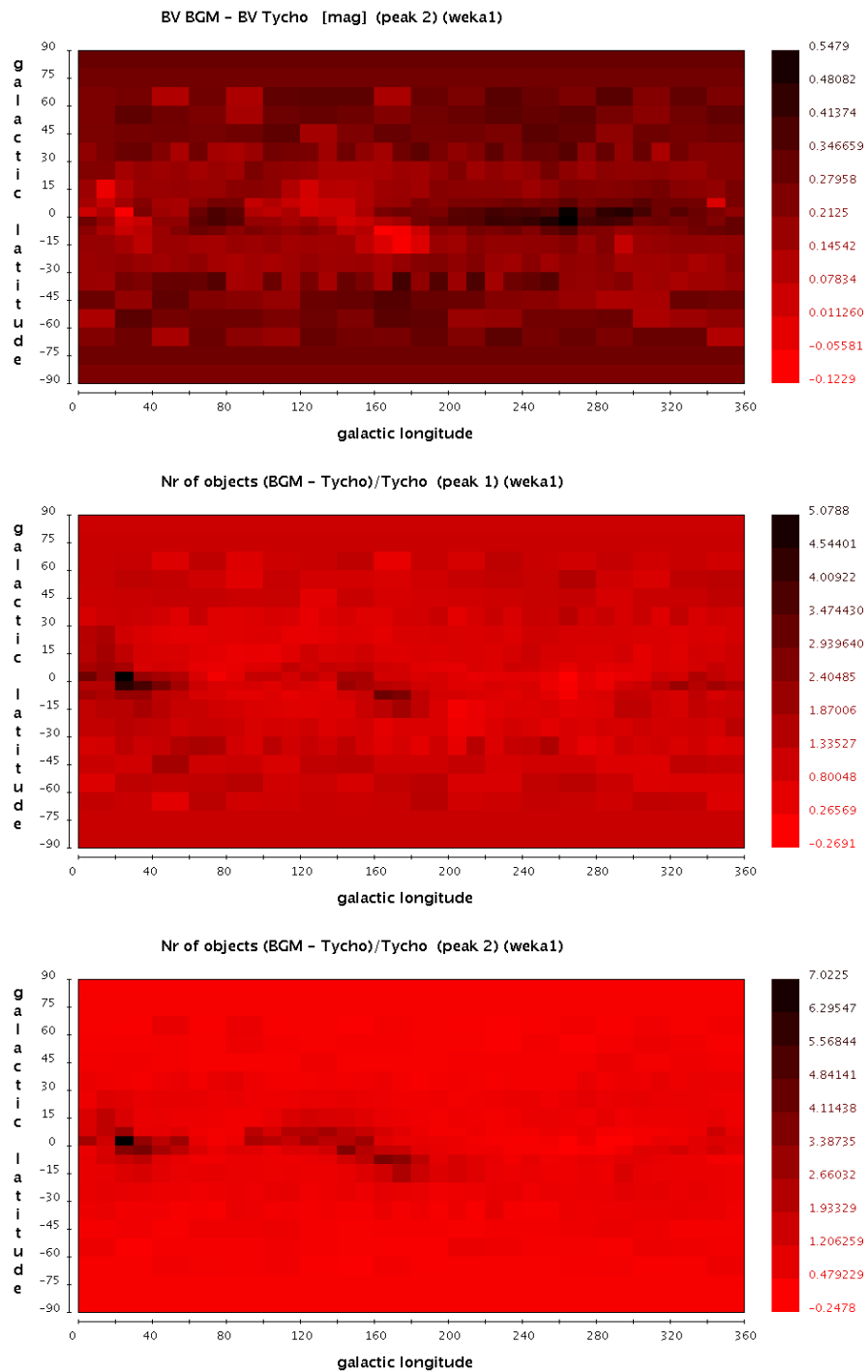


Figure 5.2: The sky maps where the old BGM model is compared to Tycho-2 data. Top: the map of the differences in the mean $(B - V)_T$ colour between the old BGM model and data for the stars belonging to the red peak of our colour distribution (mainly giants); middle: The relative number of objects $((BGM - Tycho)/Tycho)$ corresponding to the blue peak of $(B - V)_T$ distribution. Bottom: The relative number of objects $((BGM - Tycho)/Tycho)$ corresponding to the red peak of $(B - V)_T$ distribution.

In the Table 5.1 we show the list of model's most important ingredients, which were under study and then specify the values that were assigned to them in the old and new model.

Ingredients	old model	new model (default)
IMF	Haywood-Robin IMF	Haywood-Robin IMF (A) Kroupa-Haywood v6 (B)
SFR	constant	a decreasing $\exp(-0.12\tau)$ SFR from Aumer and Binney (2009)
evolutionary tracks	see Table 3.3	see package B Table 3.3
age-metallicity relation	Twarog (1980)	Haywood (2006)
atmosphere models	BaSeL 2.2	BaSeL 3.1
binarity	no	yes: the scheme adopted from Arenou (2010)
age of the thin disc	10 Gyr	10 Gyr
thick disc parameters	$x_l = 400$ pc, $h_z = 800$ pc density = $8.33e-3$ */pc ³	$x_l = 400$ pc, $h_z = 800$ pc density = $8.33e-3$ */pc ³
extinction model	Drimmel and Spergel (2001) ¹	Marshall et al. (2006) + Drimmel and Spergel (2001)
total dynamical mass	Crézé et al. (1998)	van Leeuwen (2007)
local stellar mass density	Wielen (1974)	Wielen (1974)
age-velocity relation	Gómez et al. (1997)	Gómez et al. (1997)
warp	Reylé et al. (2009)	Reylé et al. (2009)
scale length	young disc $h_R = 5000.0$ pc old disc $h_R = 2400.0$ pc	young disc $h_R = 5000.0$ pc old disc $h_R = 2400.0$ pc

Table 5.1: The list of the most important ingredients of the old and new model which were investigated. ⁽¹⁾ In the BGM from Robin et al. (2003) the Drimmel and Spergel (2001) extinction model was not used, but it was used in our simulations with the old model performed in 2009.

The ingredients presented for the new model compose our default version. Thus, whenever we refer to the default model we mean our new model with the ingredients presented in Table 5.1. Because there are two IMF that we favour (see section 5.2.2) we may refer to the default

model A or B depending which of them was assumed in simulations.

In section 2.2.2 we explain that when any of the model's ingredients is changed the definition of the model changes and the new mass model has to be derived. The process of determination of the new mass model in BGM consists of three parts, which are presented in Fig. 2.10 and it includes the recalculation of the Galactic gravitational potential. That procedure was performed when changing any of the model ingredients listed in Table 5.1 except atmosphere models and extinction model. When changing the parameters of the thick disc and scale length the changes in the derivation of the new mass model are negligible, thus we have not performed those calculations.

5.2 The impact of the model's inputs on the results

In this section we present the fitting and analysis for each of the model's ingredients separately. We have investigated the impact on the results when each of them was changed independently from the others. The undertaken discussion helped us to establish and justify the composition of our default model.

Depending on the model's ingredient different strategies have been followed in our studies. In some cases the fit of the synthetic and observed LF was checked and the whole sky simulations were performed. However most usually we were performing the simulations in three established regions and comparing the results with Tycho-2 data. When choosing those three regions we wanted to pick one at the plane, the second at intermediate latitudes and the third at the pole and ensure that in Tycho-2 set they do not show any extraordinary or problematic features. Those standards fields were chosen to be:

- region 1: the Galactic North Pole at $b=(70^\circ;90^\circ)$
- region 2: at intermediate latitudes $l=(160^\circ;180^\circ)$ and $b=(20^\circ;40^\circ)$
- region 3: within the plane $l=(70^\circ;90^\circ)$ and $b=(-10^\circ;10^\circ)$.

We have checked whether the region chosen at these intermediate latitudes is a representative sample of the entire stripe of the sky at intermediate latitudes, see $(B - V)_T$ distributions in Fig. 5.3 at the top. The same test was made for the region within the plane, its $(B - V)_T$ distribution was compared to the $(B - V)_T$ distribution of the entire plane of Tycho-2 data, see Fig. 5.3 bottom.

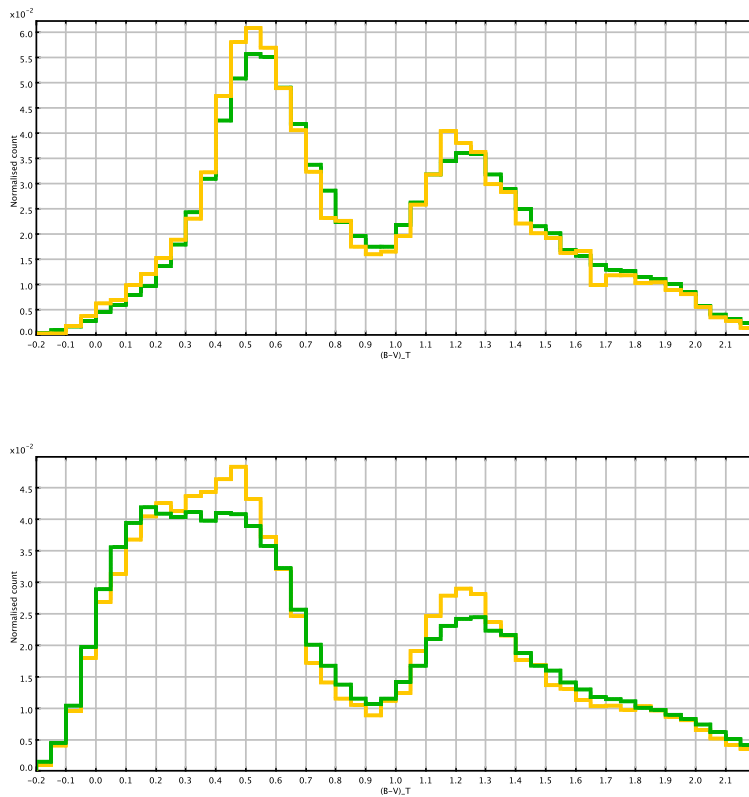


Figure 5.3: The two standard regions representing our Tycho-2 sample. Top: in green normalized $(B-V)_T$ distribution of the stripe of the sky at intermediate latitudes $b=(20^\circ;40^\circ)$ and in orange the region 2 chosen for analysis. Bottom: in green $(B-V)_T$ distribution of the entire plane of Tycho-2 data and in orange the region 3 chosen for analysis.

5.2.1 The local stellar mass density

We have investigated whether changing the assumption on the value of local stellar mass density causes significant changes in the star counts and $(B - V)_T$ distributions produced by our model. In Table 3.10 of section 3.7 we have presented two observational values assigned to that parameter, which have been tried in our research. The older one was derived in Wielen (1974) and we will refer to it as LMD1 (local mass density 1). The second value was provided in Jahreiß and Wielen (1997) after Hipparcos data was published and here we refer to it as LMD2 (local mass density 2). This value is in the agreement with the value given by Reid et al. (2002). We have varied just the density corresponding to main-sequence and giants stars keeping for white dwarfs $0.007 M_{\odot}/pc^3$ in both cases. The tested values are:

- LMD1 = $0.039 M_{\odot}/pc^3$
- LMD2 = $0.033 M_{\odot}/pc^3$.

Subsequently, we have applied the LMD1 and LMD2 to our default model A (with and without binarity), then the LMD1 and LMD2 to our default model where the IMF was changed to Kroupa (2008) and the SFR was set constant (with and without binarity) and also the LMD1 and LMD2 to our default model where the IMF was changed to Just and Jahreiß (2010) (with binarity). The synthetic luminosity functions were calculated for the ten presented cases and compared to the observed data, see Fig. 5.4, 5.5 and 5.6. The figures corresponding to all tested models can be found in Table 5.2.

As expected the effect of changing the value of local mass density from LMD1 to LMD2 is the same over all the length of the LF and it is that we decrease the number of objects. Binarity produces a second order effect. In Fig. 5.4 and 5.5 we can observe the behavior of the synthetic LF when binarity was added with respect to the LF obtained with the same model's ingredients but without binaries. The one with binarity compared to the one without binarity goes down (in number of objects) at the bright magnitudes and goes up at the faint magnitudes, while in the intermediate range both are very similar. This tendency is seen in both figures and in the case of two local density values. It is because when adding binarity we create secondaries, which will have a tendency to be low-mass stars. Thus when adding binarity we increment the number of objects at the low-mass tail of LF and decrement the high masses.

Before discussing how good is the fit of each presented synthetic LF we would like to point out to the reader that the three LF derived from observations differ one from another. Especially Jahreiß and Wielen (1997) and Reid et al. (2002) are very different in the bright domain. Taking into account big error bars at the bright and faint ends of the LF and also the fact that three observational set differ between them, one could conclude that all presented synthetic LF fit the observations. It can be noticed that in the bright domain our default model A (with both values of local mass density) fits better the Kroupa (2001) and Reid et al. (2002) data see Fig. 5.4, whereas our default model with Kroupa (2008) IMF instead of Haywood-Robin (and both values of local mass density) fits better to Jahreiß and Wielen (1997) data see Fig. 5.6. In the region of $4 < M_V < 8$ mag the default model A (with both values of local mass density) fits data much better than default model with Kroupa (2008) IMF. At the faint end ($M_V > 9$) the observed LF is highly uncertain in all cases.

In Fig. 5.6 one can notice that our default model with IMF changed to the one of Just and Jahreiß (2010) and LMD2 value fits very well the Jahreiß and Wielen (1997) data for $M_V < 8$

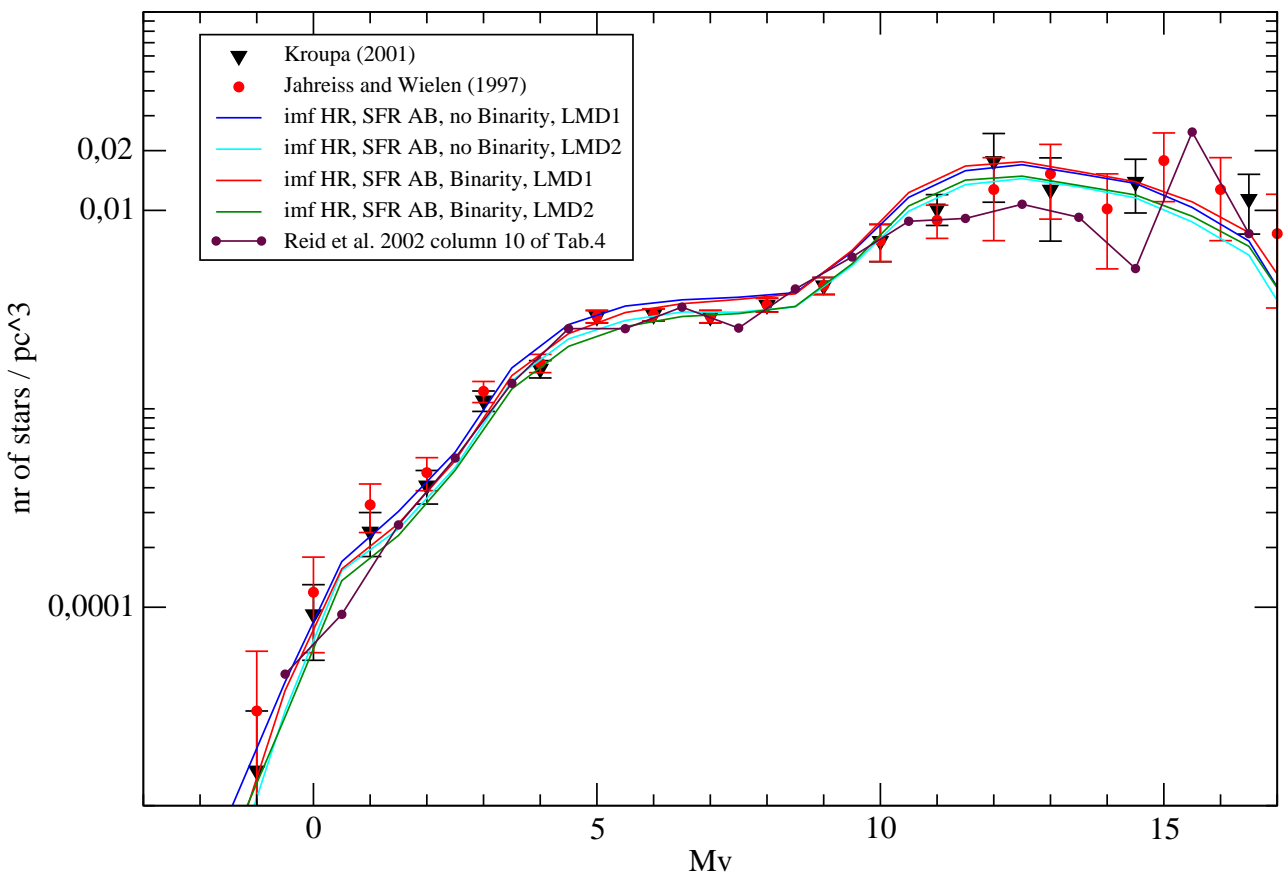


Figure 5.4: Comparing the observed local LF with the synthetic LF obtained with our default model A and two values of local stellar mass density, LMD1 and LMD2 (in both cases simulations with and without binarities).

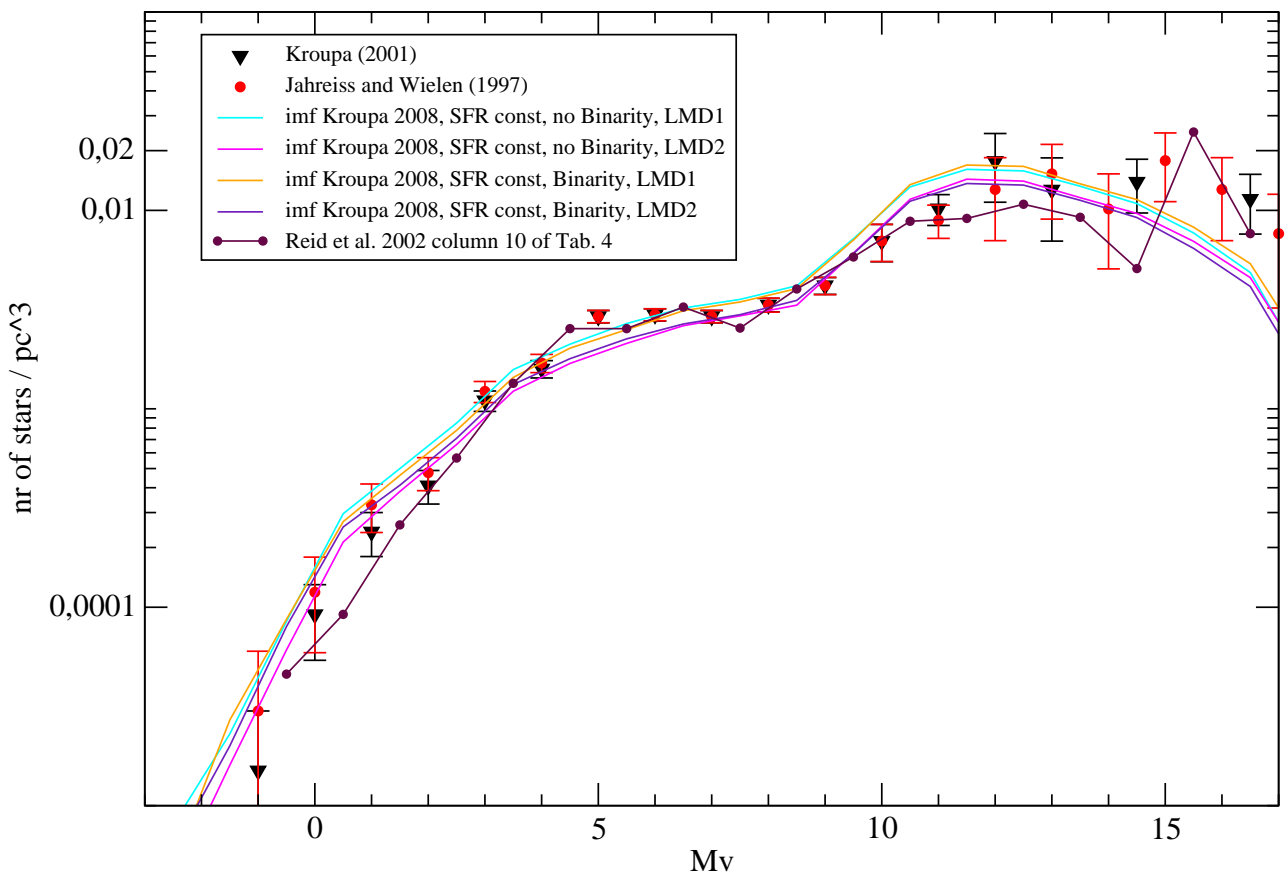


Figure 5.5: Comparing the observed LF with the synthetic LF obtained with our default model, where the IMF was changed to Kroupa (2008), the SFR was set constant and two values of local stellar mass density were used, LMD1 and LMD2, comparing in both cases simulations with and without binaries.

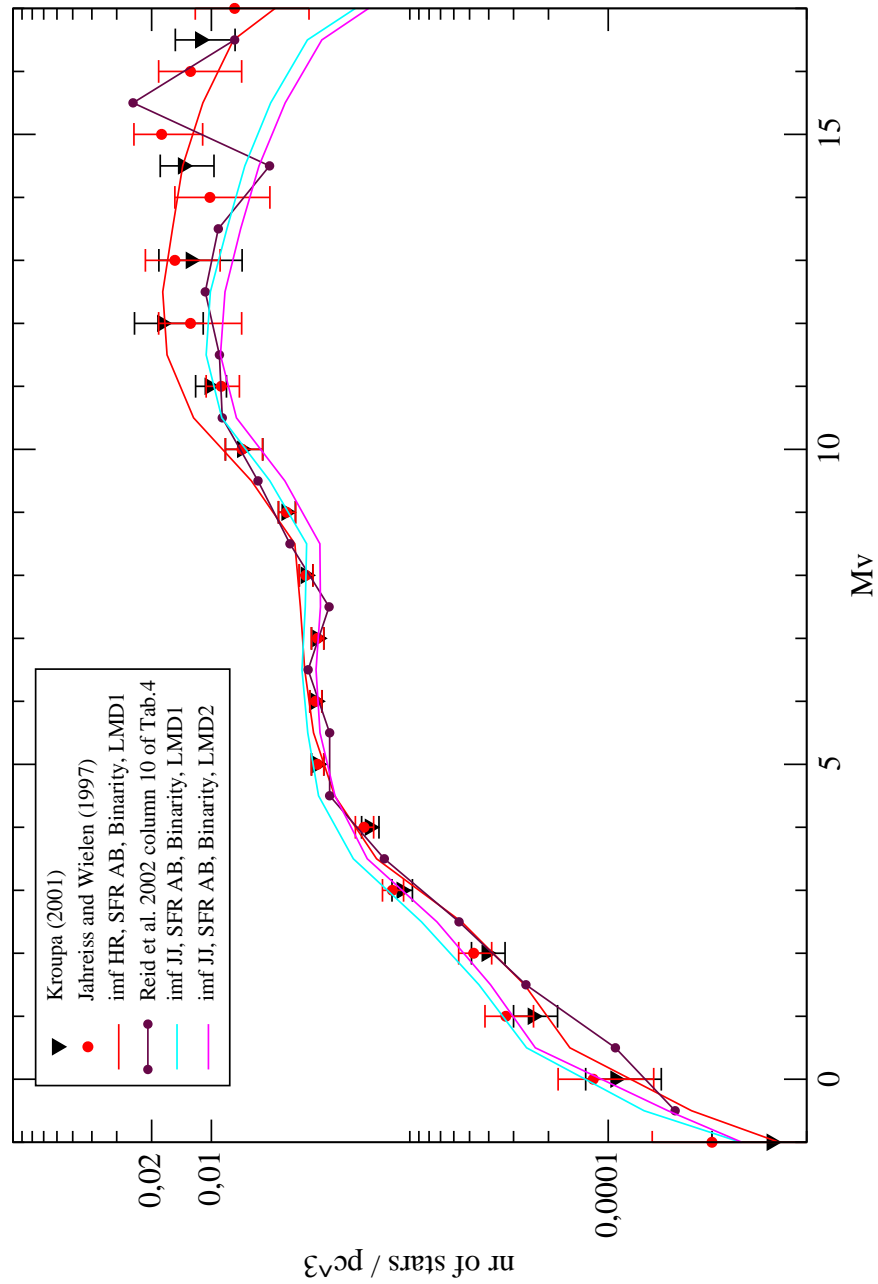


Figure 5.6: Comparing the observed LF with the synthetic LF obtained with our default model, where the IMF was changed to Just and Jahreiß (2010) IMF and two values of local stellar mass density were used, LMD1 and LMD2.

IMF + SFR	LMD	Binarity	Figures
Haywood-Robin IMF + Aumer and Binney (2009) SFR default model A	LMD1	yes	Fig. 5.4
Haywood-Robin IMF + Aumer and Binney (2009) SFR default model A	LMD1	no	Fig. 5.4
Haywood-Robin IMF + Aumer and Binney (2009) SFR default model A	LMD2	yes	Fig. 5.4
Haywood-Robin IMF + Aumer and Binney (2009) SFR default model A	LMD2	no	Fig. 5.4
Kroupa (2008) and constant SFR	LMD1	yes	Fig. 5.5
Kroupa (2008) and constant SFR	LMD1	no	Fig. 5.5
Kroupa (2008) and constant SFR	LMD2	yes	Fig. 5.5
Kroupa (2008) and constant SFR	LMD2	no	Fig. 5.5
Just and Jahreiß (2010) IMF + Aumer and Binney (2009) SFR	LMD1	yes	Fig. 5.6
Just and Jahreiß (2010) IMF + Aumer and Binney (2009) SFR	LMD2	yes	Fig. 5.6

Table 5.2: The table of figures where comparing of LF was showed for each model tested in this section.

mag. As will be discussed later on in this section this combination do not fit well the Tycho-2 $(B - V)_T$ distribution.

In Table 5.3 we present the contribution of the secondary stars to the total stellar mass density of the thin disc in case of our default model A with IMF changed to the one of Just and Jahreiß (2010). It also confirms the correctness of our treatment. We can see that the mass density corresponding to the synthetic LF from Fig. 5.4 and 5.6 is equal to LMD1 and LMD2 respectively.

In Table 5.4 we compare the number of objects in each M_V bin between Reid et al. (2002) data and our default model with two values of local mass density, LMD1 and LMD2.

We conclude that using only the observed LF was not sufficient to constrain the local mass density value, so we used the Tycho-2 data. Our Tycho-2 sample corresponds to the range in $M_V = (-1; 5)$ mag.

We have performed the whole sky simulations with our default model A and the two values LMD1 and LMD2 and as well for our default model where the IMF was changed to Just and Jahreiß (2010) and the local mass density was set to LMD2 (best fit according to LF). In Fig. 5.7 we present the cumulative whole sky $(B - V)_T$ distributions of the Tycho sample and three models we have tried.

source	default model	default model A	default model A	default model
	LMD1	LMD2	Just and Jahreiß (2010) IMF LMD1	Just and Jahreiß (2010) IMF LMD2
primary + single stars	0.033	0.028	0.033	0.028
secondary stars	0.006	0.005	0.006	0.005
total	0.039	0.033	0.039	0.033

Table 5.3: The local mass density (in M_{\odot}/pc^3) corresponding to the synthetic LF calculated with our default model A (and both values: LMD1 and LMD2) and our default model with Just and Jahreiß (2010) IMF (and both values: LMD1 and LMD2).

Mv bin	Reid et al. (2002)	default model A	default model A
		LMD1	LMD2
-0.5	0.46	0.38	0.28
0.5	0.92	1.56	1.36
1.5	2.60	2.64	2.30
2.5	5.65	5.48	4.90
3.5	13.45	14.7	12.59
4.5	25.36	23.92	20.65
5.5	25.36	30.54	25.95
6.5	32.54	33.87	29.18
7.5	25.52	35.61	30.19
8.5	40.16	37.97	32.81
9.5	58.26	62.81	53.73
10.5	88.16	122.87	105.26
11.5	91.06	167.33	142.09
12.5	107.30	175.84	148.84
13.5	92.31	156.94	133.49
14.5	50.93	139.53	119.55
15.5	248.28	110.33	93.43
16.5	76.39	77.39	65.90
17.5	76.39	29.48	25.09

Table 5.4: The comparison of the LF (units $10^{-4} * /pc^3$) in each M_V bin between Reid et al. (2002) data and our default model A with two values of local mass density, LMD1 and LMD2.

In Fig. 5.8 we show the same results, but the histograms are normalized to give the same number of objects. In Fig. 5.9 and 5.10 we present the $(B - V)_T$ histograms for the same models after dividing the sky into three parts according to the latitude (Galactic plane, intermediate latitudes and poles).

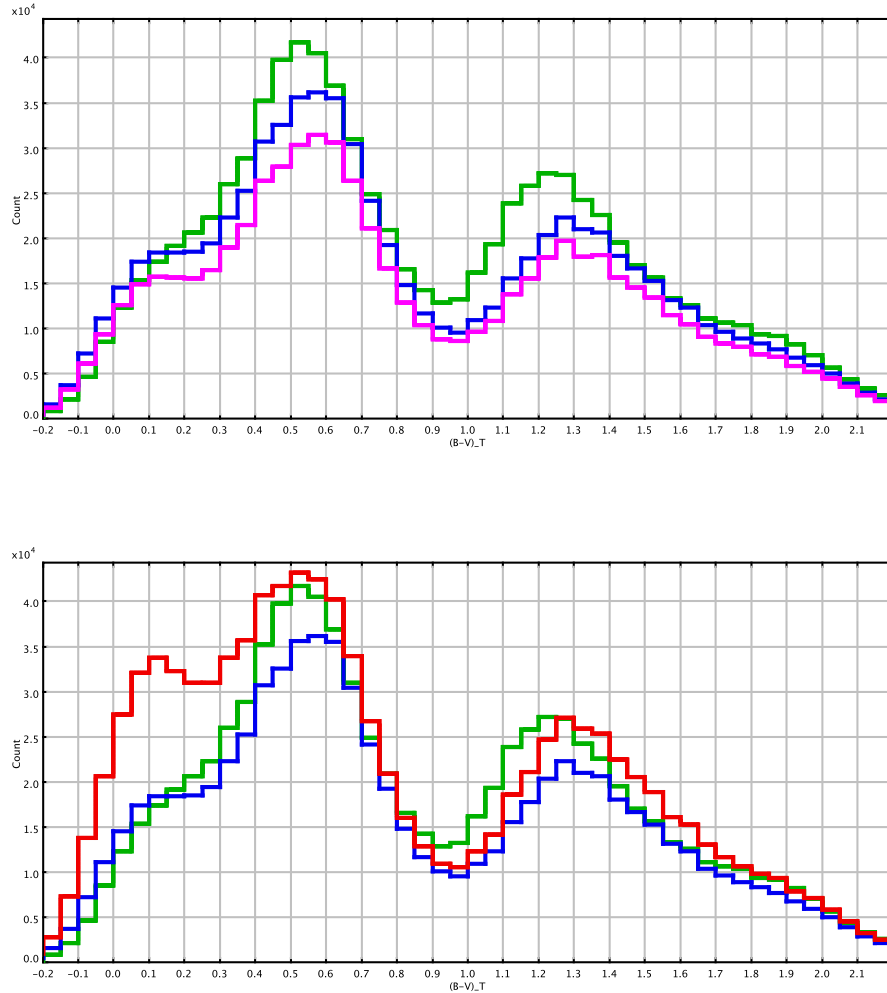


Figure 5.7: The cumulative whole sky $(B - V)_T$ distribution. In green Tycho-2 data, in blue the simulations with our default model A and LMD1, in pink our default model A with LMD2 and in red our default model with IMF changed to the one of Just and Jahreiß (2010) and LMD2.

Fig. 5.7 indicates that our default model with Just and Jahreiß (2010) IMF and LMD2 yields to an excess of very bright stars. From that we conclude that Tycho-2 data could constrain the LF at its bright end ($M_V < 4$).

We can see that the Just and Jahreiß (2010) IMF and LMD2 combination produces too many blue stars, hence it could be estimated that the Just and Jahreiß (2010) IMF with LMD1 would provide even less realistic solution when compared to Tycho-2 data. The fit provided by our default model A and LMD1 is in our opinion the best from all presented combinations, although it shows some discrepancies as well. We emphasize that at this point we do not discriminate any IMF, but we discuss different combinations of IMF and local mass density values. There are other important model's ingredients as for instance SFR, which have to be taken into consideration

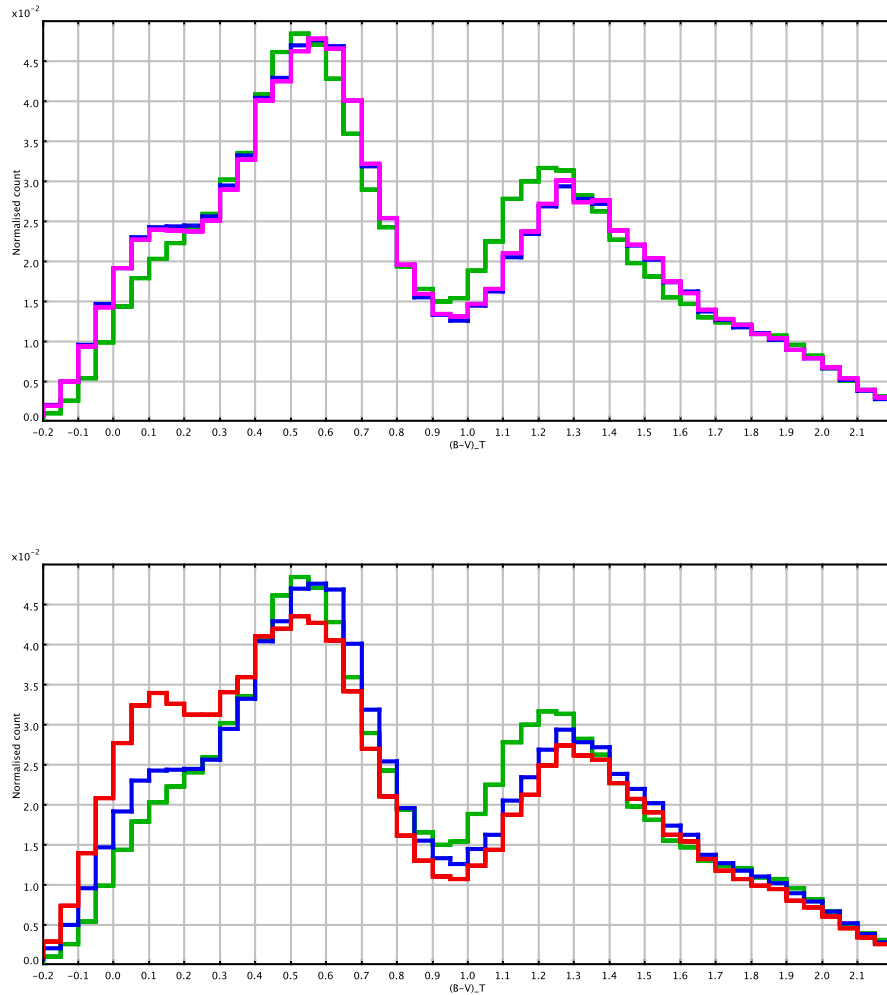


Figure 5.8: The normalized cumulative whole sky $(B - V)_T$ distribution. In green Tycho-2 data, in blue the simulations with our default model A and LMD1, in pink our default model A with LMD2 and in red our default model with IMF changed to the one of Just and Jahrei (2010) and LMD2.

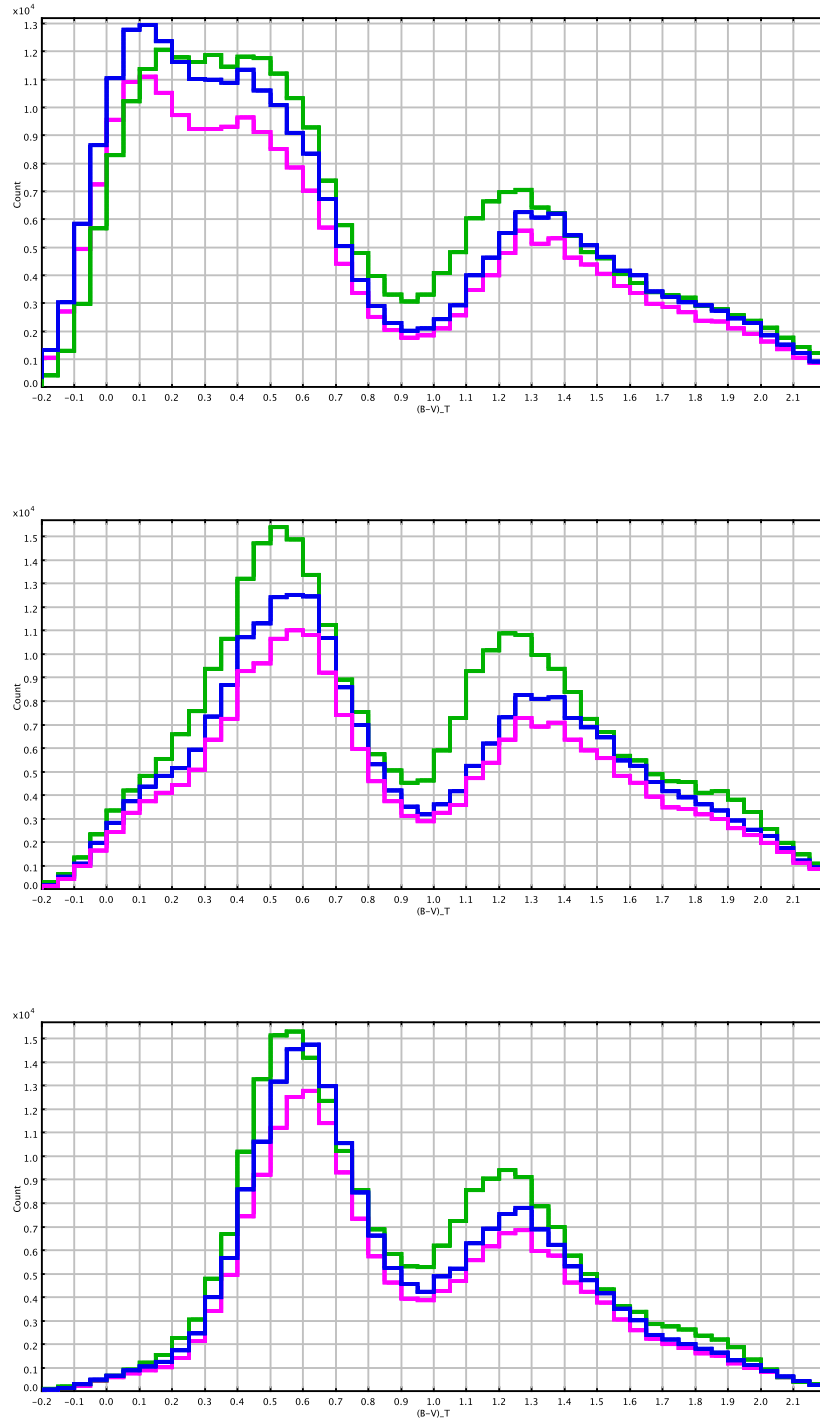


Figure 5.9: The $(B-V)_T$ distributions corresponding to top: entire Galactic plane $b=(-10^\circ;10^\circ)$, middle: entire stripes of sky at $b=(-30^\circ;-10^\circ)$ and $b=(10^\circ;30^\circ)$ and bottom: the stripes of sky at $b=(-90^\circ;-30^\circ)$ and $b=(30^\circ;90^\circ)$. In green Tycho-2 data, in blue the simulations with our default model A and LMD1 and in pink our default model A with LMD2.

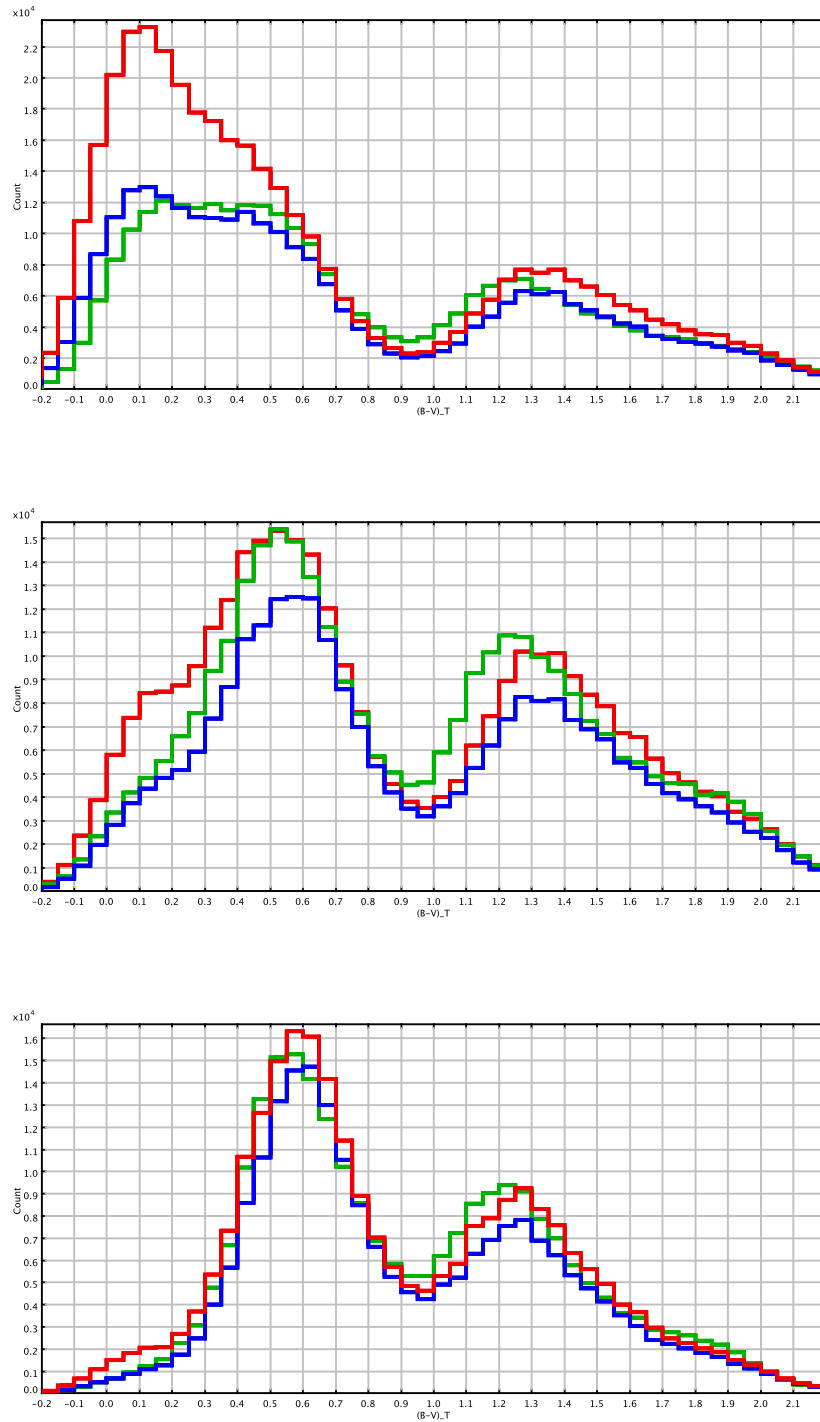


Figure 5.10: The $(B - V)_T$ distributions corresponding to top: entire Galactic plane $b = (-10^\circ; 10^\circ)$, middle: entire stripes of sky at $b = (-30^\circ; -10^\circ)$ and $b = (10^\circ; 30^\circ)$ and bottom: the stripes of sky at $b = (-90^\circ; -30^\circ)$ and $b = (30^\circ; 90^\circ)$. In green Tycho-2 data, in blue the simulations with our default model A and in red our default model with IMF changed to the one of Just and Jahrei (2010) and LMD2.

when choosing the best fit IMF. This work is presented in the following sections.

The total number of stars corresponding to presented whole sky simulations is:

- default model A + LMD1: 758372 (12 % less than Tycho sample)
- default model A + LMD2: 656320 (24 % less than Tycho sample)
- default model + Just and Jahreiß (2010) IMF + LMD2: 992858 (15 % more than Tycho sample)
- Tycho2: 864816,

thus in case of our default model A we miss stars. When we look at the normalized whole sky $(B - V)_T$ histograms in Fig. 5.8 we can notice that the shape of the distribution provided by our default model A fits Tycho-2 very well apart from the remaining shift in the giants peak, while Just and Jahreiß (2010) IMF produces a bump in the bluest stars. As it will be shown in section 5.2.2 this effect can not be solved by changing the SFR. From analysis done in this section we might suggest that in order to fit better the Tycho-2 with our default model A higher mass density should be assumed in the local neighborhood. However, as pointed out before, our whole sky Tycho-2 data allows us to fit only the bright region of the LF that is $M_V < 6$ mag. Depending only on this observational constraint we maintain the LMD1 as our default value and we exclude the LMD2 value. In order to choose properly between the two values, LMD1 and LMD2 one would need to try more data sets especially a catalogue complete up to $V \sim 18$ mag, such as Gaia will provide.

From Fig. 5.9 and 5.10 it is clear that Just and Jahreiß (2010) IMF gives significantly worst fit in the plane than Haywood-Robin IMF and only slightly better at intermediate latitudes, when the same decreasing SFR is assumed. This trend is clearly reproduced in Fig. 5.10 (top: Galactic plane). We are aware that reproducing the Galactic plane is a hard task. It is possible that the differences in simulations obtained with different IMF would change if another extinction maps or spiral arms models would be used.

5.2.2 The IMF and the SFR

Here we present the results of the simulations when different scenarios were assumed for IMF and SFR. The rest of the model's inputs was set as in our default model presented in Table 5.1. In Table 5.5 we give a list of figures corresponding to each IMF and SFR combination.

IMF	constant SFR	decreasing SFR: $\exp(0.12 \times \tau)$ Aumer and Binney (2009)
Haywood et al. (1997a)	Fig. A.2, A.4, A.6, A.8	Fig. 5.11, 5.12, 5.13, 5.15
Haywood-Robin	Fig. A.1, A.3, A.5, A.7	Fig. 5.11, 5.12, 5.13, 5.14
Vallenari et al. (2006)	Fig. A.2, A.4, A.6, A.8	Fig. 5.11, 5.12, 5.13, 5.15
Kroupa (2008)	Fig. A.1, A.3, A.5, A.7	Fig. B.1, B.2, B.3 Fig. 5.11, 5.12, 5.13, 5.14
Just and Jahreiß (2010)*	Fig. A.1, A.3, A.5, A.7	Fig. 5.11, 5.12, 5.13, 5.14
Kroupa-Haywood v.1		Fig. B.1, B.2, B.3, B.4
Kroupa-Haywood v.4		Fig. B.1, B.2, B.3, B.4
Kroupa-Haywood v.6	Fig. A.2, A.4, A.6, A.8	Fig. B.1, B.2, B.3, B.4 Fig. 5.11, 5.12, 5.13, 5.14
Kroupa-Haywood v.7		Fig. B.1, B.2, B.3, B.4
Kroupa-Haywood v.8		Fig. B.1, B.2, B.3, B.4

Table 5.5: The list of figures corresponding to each IMF and SFR combination. *Additionally, the IMF of Just and Jahreiß (2010) was combined with the SFR of the model A from Just and Jahreiß (2010) (see Fig. 5.16).

The constant SFR was tested along with all ten IMF proposed in section 3.1. In Appendix A we show the results of simulations done with the six more representative IMF and a constant SFR. Following our strategy we have compared there the $(B - V)_T$ distributions towards the three established regions for all the cases and also we have checked the fitting of the produced synthetic luminosity functions to the observed ones. From Fig. A.1, A.2, A.3, A.4, A.5 and A.6 we derive several conclusions:

1. There is almost no difference in number of objects and the appearance of $(B - V)_T$ histograms at the high Galactic latitudes (Galactic North Pole) between simulations done with decreasing (Aumer and Binney (2009)) and constant SFR.
2. At intermediate latitudes the differences are still small.
3. In the plane we observe clearly that the constant SFR produces much more blue on average young objects than a decreasing SFR.

We conclude that when imposing a constant SFR along with ten IMF that we have tried we are always getting unrealistic star counts on the blue part of our $(B - V)_T$ distribution within the Galactic plane when comparing to Tycho-2 data. All above conclusions are coherent with the results from the fitting of the local LF (see Fig. A.7 and A.8). A constant SFR produces too many bright objects no matter which IMF have been used.

In Appendix B we present the results of comparisons between Kroupa (2008) IMF and the five tested versions of Kroupa-Haywood IMF (see section 3.1), when combined with the decreasing

SFR of Aumer and Binney (2009). Our reasoning was to compare the performances of those IMF between them, then to choose the one which performs best when comparing to Tycho-2 data and compare it with the five IMF from literature. Looking at the $(B - V)_T$ distributions in Fig. B.1, B.2 and B.3 we draw the following conclusions:

- Kroupa-Haywood v1 and Kroupa-Haywood v4 IMF give a very bad fit to Tycho-2 data at intermediate latitudes and within the plane.
- We notice that Kroupa-Haywood v6 and Kroupa-Haywood v7 give very similar results and those results are in agreement with Tycho-2 data in all three regions. In the first case we have changed the values of two slopes and in the second we have moved one mass limit with respect to the Kroupa-Haywood v1 (see section 3.1).
- Kroupa-Haywood v8 produces too many stars at the Galactic pole and within the plane when combined with a decreasing SFR of Aumer and Binney (2009).

Then we have calculated the synthetic LF for each investigated model and we compared them to the observed LF (see Fig. B.4). The range of the LF which corresponds to our Tycho-2 sample is $M_V = (-1; 5)$ mag. It is interesting to notice that in the range $M_V = (0; 4)$ mag the synthetic LF produced by Kroupa-Haywood v1 and Kroupa-Haywood v4 IMF fit quite well the observed LF from Reid et al. (2002) and above the $M_V = 4$ mag they drop below the observational points. At the same time we have seen from comparisons with Tycho-2 data that those two IMF give very poor fit especially within the Galactic plane. Then, we observe that Kroupa-Haywood v6 and Kroupa-Haywood v7 in the absolute magnitude range corresponding to Tycho-2 sample produce very similar LF and those solutions fall in between the observational points of Jahreiß and Wielen (1997) and Kroupa (2001). The comparisons with Tycho-2 sample show that those two IMF provide good fits, however when we look at the fit of the local LF at the full domain of M_V we see that Kroupa-Haywood v6 IMF gives a more realistic results than the Kroupa-Haywood v7. The latter one in the $M_V = (5; 8)$ mag produces too many stars. The LF calculated from simulations with the Kroupa-Haywood v8 IMF in the bright domain is in agreement with Jahreiß and Wielen (1997) data. We know from Tycho-2 constraints that this IMF provides too many stars.

We conclude that the Kroupa-Haywood v6 IMF when combined with decreasing SFR from Aumer and Binney (2009) reproduces best the Tycho-2 data from the six IMF presented in Appendix B. As it will be discussed later on we propose that our Tycho-2 sample can help to constrain the observed LF.

Subsequently we have compared the simulations obtained with Kroupa-Haywood v6 IMF and the five IMF from literature, again when a decreasing SFR from Aumer and Binney (2009) was assumed. In Fig. 5.11, 5.12 and 5.13 we present the $(B - V)_T$ distributions produced towards our three regions by all mentioned combinations of IMF and SFR. We observe that

- when we used the Kroupa (2008) IMF we lack stars at intermediate latitudes, while in the plane an unnatural bump of the bluest stars is created.
- Just and Jahreiß (2010) IMF at the pole leads to slightly too many stars, at intermediate latitude provides a very good fit, however within the plane the fit is bad. Similarly to the case of Kroupa (2008) IMF there are too many blue and bright objects.

- Vallenari et al. (2006) IMF when combined with the decreasing SFR of Aumer and Binney (2009) produces far too many stars when compared to Tycho-2 data in the plane and almost acceptable results at intermediate and high latitudes.
- Haywood et al. (1997a) IMF is not bad at the pole but it provides a poor fit at intermediate latitudes and within the plane.
- Haywood-Robin and Kroupa-Haywood v6 IMF combined with the decreasing SFR of Aumer and Binney (2009) lead to good fit at the high and intermediate latitudes. When looking at the Galactic plane we can notice that those are the two IMF that provide best results when compared to Tycho-2 data. There are still some discrepancies present, however the Galactic plane is where many different factors interplay and finding a good fit is a very complex task (see next sections in this chapter).

In Fig. 5.14 and 5.15 we show the fitting of synthetic LF obtained with the six discussed IMF and a decreasing SFR from Aumer and Binney (2009) to the observed LF. We see that the LF produced by Vallenari et al. (2006) and Just and Jahreiß (2010) IMF in the bright domain are close to the observed LF of Jahreiß and Wielen (1997) and between 4 and 9 mag are above all observational points. That suggests that these two combinations of IMF and SFR are not fitting well the local LF. Kroupa (2008) and Haywood et al. (1997a) IMF give a better overall fit to the observed LF, but those functions when combined with a decreasing SFR led to a poor fit to Tycho-2 $(B - V)_T$ distributions.

Constraining the bright stars of our simulations just by the LF is hard, because as can be seen the error bar is large there. Tycho-2 serves as a stronger constraint in that range.

We have performed additional simulations combining the IMF of Just and Jahreiß (2010) with the SFR of the model A (best fit) from Just and Jahreiß (2010) (see section 3.2). As usually the simulations were done towards our three chosen regions. In Fig. 5.16 we compare their results with the ones obtained with Just and Jahreiß (2010) IMF and Aumer and Binney (2009) decreasing SFR. One can notice that both SFR give very similar solutions. We conclude the Just and Jahreiß (2010) IMF used with two different decreasing SFR (including the SFR of the best fit model from Just and Jahreiß (2010)) is not able to reproduce the Tycho-2 $(B - V)_T$ distribution of the Galactic plane when applied to our new model.

Finally in Fig. 5.17 we show the whole sky cumulative $(B - V)_T$ distribution obtained with our default model, a decreasing SFR from Aumer and Binney (2009), and our two best fit IMF, the Haywood-Robin and Kroupa-Haywood v6 compared to Tycho-2 data. In Fig. 5.18 the same simulations but divided into three latitude ranges. It can be seen that Haywood-Robin IMF fits better the blue peak of Tycho $(B - V)_T$ distribution, whereas Kroupa-Haywood v6 performs better in the red peak. In this section we have demonstrated that the simulations obtained with those two IMF (and a decreasing SFR) fit Tycho-2 data best. For that they have been applied in our two default models presented in Table 5.1. When evaluating the fit between Tycho-2 data and our new default models A and B presented in Fig. 5.17 it is crucial to contemplate our departure point, which was the same comparison made three years earlier using the old model, see Fig. 5.1 top. The change is enormous.

In this section 5.2.2 we have seen that one of our major discrepancies when comparing to Tycho-2 data is the excess of the blue stars within the Galactic plane. It is present in the colour distributions produced by all investigated IMF and SFR combinations and in most cases that

excess is very significant. In the following sections we will demonstrate that it can be caused by a superposition of various effects.

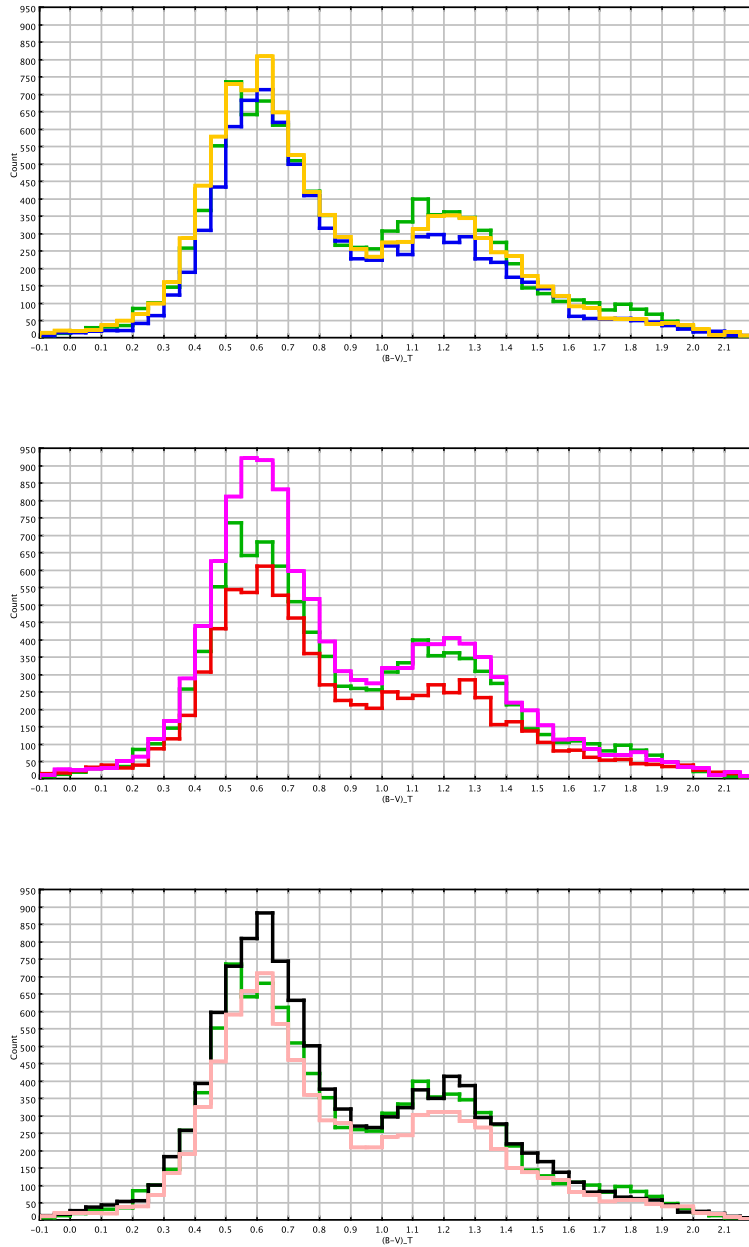


Figure 5.11: $(B - V)_T$ distribution towards the Galactic North Pole. In green Tycho-2 data, in blue the simulations with Haywood-Robin IMF, in orange Kroupa-Haywood v6, in red simulations with Kroupa (2008) IMF, in magenta Just and Jahrei (2010) IMF, in black Vallenari et al. (2006) IMF and in pink Haywood et al. (1997a) IMF. In all models we have imposed a decreasing exponential SFR of Aumer and Binney (2009).

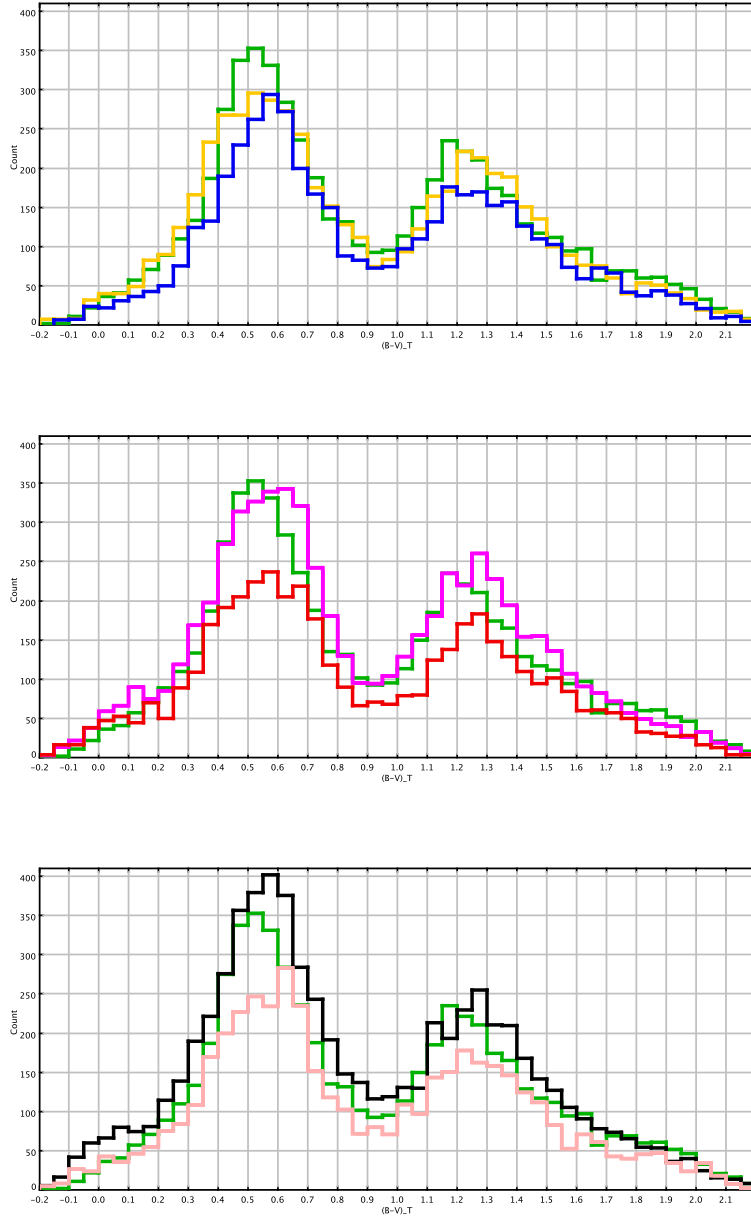


Figure 5.12: $(B - V)_T$ distribution of the region 2 corresponding to the intermediate latitudes. In green Tycho-2 data, in blue the simulations with Haywood-Robin IMF, in orange Kroupa-Haywood v6, in red simulations with Kroupa (2008) IMF, in magenta Just and Jahreiß (2010) IMF, in black Vallenari et al. (2006) IMF and in pink Haywood et al. (1997a) IMF. In all models we have imposed a decreasing exponential SFR of Aumer and Binney (2009).

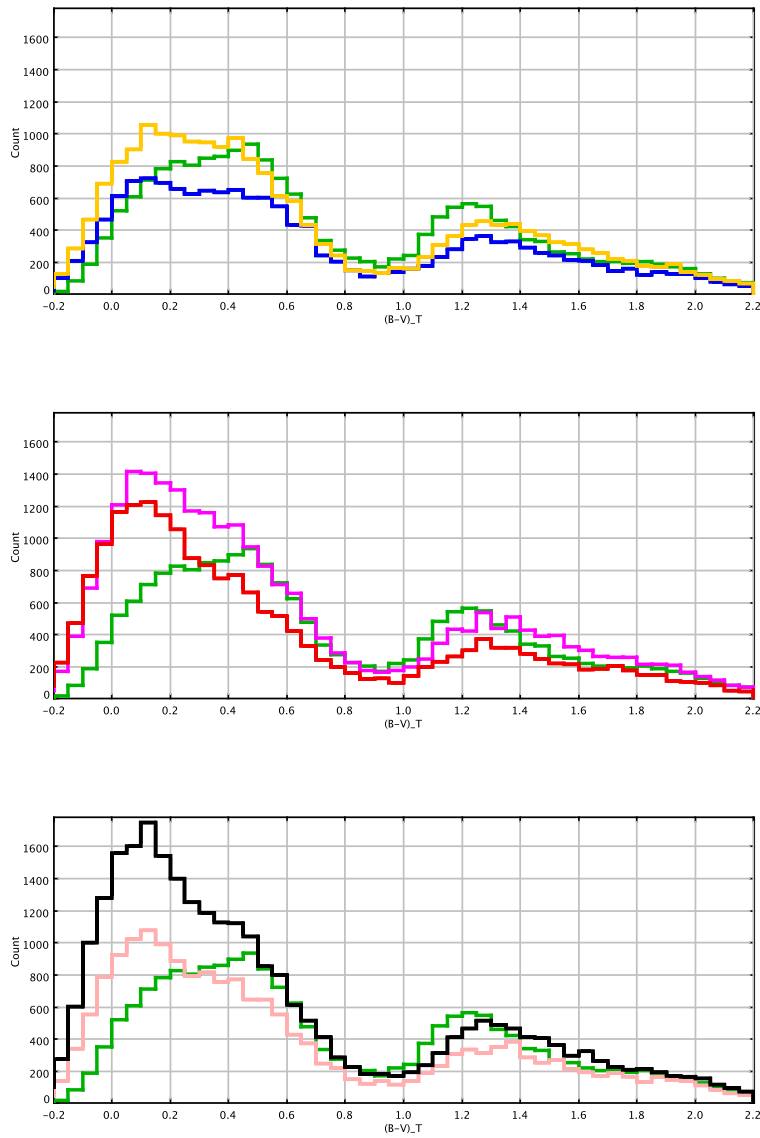


Figure 5.13: $(B-V)_T$ distribution of region 3 within the plane. In green Tycho-2 data, in blue the simulations with Haywood-Robin IMF, in orange Kroupa-Haywood v6, in red simulations with Kroupa (2008) IMF, in magenta Just and Jahreiß (2010) IMF, in black Vallenari et al. (2006) IMF and in pink Haywood et al. (1997a) IMF. In all models we have imposed a decreasing exponential SFR of Aumer and Binney (2009).

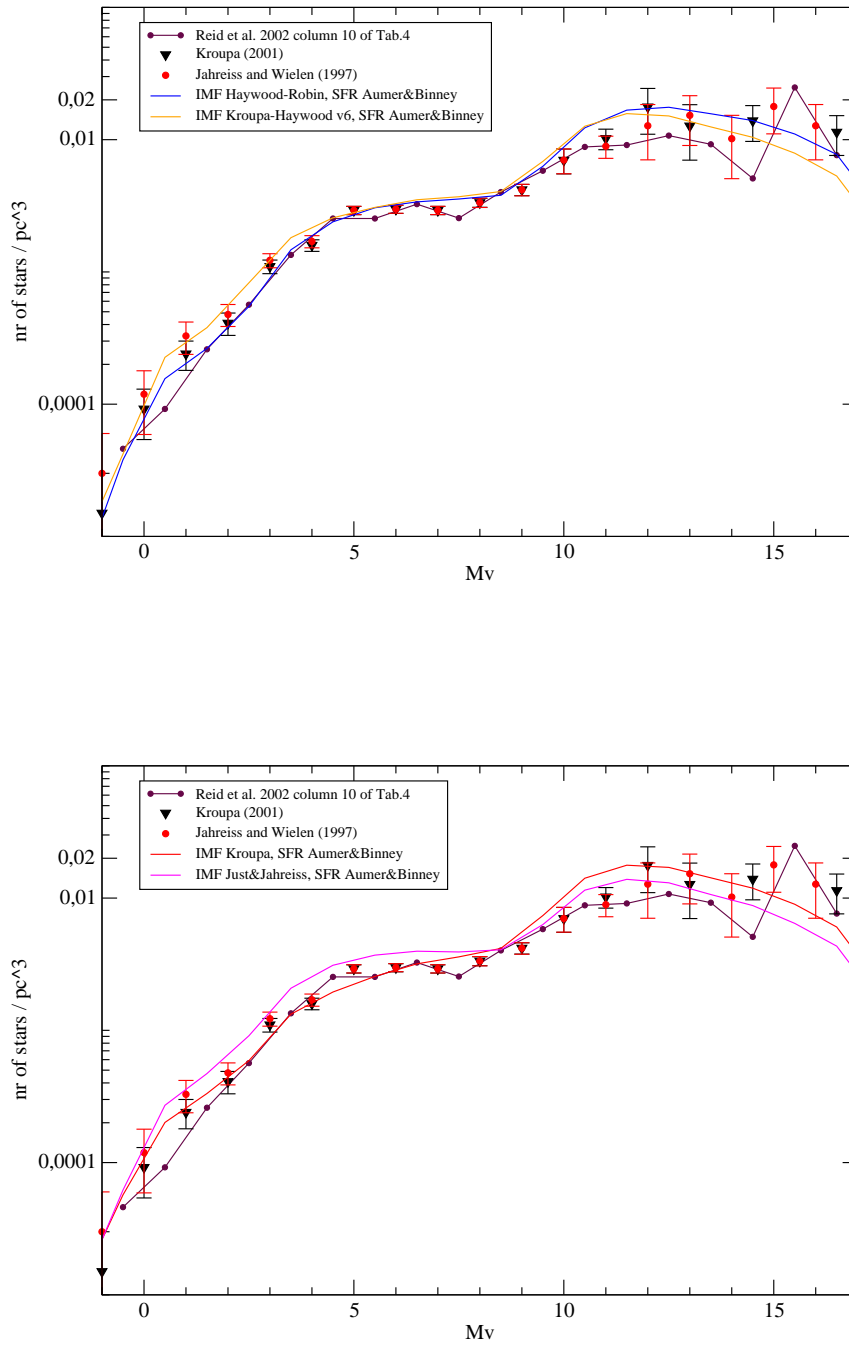


Figure 5.14: Comparing the observed LF with the synthetic LF obtained with our default model where a decreasing exponential SFR of Aumer and Binney (2009) was applied together with different IMF.

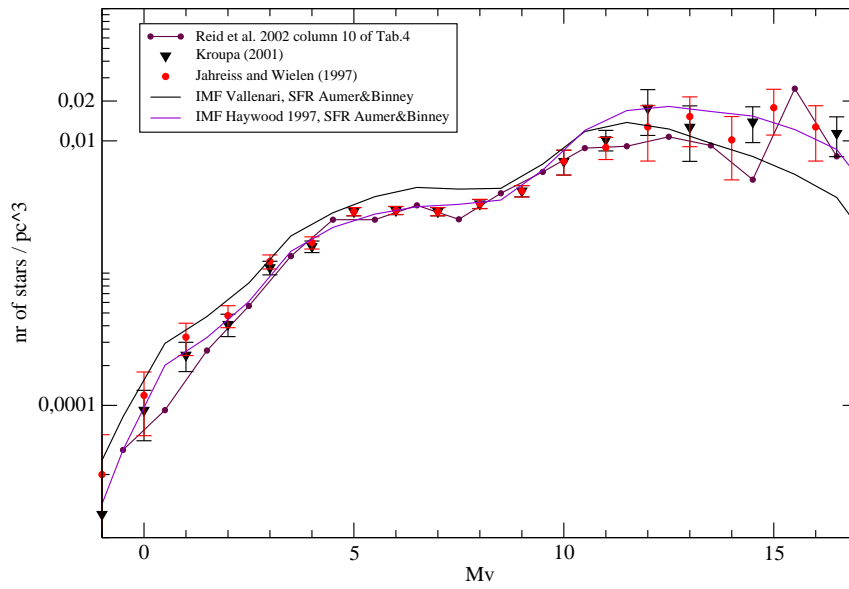


Figure 5.15: Comparing the observed LF with the synthetic LF obtained with our default model where a decreasing exponential SFR of Aumer and Binney (2009) was applied together with different IMF.

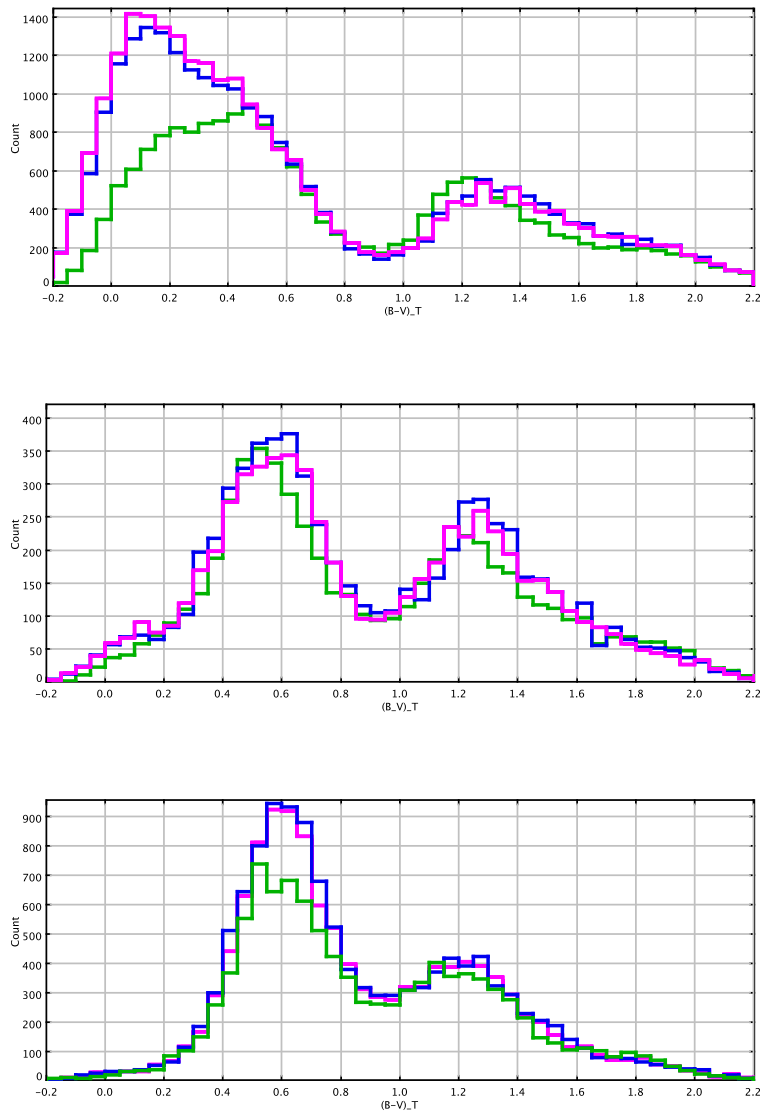


Figure 5.16: $(B - V)_T$ distributions towards our three established regions: at the top Galactic plane, in the middle intermediate latitudes and at the bottom the Galactic North Pole obtained with Just and Jahreiß (2010) IMF and two different SFR: in magenta the decreasing exponential SFR of Aumer and Binney (2009) and in blue the SFR of the model A from Just and Jahreiß (2010). In green Tycho-2 data.

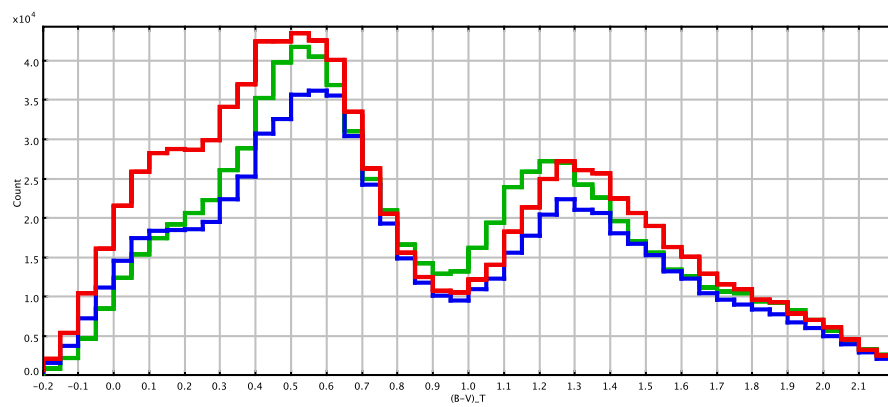


Figure 5.17: The cumulative whole sky $(B - V)_T$ distribution. In green Tycho-2 data, in blue the simulations with our default model A (Haywood-Robin IMF) and in red our default model B (Kroupa-Haywood v6 IMF).

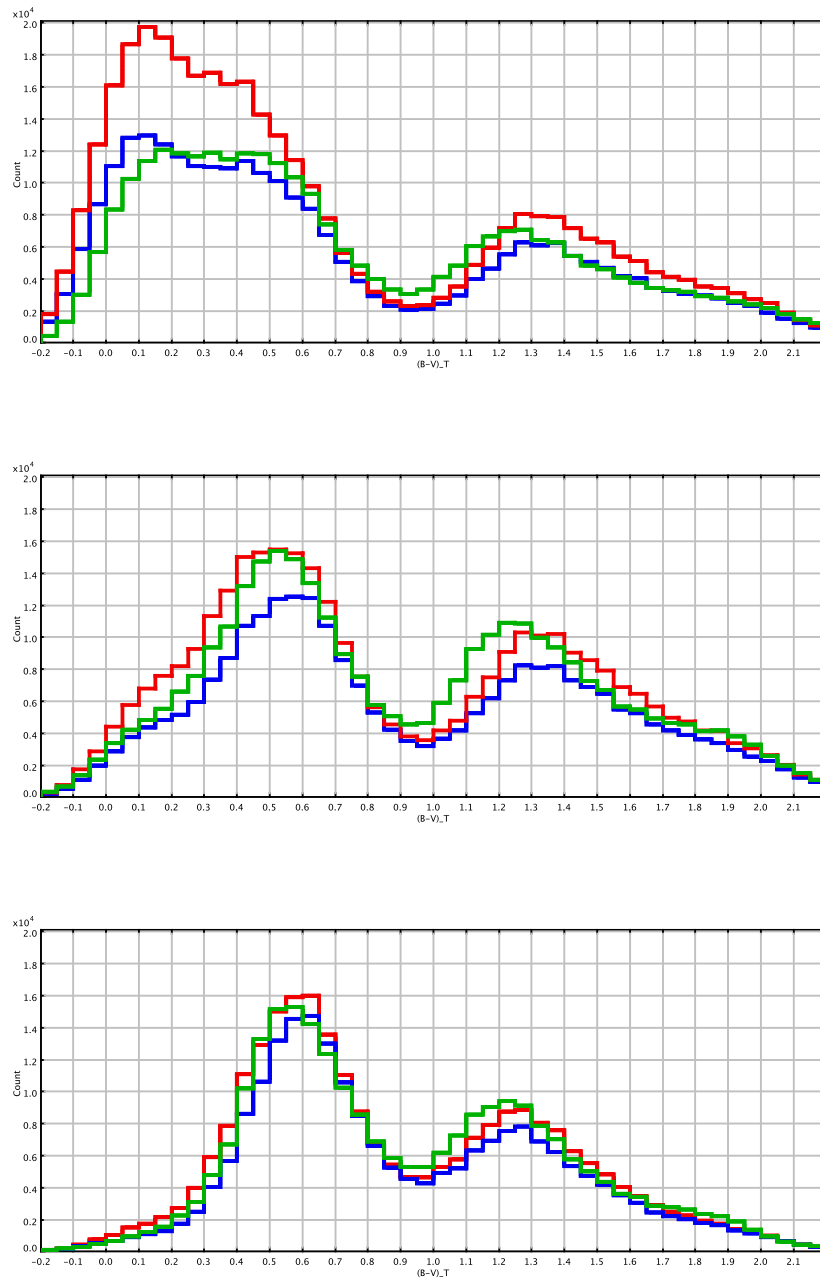


Figure 5.18: The $(B - V)_T$ distributions corresponding to top: entire Galactic plane $b=(-10^\circ;10^\circ)$, middle: entire stripe of sky at $b=(-30^\circ;-10^\circ)$ and $b=(10^\circ;30^\circ)$ and bottom: the stripe of sky at $b=(-90^\circ;-30^\circ)$ and $b=(30^\circ;90^\circ)$. In green Tycho-2 data, in blue the simulations with our default model A (Haywood-Robin IMF) and in red our default model B (Kroupa-Haywood v6 IMF).

5.2.3 Binariness

In Fig. 5.19 we show the comparison of $(B - V)_T$ distributions towards our three chosen regions performed with our default model B with and without binarity.

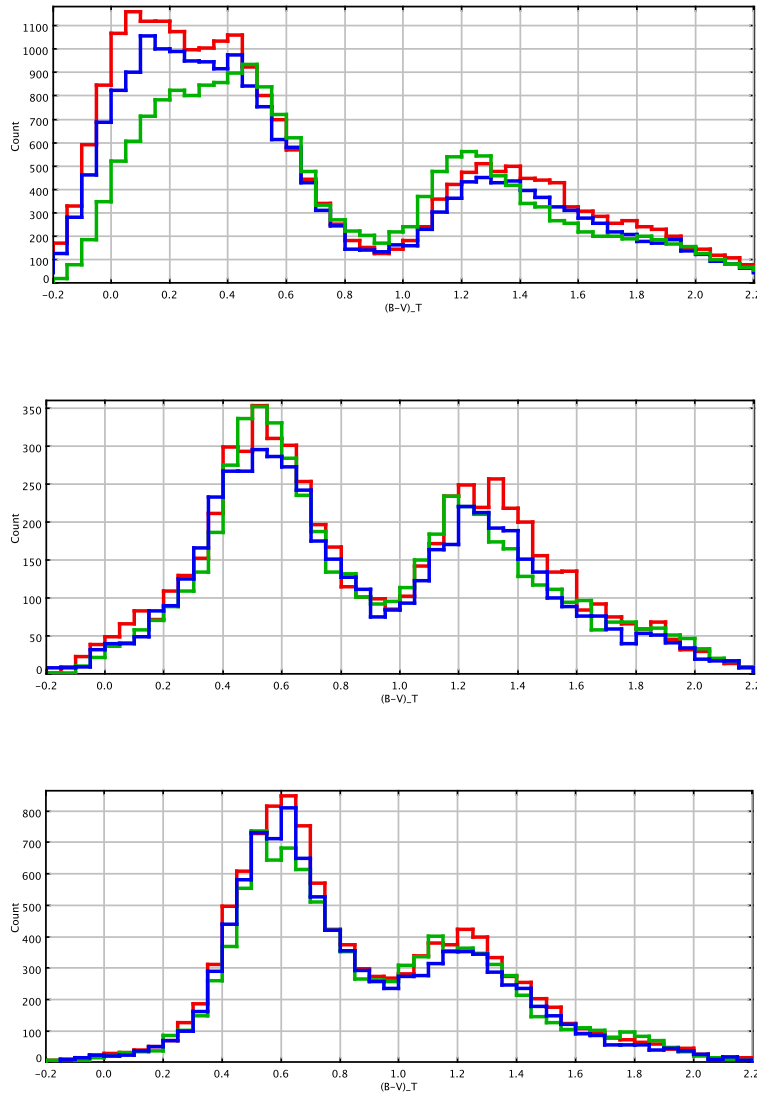


Figure 5.19: $(B - V)_T$ distributions towards our three established regions: at the top Galactic plane, in the middle intermediate latitudes and at the bottom the Galactic North Pole. In green Tycho-2 data, in blue the simulations with our default model B and binarity, in red simulations with our default model B and without binarity.

As can be clearly noticed in Fig. 5.19 simulations without binaries perform worse within the plane. In that case the excess of the blue stars is bigger than when binaries are produced. Additionally, the lack of binaries shifts the red peak of the colour distribution towards higher values, providing a worse fit to Tycho-2 data.

In order to compare our simulations with Tycho-2 data we have applied the value of 0.8 arc sec for the spatial resolution of our catalogue, meaning that all the binary systems generated below that limiting angular separation were merged. Apart from that value we have also tried the 0.5 and 1.0 arc sec and no significant changes could be noticed in the colour histograms when different separation values were applied. This is because most of the simulated binaries turn out to have much smaller separations.

We want to emphasize that introducing binarity is a great advantage of our new model and that now binaries are produced by default.

5.2.4 The age of the thin disc

We have investigated if the change in the age of the thin disc can substantially change the colour distribution of the sample. Firstly we have extended its value to 12 Gyr. Then we have decreased it to 9 Gyr following del Peloso et al. (2005). Using both values we have performed the simulations with our default model B towards the three established regions. We remind to the reader that in our default model this parameter is set to 10 Gyr. In Fig. 5.20 we present the resulting comparisons between both simulations and Tycho-2 data.

At the Galactic pole the three simulated samples perform similarly in the blue peak, while in the red peak we may see that the solution obtained with 12 Gyr old thin disc produces a bit more of old stars and it fits better Tycho-2 data. At intermediate latitudes we also see some more giants generated in simulations with 12 Gyr old thin disc, but here it is more than in Tycho sample. In this range the best solution is provided by simulations with 9 Gyr old thin disc, however the 10 Gyr old thin disc performs good as well. Finally in the plane all samples agree in the red peak while in the blue peak we can notice clear differences. It seems that if we extend the age of the thin disc to 12 Gyr we produce a bit less of the blue and young stars within the plane, what makes the fit to Tycho-2 data better. However, as we already have discussed several times the Galactic plane is a problematic region, where extinction, spiral arms and many other effects play important roles. This is why it is not straightforward to constrain any parameter there. We keep the investigation of the age of the thin disc open. Samples containing fainter stars should be used in the future. We decided to keep the value of 10 Gyr as the thin disc in our default model.

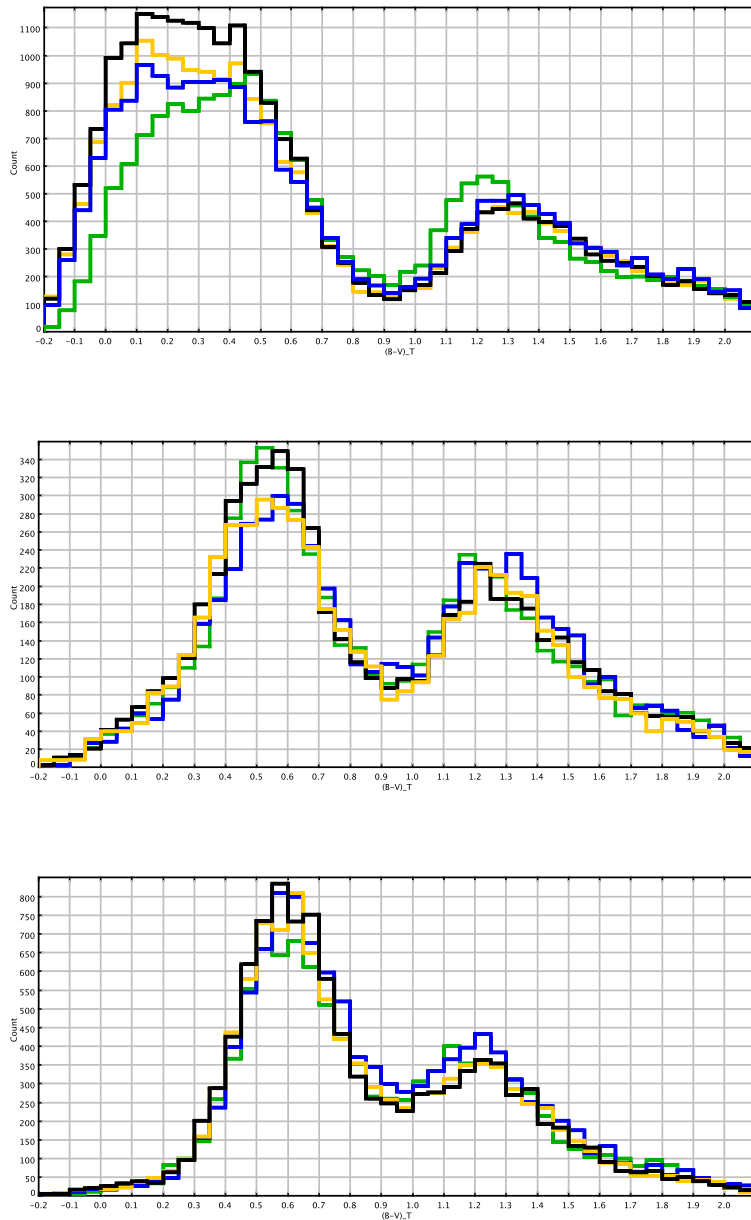


Figure 5.20: $(B - V)_T$ distributions towards our three established regions: at the top Galactic plane, in the middle intermediate latitudes and at the bottom the Galactic North Pole. In green Tycho-2 data, in blue the simulations with our default model B and the age of the thin disc extended to 12 Gyr, in orange our default model B and the age of the thin disc set to 10 Gyr and in black our default model B and 9 Gyr old thin disc.

5.2.5 The thick disc

Our simulated and data samples are magnitude limited. That results in a fact that we are mainly working with the thin disc stars. The thick disc was found to have a small contribution to our star counts, whereas halo contribution is negligible. We have decided to investigate the importance of the thick disc population in our analysis and in this section we present a short discussion on that subject.

The Eq. 1 of Reylé and Robin (2001) expresses the density law used for the thick disc in BGM. This law is assumed to be a truncated exponential, meaning that at large distances it is exponential and at short distances it is a parabola. The authors discuss there the three parameters defining the density of that population along the z axis:

- h_z the scale height
- the local density
- and x_l the distance above the plane where the density law becomes exponential.

In our analysis with Tycho-2 sample we have tried two different sets of the values describing the density law for the thick disc. We wanted to check if this can significantly change the contribution of thick disc to our sample and if consequently it can change the appearance of the $(B - V)_T$ distributions.

We define the first thick disc density model by the set of values:

- $h_z = 800$ pc
- density normalization factor = 1.0 leading to the local density of the thick disc = 0.0029 M_\odot/pc^3 or 0.0083 in $*/\text{pc}^3$
- $x_l = 400$ pc.

The second density model was defined by the values:

- h_z 1200.0 pc
- density normalization factor = 0.25 (four times less than the first model assumes)
- $x_l = 72.0$ pc.

For both cases we have simulated two of our standard regions, the Galactic North Pole and the one at intermediate latitudes and compared the results with Tycho-2 data. One can clearly see that the first model assuming more density for the thick disc provides us better fit to Tycho-2 $(B - V)_T$ distributions. It fits better the red giants peak and significantly contributes at intermediate colours in between the peaks.

We have also performed the whole sky statistics and it turned out that the contribution of the thick disc to the total number of stars in our sample in the case of two density models is the following:

- first density model: 7.3 %

- second density model: 2 %.

We have decided to use the first density model, which is assuming more density for the thick disc as it reproduces better the Tycho-2 $(B - V)_T$ distributions.

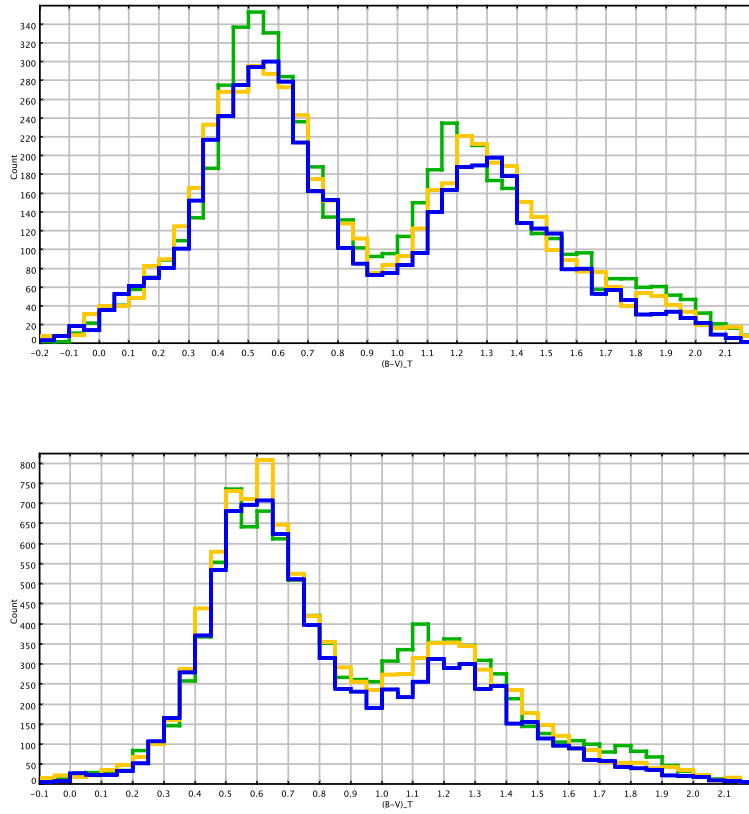


Figure 5.21: $(B - V)_T$ distributions towards our two established regions: at the top intermediate latitudes and at the bottom the Galactic North Pole. In green Tycho-2 data, in blue the simulations with our default model B and the second thick disc density model and in orange our default model B and the first thick disc density model.

5.2.6 Extinction model

The Marshall et al. (2006) extinction model applied in BGM covers a part of the thin disc corresponding to $l=(-100^\circ;100^\circ)$ and $b=(-10^\circ;10^\circ)$. In our default new model we use it for that stripe and the Drimmel and Spergel (2001) extinction model for the rest of the sky.

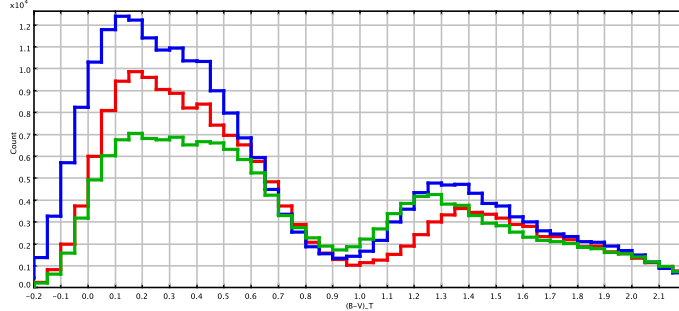
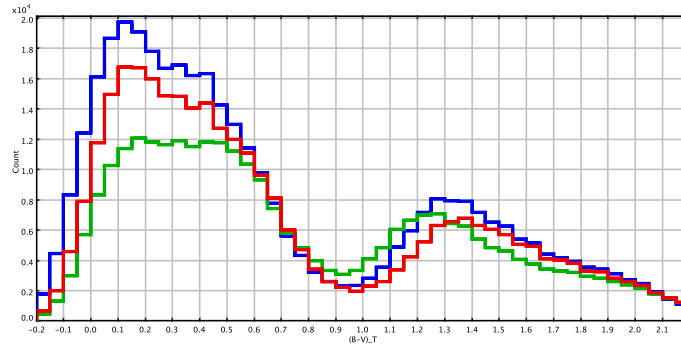


Figure 5.22: The comparison of $(B-V)_T$ distributions of a part of Galactic plane ($l=(-100^\circ;100^\circ)$ and $b=(-10^\circ;10^\circ)$) where our default model B was used along with two different extinction models: in red Drimmel and Spergel (2001) and in blue Marshall et al. (2006), in green Tycho data.

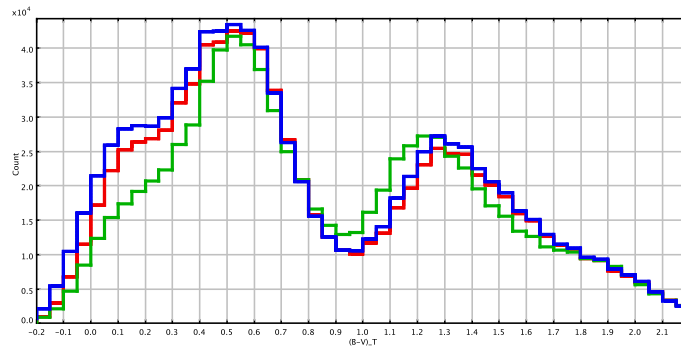
We were interested in comparing both approaches to extinction modelling, so we have simulated the $l=(-100^\circ;100^\circ)$ and $b=(-10^\circ;10^\circ)$ stripe in plane using the Drimmel and Spergel (2001) model as well, see Fig. 5.22. In all presented simulations our default model B was used. The blue histogram corresponds to Marshall et al. (2006) model, in red Drimmel and Spergel (2001) and in green Tycho data. The difference is significant. We have combined the stripes obtained with both extinction models with the simulations of the rest of the plane and the rest of the sky, which were done using only Drimmel and Spergel (2001) extinction law, in order to see how important are the differences in the global scale, see Fig. 5.23. As we can see those differences remain significant when looking at the whole plane and the entire sky. They can reach $\sim 10\%$ of star counts for the bluest and bright objects ($(B-V)_T < 0.4$). However, we want to emphasize that in presented here studies we have used our default model B. As can be noticed in the Fig. 5.18 from section 5.2.2 our default model A with different IMF does not show the excess of the blue stars, although the same Marshall et al. (2006) extinction model was used. It means that several parameters interplays within the plane and one should carefully derive conclusions about them.

In our work we decide to keep the combination of Marshall et al. (2006) model for $l=(-100^\circ;100^\circ)$ and $b=(-10^\circ;10^\circ)$ stripe and Drimmel and Spergel (2001) extinction law for the rest of the sky, assuming that Marshall et al. (2006) model has solved the saturation problems at the crowded Galactic center reported by Drimmel and Spergel (2001). However we conclude that the extinction model proposed by Marshall et al. (2006) probably underestimates the absorption in the local sphere covered by our Tycho-2 data. As can be seen in our analysis the extinction model is a crucial input of BGM and has a strong impact on the star counts and colour distributions of fields within the plane. It is possible that Marshall et al. (2006) extinction model underestimates the extinction at the very short distances, because he was not using main sequence stars. That

would explain why we see there much more of the blue stars than in the sample done with Drimmel and Spergel (2001) model and in data.



a) Galactic plane



b) whole sky

Figure 5.23: We have simulated the stripe $l=(-100^\circ;100^\circ)$ and $b=(-10^\circ;10^\circ)$ using two different extinction models: Drimmel and Spergel (2001) (in red) and Marshall et al. (2006) (in blue) and our default model B. We then joined it with the simulations of the rest of plane (a) and rest of sky (b) where Drimmel and Spergel (2001) extinction law was assumed and compared between them and with Tycho data (green).

5.2.7 Atmosphere models

We have compared the performance of three approaches to atmosphere models in our research, the BaSeL 2.2 and BaSeL 3.1 libraries and a combination of BaSeL 3.1 and MARCS solution for giants. In Fig. 5.24 we show the results of simulations towards our three established regions done with the default model B and BaSeL 2.2 (red) and BaSeL 3.1 (blue) libraries.

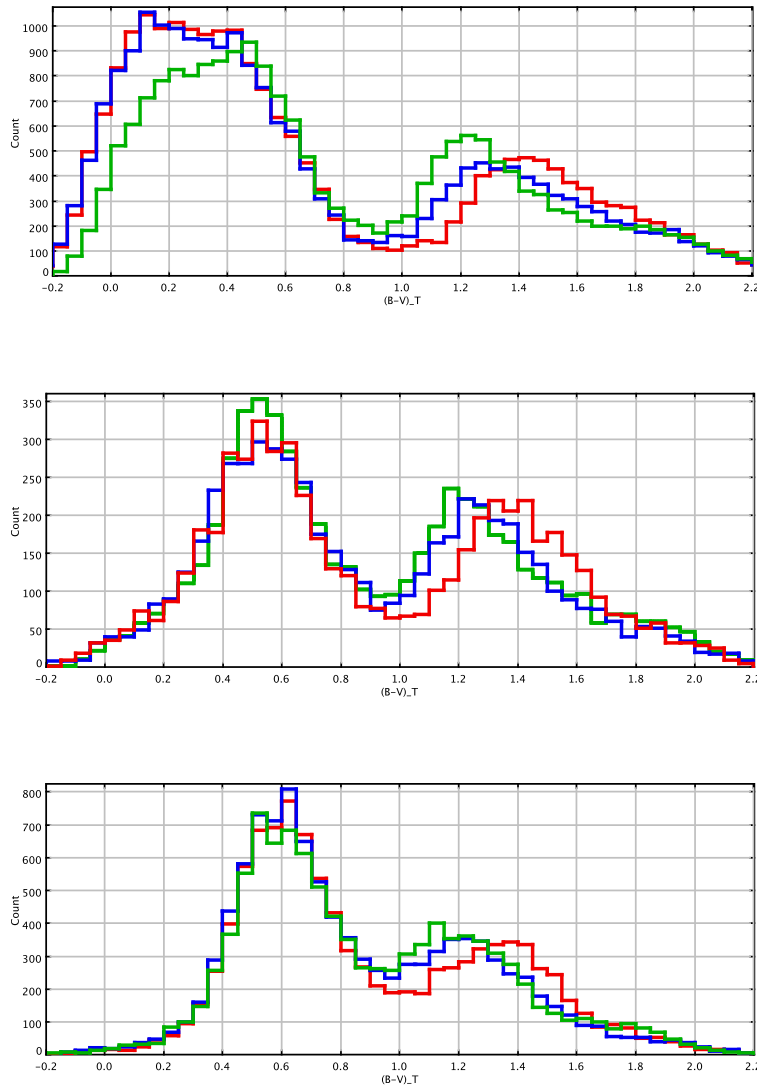


Figure 5.24: $(B - V)_T$ distributions towards our three established regions: at the top Galactic plane, in the middle intermediate latitudes and at the bottom the Galactic North Pole. In green Tycho-2 data, simulations done with our default model B and in red BaSeL 2.2 library and in blue BaSeL 3.1.

Similarly in Fig. 5.25 we compare the $(B - V)_T$ distributions for the same three regions obtained with our default model B and BaSeL 3.1 (blue) library and a combination of BaSeL

3.1 with MARCS grid (magenta).

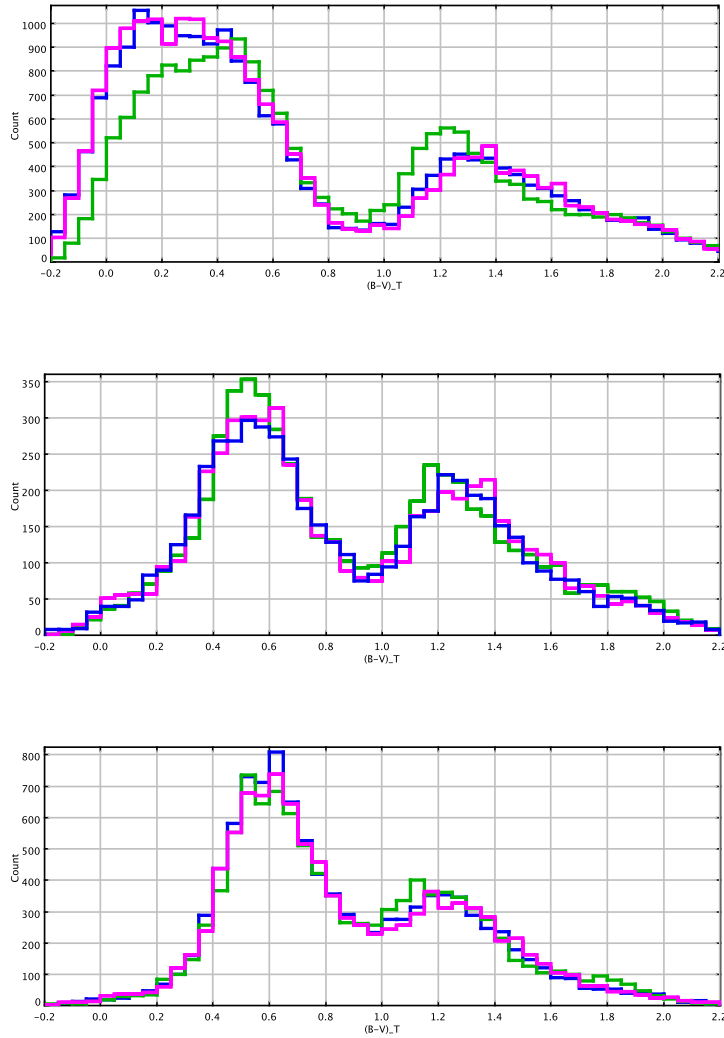


Figure 5.25: $(B - V)_T$ distributions towards our three established regions: at the top Galactic plane, in the middle intermediate latitudes and at the bottom the Galactic North Pole. In green Tycho-2 data, simulations done with our default model B and in blue BaSeL 3.1 and in magenta BaSeL 3.1 with MARCS grid (for giants).

BaSeL 2.2 library gives too red colours for giants when compared to Tycho-2 as expected, at all Galactic latitudes. BaSeL 3.1 library moves the red peak by about 0.1 mag towards bluer colours making it more similar to Tycho-2 giants. The MARCS solution for giants falls in between the two BaSeL libraries. It is clear that BaSeL 3.1 fits Tycho-2 data much better than the remaining two options, so we conclude that updating the atmosphere models to BaSeL 3.1 we have corrected the position of the K giants in the new model by 0.1 mag. This is an important improvement of our new BGM model (see in 5.1 top the significant shift of the red peak in the old BGM model).

5.2.8 Evolutionary tracks

In this section we present how the $(B - V)_T$ distributions have changed when changing the evolutionary tracks in the model from package B, which is our default to package A (consult the Table 3.3). It must be clarified that we have updated the evolutionary tracks of the new model firstly to the set A and then to the set B, which was the newest release and here we show the comparison between them. While in the old BGM model the evolutionary tracks frozen within the corresponding Hess diagram where even older as indicated in Table 3.3.

The differences in the colour distributions are minor. However, we decide to use the new tracks from Bertelli et al. (2008) and Bertelli et al. (2009), our package B, in our default model.

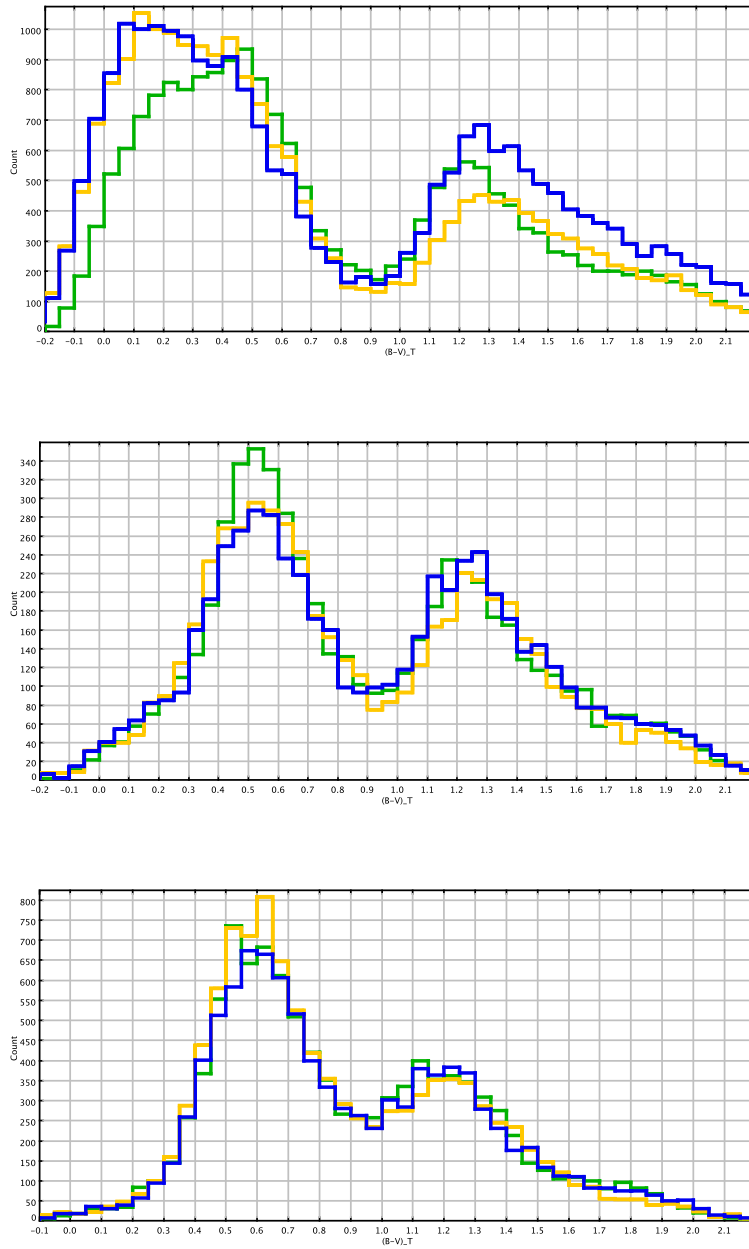


Figure 5.26: $(B - V)_T$ distributions towards our three established regions: at the top Galactic plane, in the middle intermediate latitudes and at the bottom the Galactic North Pole. In green Tycho-2 data, in blue the simulations with our default model B and package A of evolutionary tracks and in orange our default model B and package B of evolutionary tracks.

5.2.9 Age-metallicity relation

In section 3.6 we discussed the change of the age-metallicity relation. In the old model the Twarog (1980) values were used and in our new model we have updated them to the values proposed by Haywood (2006). Here we show the comparison of $(B - V)_T$ distributions towards our three established regions, when both relations were tried.

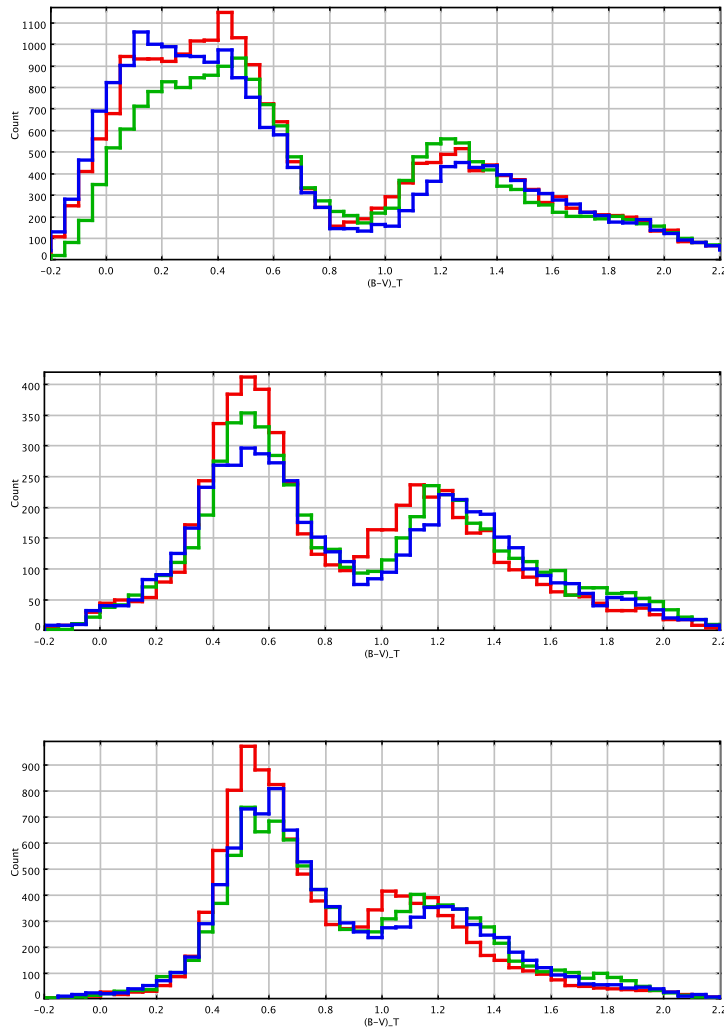


Figure 5.27: $(B - V)_T$ distributions towards our three established regions: at the top Galactic plane, in the middle intermediate latitudes and at the bottom the Galactic North Pole. In green Tycho-2 data, in red the simulations with old Twarog (1980) relation and in blue with the new values from Haywood (2006).

This parameter plays a lot on the position of the giant peak. As expected, the most significant differences are observed at intermediate and high Galactic latitudes. The new Haywood (2006) relation reproduces better both, the blue and the red peak of the colour distribution.

Thus looking at our results we choose it for our default model. However, it is possible that an intermediate age-metallicity relation could fit data even better, in case if Haywood (2006) correction was a bit too much.

5.2.10 The total local dynamical mass

In the old model the value of total local dynamical mass was the same as derived by Cr ez e et al. (1998). More recently van Leeuwen (2007) has applied a new reduction to Hipparcos data and recalculated that value, finding it about 20 per cent higher. If we would assume that the latter results are correct we would be seriously underestimating the total dynamical mass in our model. The consequence that follows from underestimation of the dynamical mass is that the calculated values of eccentricities $\epsilon(i)$ are too big. When they are too big the model should produce more stars at higher latitudes than are observed. We found it very interesting to check how the change of total local dynamical mass can affect the star counts and $(B - V)_T$ distributions of our samples. As we have described in section 3.7 we have tried the two mentioned values of the local dynamical mass in our new model. The potential was recalculated and the density normalization was performed. In Table 5.6 we present the values of $\epsilon(i)$, $RSVd(i)$, $\rho_{\odot}^{all}(i)$ and $\Sigma_{\odot}^{all}(i)$ which were obtained in both cases. We remind that the variables $RSVd(i)$ correspond to the ratio of surface to volume density and are part of the density normalization process. They are conceptually equal to scale heights, however we should not name them like this because we are using the Einasto density law and not the simple exponential law. While $\rho_{\odot}^{all}(i)$ is the local volume mass density and $\Sigma_{\odot}^{all}(i)$ local surface mass density for each age bin. We recommend to consult section 2.2.2 for more detailed explanation of those variables.

component	Cr�ez�e et al. (1998) ISM: $0.02 M_{\odot}/pc^3$				van Leeuwen (2007) ISM: $0.05 M_{\odot}/pc^3$			
	$\epsilon(i)$	$RSVd(i)$	$\rho_{\odot}^{all}(i)$	$\Sigma_{\odot}^{all}(i)$	$\epsilon(i)$	$RSVd(i)$	$\rho_{\odot}^{all}(i)$	$\Sigma_{\odot}^{all}(i)$
1	0.0140	129.90	0.0020	0.2604	0.0140	129.90	0.0018	0.2396
2	0.0225	277.21	0.0056	1.5666	0.0203	250.76	0.0057	1.4419
3	0.0319	390.78	0.0053	2.0595	0.0290	355.68	0.0053	1.8955
4	0.0478	583.71	0.0040	2.3220	0.0437	533.91	0.0040	2.1372
5	0.0610	744.17	0.0075	5.5600	0.0561	684.59	0.0075	5.1174
6	0.0692	843.89	0.0084	7.0681	0.0637	777.01	0.0084	6.5054
7	0.0697	849.97	0.0168	14.311	0.0642	783.09	0.0168	13.172
			0.0496	33.147			0.0495	30.509

Table 5.6: The changes in values of ϵ , $RSVd(i)$, $\rho_{\odot}^{all}(i)$ and $\Sigma_{\odot}^{all}(i)$ values when new van Leeuwen (2007) total dynamical density value was applied in our default model.

One can notice that after changing the total local mass density by increasing the density of the ISM the total volume mass density of stars remained the same, while the total surface mass density changed by the factor of 8 per cent. The volume mass density is obtained from simulations of the stellar content in the sphere around the Sun. In the sphere mode we assume just one big volume element with the density as at the position of the Sun. The mass density within the sphere did not change and we do not notice differences coming from the change of eccentricities $\epsilon(i)$. When calculating the surface mass density we integrate the density in the cylinder, thus here the change in values of eccentricities $\epsilon(i)$ plays a role and we notice the difference in resulting values.

From Fig. 5.28 we can conclude that the change of the dynamical mass has a weak impact on the Luminosity Function. As expected it provokes the change in the number of objects with the latitude, but in case of our magnitude limited simulations those differences are not big,

see Fig. 5.29. Nevertheless, it seems that van Leeuwen (2007) total dynamical mass leads to slightly better results at the Galactic pole. In our default model we have decided to keep the van Leeuwen (2007) value for the total dynamical mass.

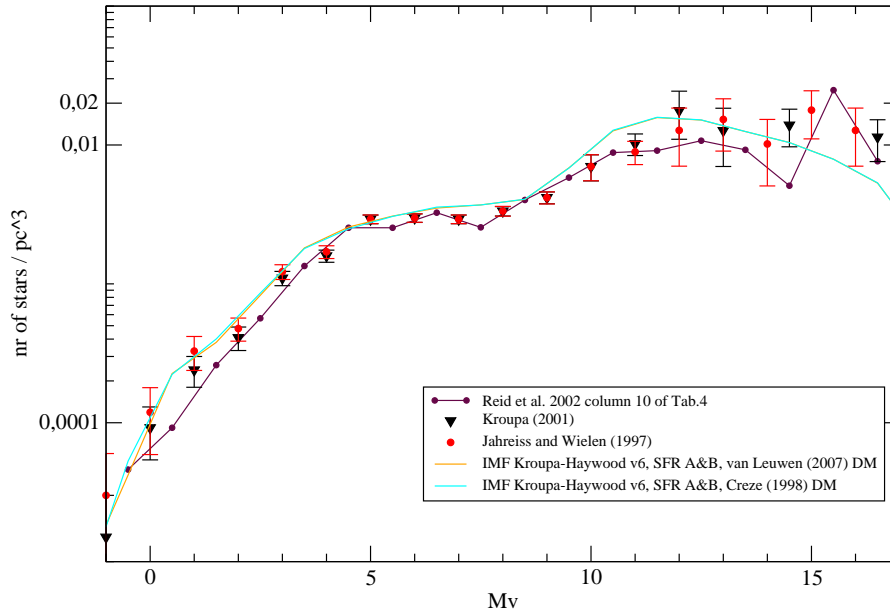


Figure 5.28: The comparison of the synthetic and the observed LF when two different values of the total dynamical mass were assumed.

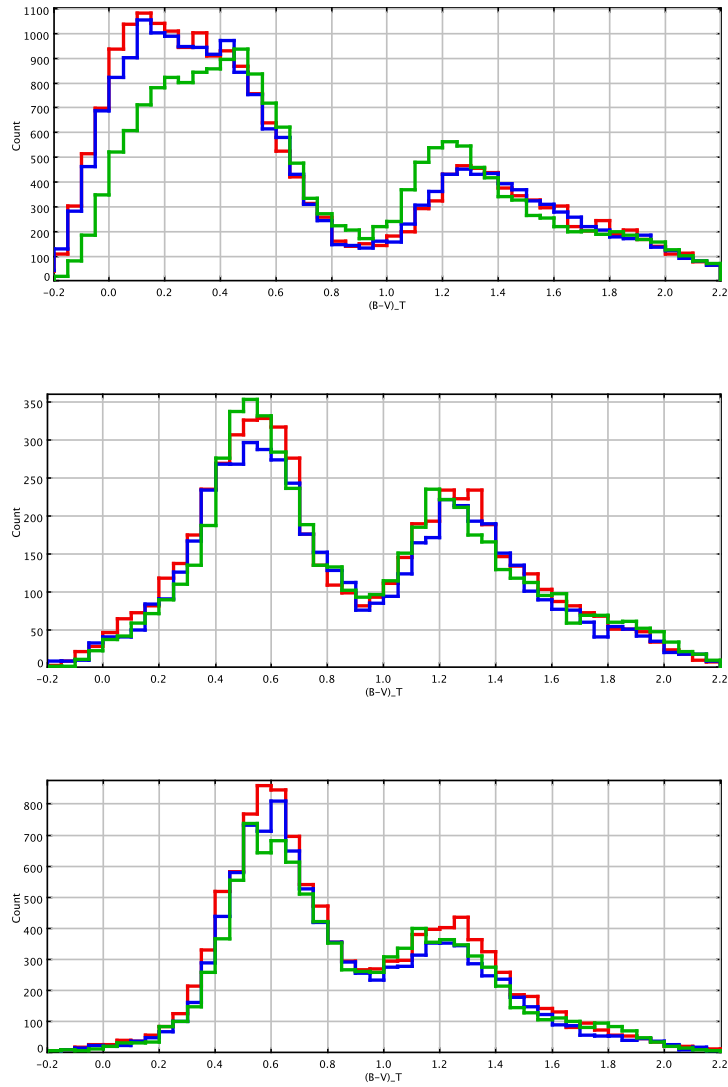


Figure 5.29: $(B - V)_T$ distributions towards our three established regions: at the top Galactic plane, in the middle intermediate latitudes and at the bottom the Galactic North Pole. In green Tycho-2 data, in red the simulations with total local dynamical mass of Cr ez e et al. (1998) and in blue the value from van Leeuwen (2007).

5.2.11 Age-velocity relation

In section 3.7 we present two sets of values for the age-velocity relation (see Table 3.11), which have been used in our analysis. Those values correspond to Gómez et al. (1997) and Holmberg et al. (2009) relations. We have applied both sets of values in our simulations and checked if the produced synthetic LF differ. Then we have also investigated what is the impact of that parameter on the resulting star counts and $(B - V)_T$ distributions when compared to observations.

In Table 5.7 we show the values of $\epsilon(i)$, $RSVd(i)$, $\rho_{\odot}^{all}(i)$ and $\Sigma_{\odot}^{all}(i)$ which were obtained in both cases. Differently than in section 5.2.10 here we can notice the change in the total local volume density of stars, although is very small. The total local surface mass density has changed more significantly than in section 5.2.10 and the difference between two cases is of about 16 per cent.

component	Holmberg et al. (2009) AVR				Gómez et al. (1997) AVR			
	ϵ	$RSVd(i)$	$\rho_{\odot}^{all}(i)$	$\Sigma_{\odot}^{all}(i)$	ϵ	$RSVd(i)$	$\rho_{\odot}^{all}(i)$	$\Sigma_{\odot}^{all}(i)$
1	0.0140	129.90	0.0022	0.2843	0.0140	129.90	0.0018	0.2396
2	0.0199	245.96	0.0069	1.7107	0.0203	250.76	0.0057	1.4419
3	0.0284	348.42	0.0064	2.2488	0.0290	355.68	0.0053	1.8955
4	0.0467	570.35	0.0044	2.5355	0.0437	533.91	0.0040	2.1372
5	0.0632	770.93	0.0079	6.0712	0.0561	684.59	0.0075	5.1174
6	0.0797	971.49	0.0079	7.7180	0.0637	777.01	0.0084	6.5054
7	0.0986	1200.10	0.0130	15.627	0.0642	783.09	0.0168	13.172
			0.0488	36.1958			0.04959	30.5092

Table 5.7: The changes in values of ϵ , $RSVd(i)$, $\rho_{\odot}^{all}(i)$ and $\Sigma_{\odot}^{all}(i)$ values when Holmberg et al. (2009) and Gómez et al. (1997) age-velocity relations applied in our default model.

In Fig. 5.30 we see that the change is noticeable only in the bright part of the LF, which corresponds exactly to our Tycho-2 sample. This is why we can notice changes in the star counts and appearance of colour histograms, see Fig. 5.31. One can clearly see that when using Holmberg et al. (2009) age-velocity relation we produce too many giants at the Galactic pole and too many bright stars within the plane. We conclude that Gómez et al. (1997) age-velocity relation provides a better fit to Tycho-2 data in case of our best fit IMF and SFR, thus we keep it in our default model A and B.

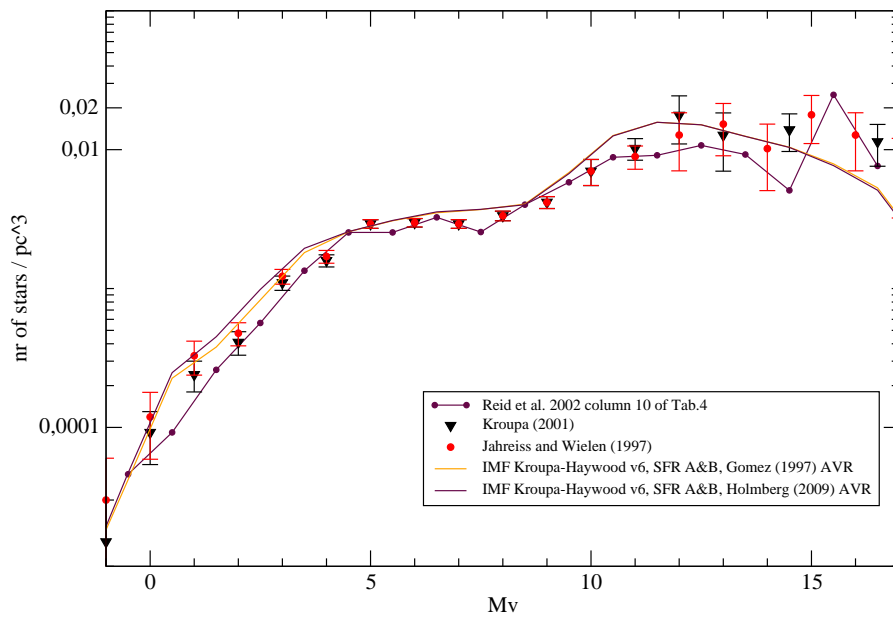


Figure 5.30: The comparisons of LFs between data and model when two different age-velocity relations were imposed.

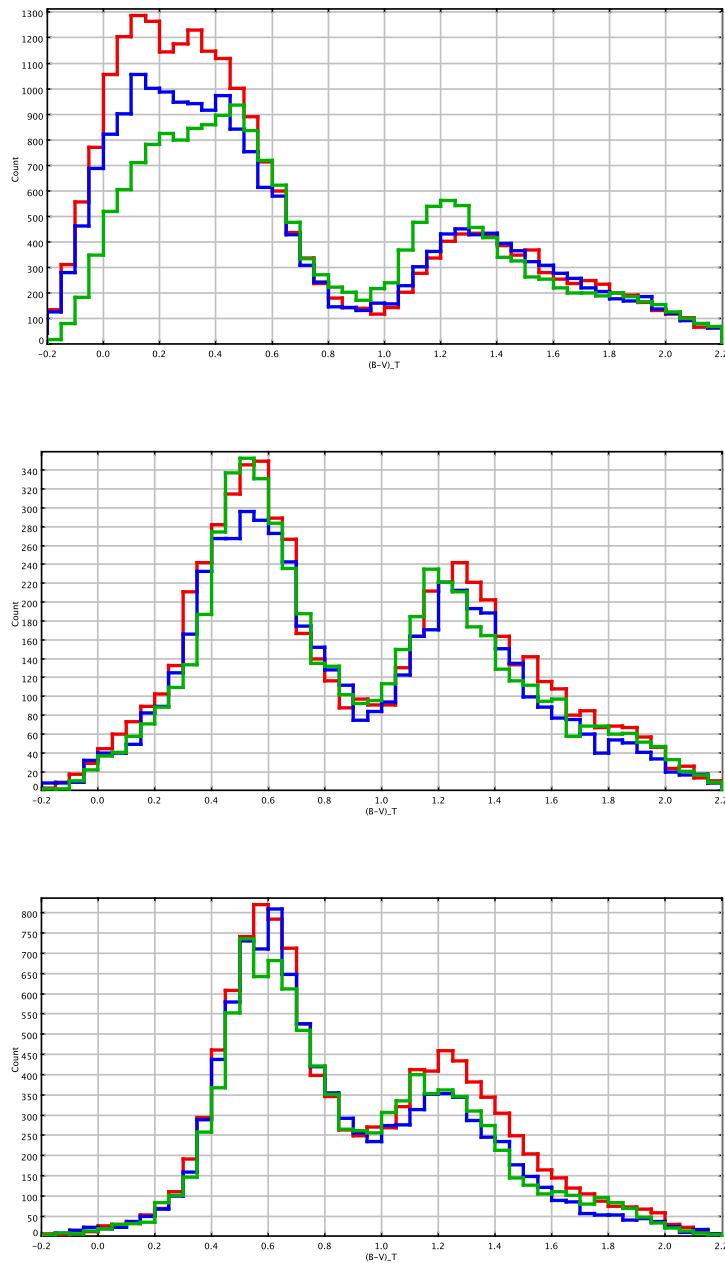


Figure 5.31: $(B - V)_T$ distributions towards our three established regions: at the top Galactic plane, in the middle intermediate latitudes and at the bottom the Galactic North Pole. In green Tycho-2 data, in red the simulations with age-velocity relation of Holmberg et al. (2009) and in blue the relation from Gómez et al. (1997).

5.2.12 Radial scale length

We have checked what happens to the $(B - V)_T$ distribution if the radial scale length of the youngest populations is changed. In our default model the values of that parameter are the following:

- Young disc (first age subpopulation $\tau < 150$ Myr): $h_R = 5000.0$ pc;
- Old disc (from the second to the seventh age bin $\tau > 150$ Myr): $h_R = 2400.0$ pc.

In our test we have changed the values of h_R for the first three thin disc subcomponents and the rest remained as previously:

- first age subpopulation ($\tau < 150$ Myr): $h_R = 5500.0$ pc;
- second age subpopulation ($150 \text{ Myr} < \tau < 1 \text{ Gyr}$): $h_R = 5000.0$ pc;
- third age subpopulation ($1 \text{ Gyr} < \tau < 2 \text{ Gyr}$): $h_R = 3500.0$ pc;
- from fourth to seventh age subpopulation ($\tau > 2 \text{ Gyr}$): $h_R = 2400.0$ pc.

The changes we applied to h_R values were significant and our intention was to see if this can cause an important change in the star counts and distribution of colour within the Galactic plane. It must be emphasized that our test was limited to Tycho-2 data, which do not go far away from the solar neighborhood. In Fig. 5.32 we see the $(B - V)_T$ histograms for the plane, in green the Tycho data, in red our default model (with the default values of scale lengths) and in black our default model with the new values of scale lengths for the three youngest subcomponents of the thin disc. In Fig. 5.33 similar comparisons for the four cardinal directions within the Galactic plane (from top to bottom: the center, anticenter, rotation and antirotation). We conclude that Tycho data alone can not constrain enough the scale lengths of the thin disc. The change we have done produces a slight improvement of the model towards the Galactic center for the blue peak (main sequence stars), while it is slightly worse towards the anticenter for the red peak (giants). Towards rotation and antirotation, as expected, the change is minor. An investigation of the scale length would need to be investigated looking at larger distances inward and outward, as it was done for example using 2MASS data with the previous BGM. For that we conclude to keep the default values of the scale lengths.

At last, in the light of our general results it is worth commenting the exercise done in this section. One can see that the radial scale length is another parameter, which plays a role in the problematic part of our $(B - V)_T$ histograms corresponding to the blue and hot stars ($(B - V)_T < 0.4$).

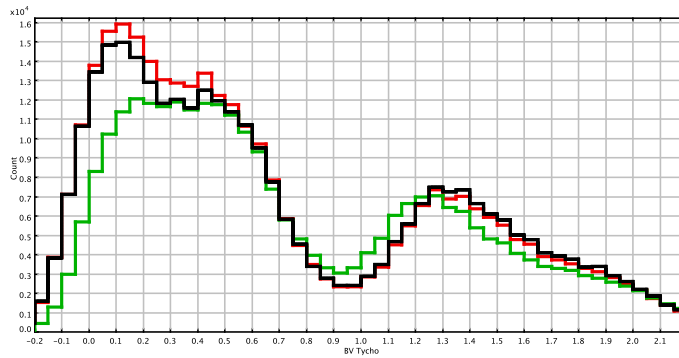


Figure 5.32: The $(B - V)_T$ distributions of stars within the Galactic plane $b=(-10^\circ;10^\circ)$, in green Tycho stars, in red the default model with the default values of radial scale lengths and in black the default model with the new values of radial scale lengths.

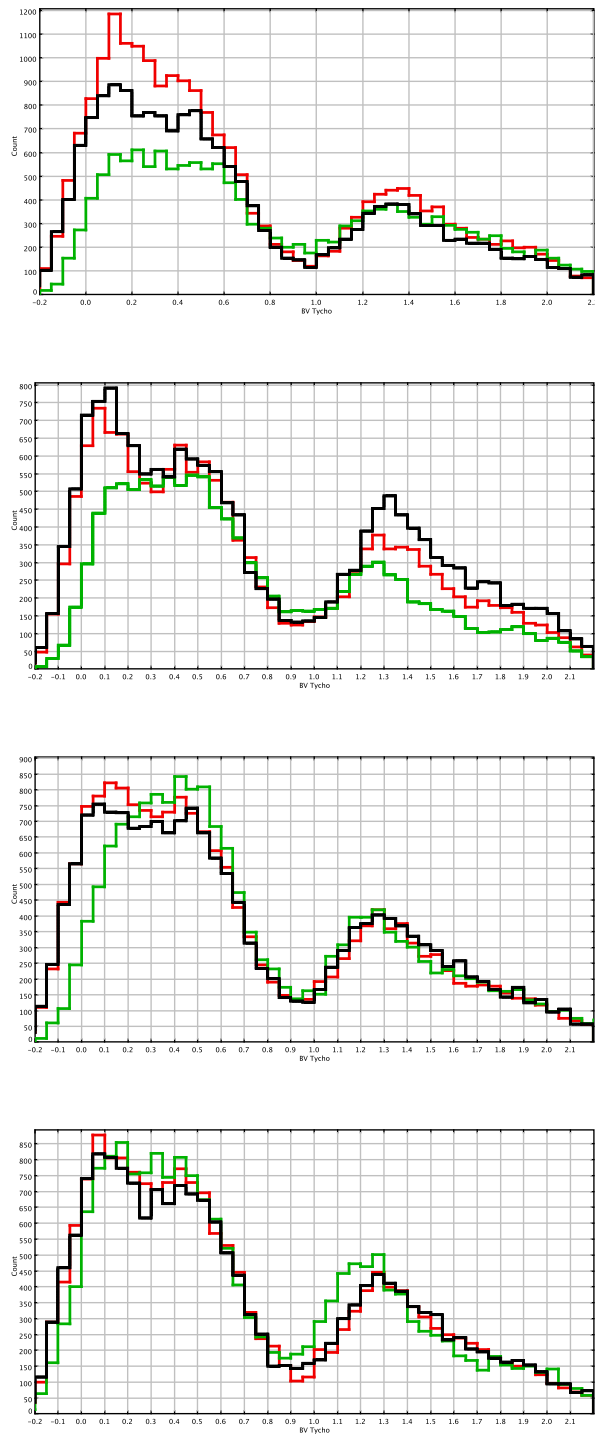


Figure 5.33: The $(B - V)_T$ distributions in four cardinal directions subsequently from the top to bottom the Galactic center, anticenter, rotation and antirotation. In green Tycho stars, in red the default model with the default values of radial scale lengths and in black the default model with the new values of radial scale lengths.

5.3 Looking for the best fit with Tycho-2 data

As reported in this chapter we went a long way on the model improving and parameters fitting in order to understand a bit more our home Galaxy. In this final section we show the whole sky comparison between the old model Robin et al. (2003) (the version of the old model that we used in 2009 includes some small updates which are listed on the official web site of the model, see BGM website), our two new default models applying Haywood-Robin and Kroupa-Haywood v6 IMF (see Table 5.1) and Tycho-2 data. We remind that our simulated and observed samples are magnitude limited. The cut was made at $V_T = 11$ mag in order to work with the magnitude complete Tycho-2 sub-sample. In Fig. 5.34 at the top we present the cumulative whole sky $(B - V)_T$ distributions of each of them. It is crucial to notice the enormous changes in the appearance of the $(B - V)_T$ histogram of our new model with respect to the old model. We have significantly decreased the number of objects in both peaks making it much more similar to the star counts of the Tycho-2 sample, also see Table 5.8. We have improved as well the appearance of the histogram. The red peak of giant stars has been shifted by more than 0.1 mag towards blue colours fitting significantly better the giants peak of Tycho-2 data. The excess of the blue stars around $(B - V)_T \sim 0.1$ mag has been significantly reduced.

From Fig. 5.34 and 5.18 we also derive the conclusions that our default model A (Haywood-Robin IMF) performs better in the blue peak of the $(B - V)_T$ distribution, while the default model B (Kroupa-Haywood v6 IMF) fits better the giants peak. From the whole sky star counts presented in Table 5.8 we conclude that model A produces in total a little bit less stars than Tycho-2 sample, while model B a little bit more. Model B differs within the plane and for intermediate and high latitudes it reproduces the Tycho-2 star counts very well, while model A performs very good in the plane and produces too less stars at higher latitudes. As clearly seen the old model generates too many stars at all latitudes.

In Fig. 5.34 at the bottom we clearly observe that our two best fit IMF from comparisons with Tycho-2 $(B - V)_T$ distributions, Haywood-Robin and Kroupa-Haywood v6 IMF differ at the bright tail of the LF, that is in the M_V range between (0;4) mag. It could suggest that in the bright domain Jahreiß and Wielen (1997) LF provides too many stars, whereas Reid et al. (2002) LF too few objects. It is possible that the real LF falls somewhere in between the data points of the LF derived by two authors, both using the new Hipparcos data.

In Fig. 5.35 and 5.36 we present the whole sky maps of the mean $(B - V)_T$ colours between our default model A and Tycho-2 data and the relative number of objects between both sets ($(\text{model A} - \text{Tycho})/\text{Tycho}$), separately for both peaks of the colour distribution. Whereas in Fig. 5.37 and 5.38 the same whole sky comparisons are made, but between our two default models, model A and B. We recommend the reader to compare them with the sky maps obtained with the old model presented in Fig. 5.1 and 5.2.

From Fig. 5.35 where we compare the mean colours of model A and Tycho-2 data we conclude that the range of differences in colours is similar as when the old model was used. However, a clear shift in the red peak is noticed what was one of our biggest improvements. What is also notable when comparing the old and new sky maps is that the most characteristic features of the sky remain. We especially mean here the characteristic regions within the Galactic plane. When we look at the maps of the relative number of objects presented in Fig. 5.36 we clearly see that those special regions within the plane where some discrepancies in colours are present correspond to areas of the sky where Tycho-2 star counts are much less than in our model (those regions are clearly seen in Fig.1 from Høg et al. (2000)). Following Lucke (1978) the two most

problematic regions can be associated with dust clouds, the Taurus dark cloud at $l=174^\circ$ and 175 pc and the large complex Aquila rift between $l=10^\circ$ and $l=55^\circ$ running from 50 pc to 375 pc. From our analysis we might expect that the extinction models we are using have problems when reproducing those close dark matter clouds. As well some other effects neglected in our comparisons can interfere within the plane as spiral structure, star forming regions, Gould belt, etc.

In spite of those particular discrepancies one can notice in the scales of Fig. 5.36 that the general star counts obtained with the new model have improved significantly. The range of the relative number of objects for both peaks was decreased by a factor of two.

In the Fig. 5.37 we notice that there is almost no shift of the blue peak between our two default models as expected from Fig. 5.34 top. The fact that in the sky map corresponding to the red peak we observe some shift in the model is due to the clustering algorithm applied to regions with little number of objects. It may occur that if there are not too many stars at some high latitude region and if both peaks of the corresponding $(B - V)_T$ distribution are relatively close the output of the clustering might be a bit different than in the case of the field with many objects. This is what we notice in Fig. 5.38 as well. As can be seen in Fig. 5.18 differences between models A and B at latitude $> 30^\circ$ are negligible, thus it is clear that discrepancies in the blue and red peak in Fig. 5.37 and 5.38 are not real and shall be considered random errors due to the low number of objects.

number of objects	model A	model B	old model
total	758372	959569	1279867
compared to our Tycho-2 sub-sample (860743)	12 % less	11 % more	50 % more
$b=(-10^\circ;10^\circ)$	275730	373414	465907
compared to our Tycho-2 sub-sample (288661)	5 % less	30 % more	61 % more
$b=(-30^\circ;-10^\circ)$ & $b=(10^\circ;30^\circ)$	263069	333372	472501
compared to our Tycho-2 sub-sample (322857)	19 % less	3 % more	15 % more
$b=(-90^\circ;-30^\circ)$ & $b=(30^\circ;90^\circ)$	219573	252783	341459
compared to our Tycho-2 sub-sample (249225)	12 % less	1 % more	37 % more

Table 5.8: Whole sky star counts obtained with our default model A and B and the old model with respect to Tycho-2 data.

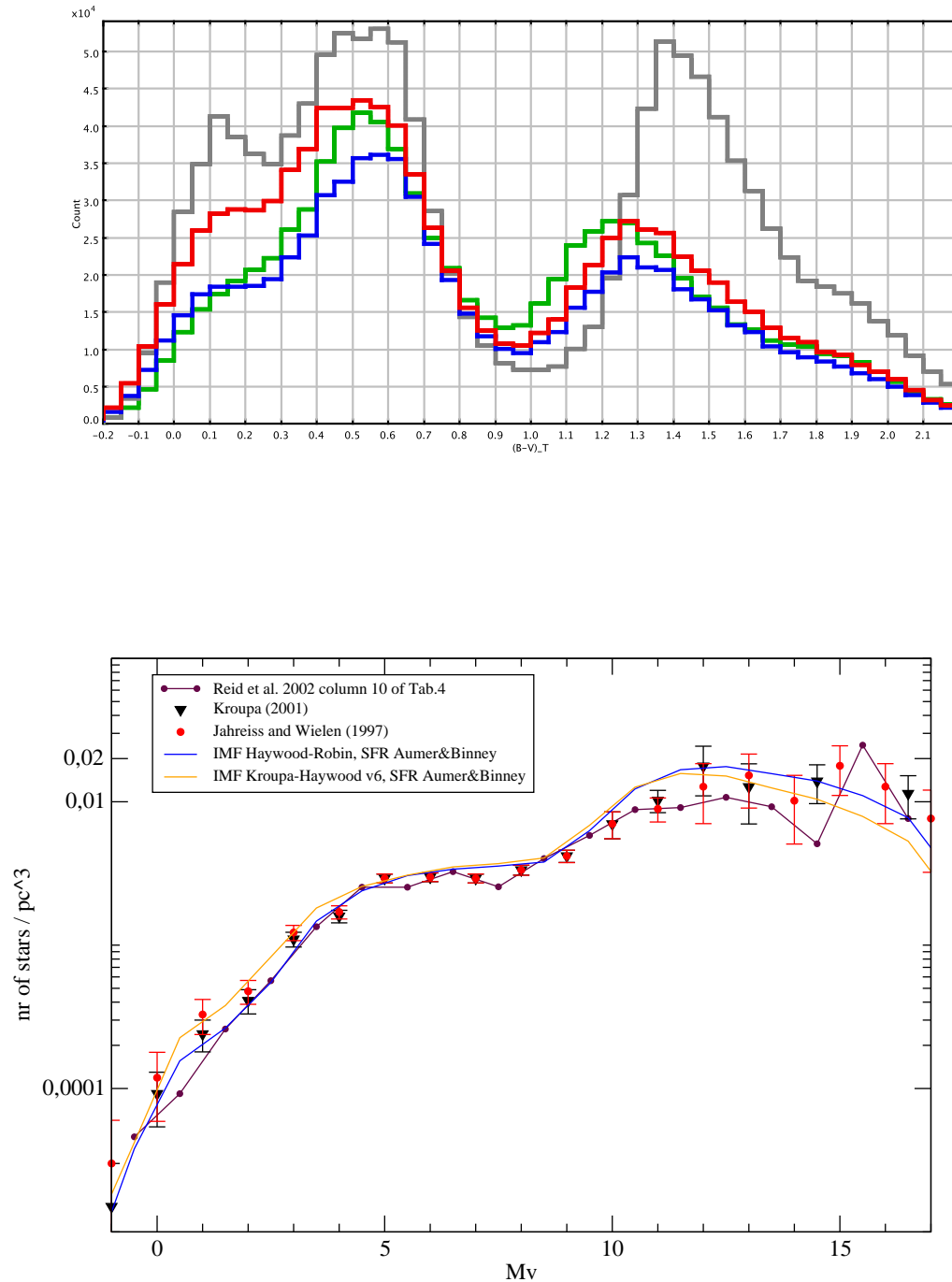


Figure 5.34: Top: The cumulative whole sky $(B - V)_T$ distributions of the old model (grey), our two new default models (in blue Haywood-Robin IMF and in red Kroupa-Haywood v6 IMF) and Tycho-2 data (in green). Bottom: Comparison of the synthetic LF obtained with our default model A and B to the observed LF.

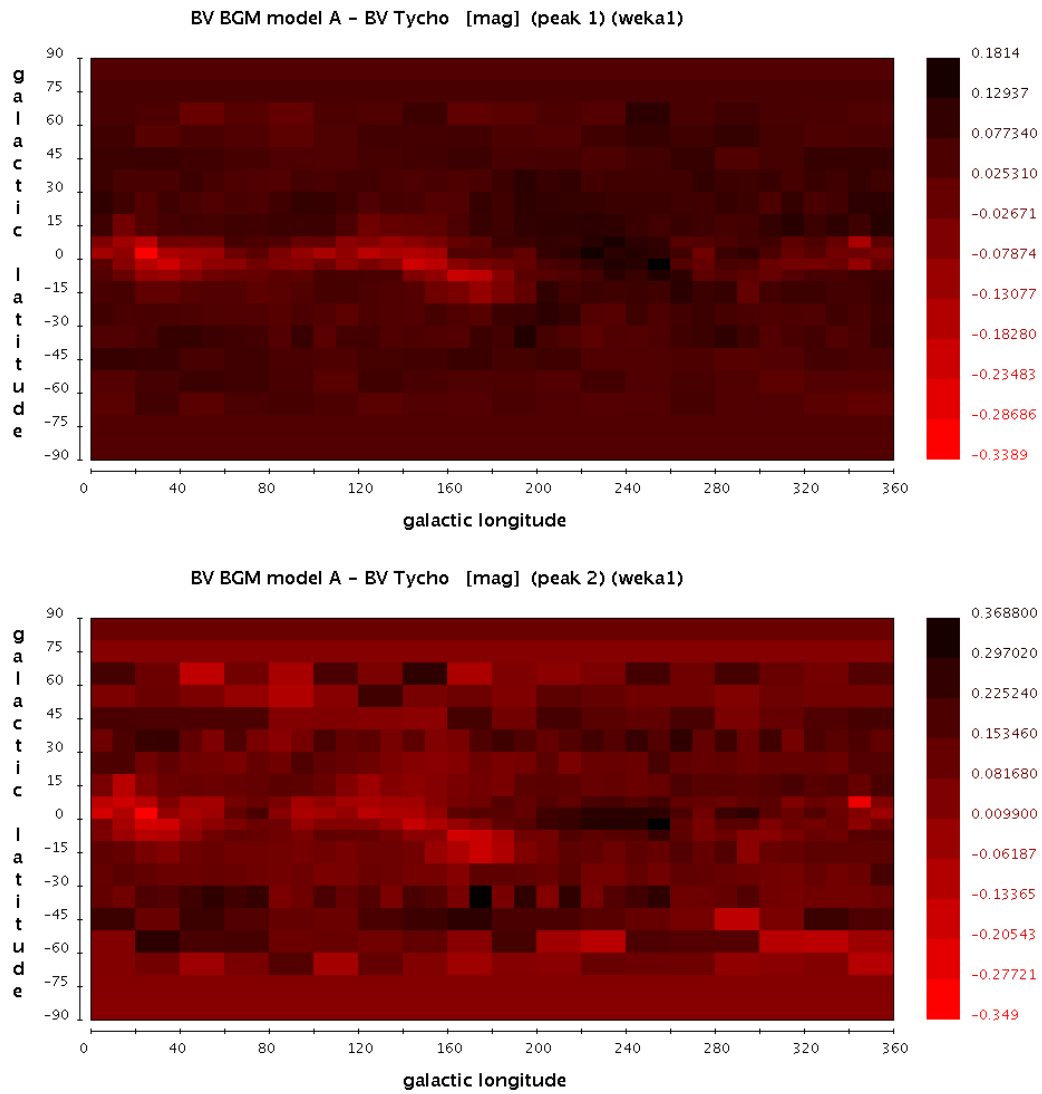


Figure 5.35: The sky maps where the new BGM model A is compared to Tycho-2 data. The differences of the mean $(B - V)_T$ colours between model and data for the stars belonging to the blue peak of $(B - V)_T$ distribution (top) and to the red peak of $(B - V)_T$ distribution (bottom).

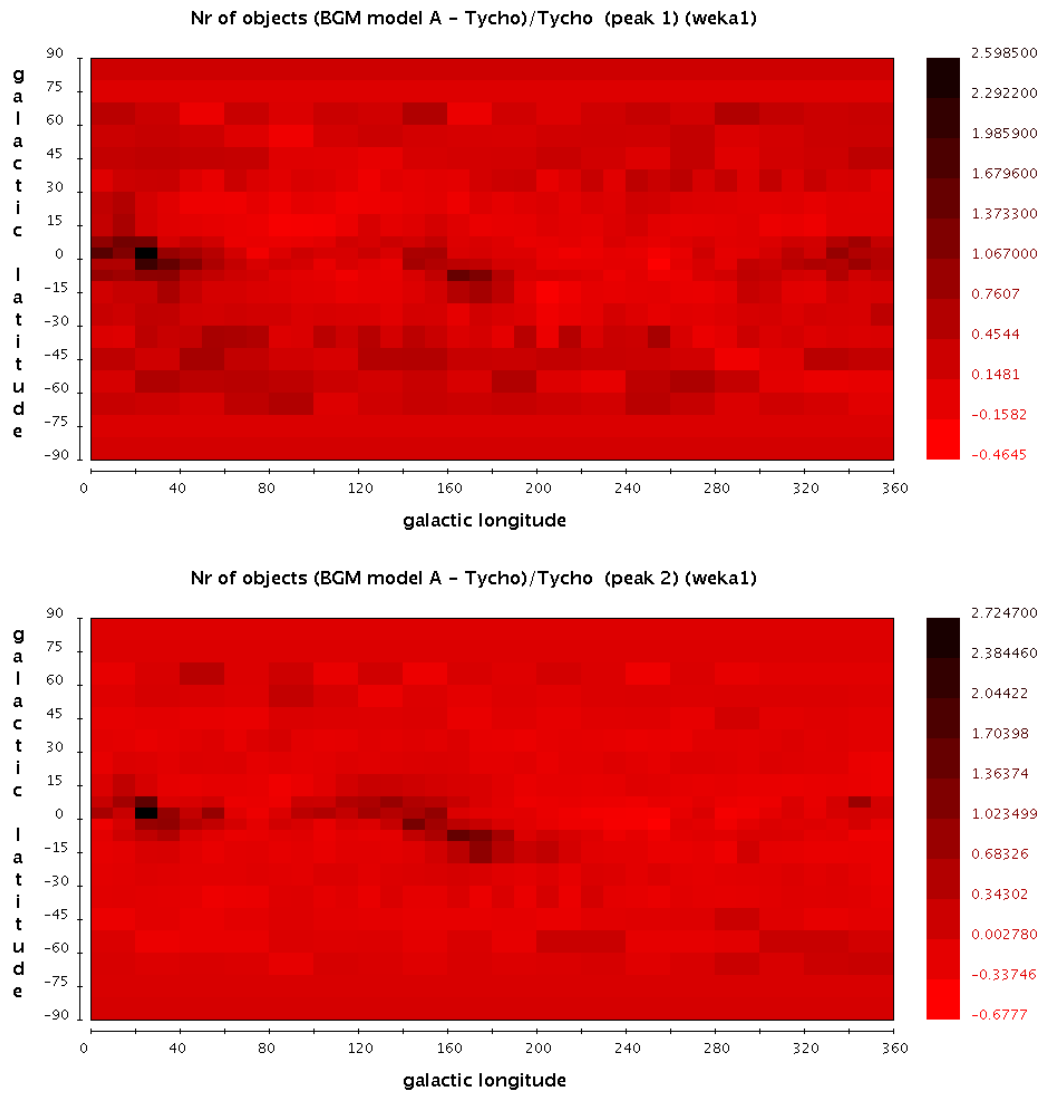


Figure 5.36: The sky maps where the new BGM model A is compared to Tycho-2 data. The relative number of objects $((\text{model A} - \text{Tycho})/\text{Tycho})$ corresponding to the blue peak of $(B-V)_T$ distribution (top) and the red peak of $(B-V)_T$ distribution (bottom).

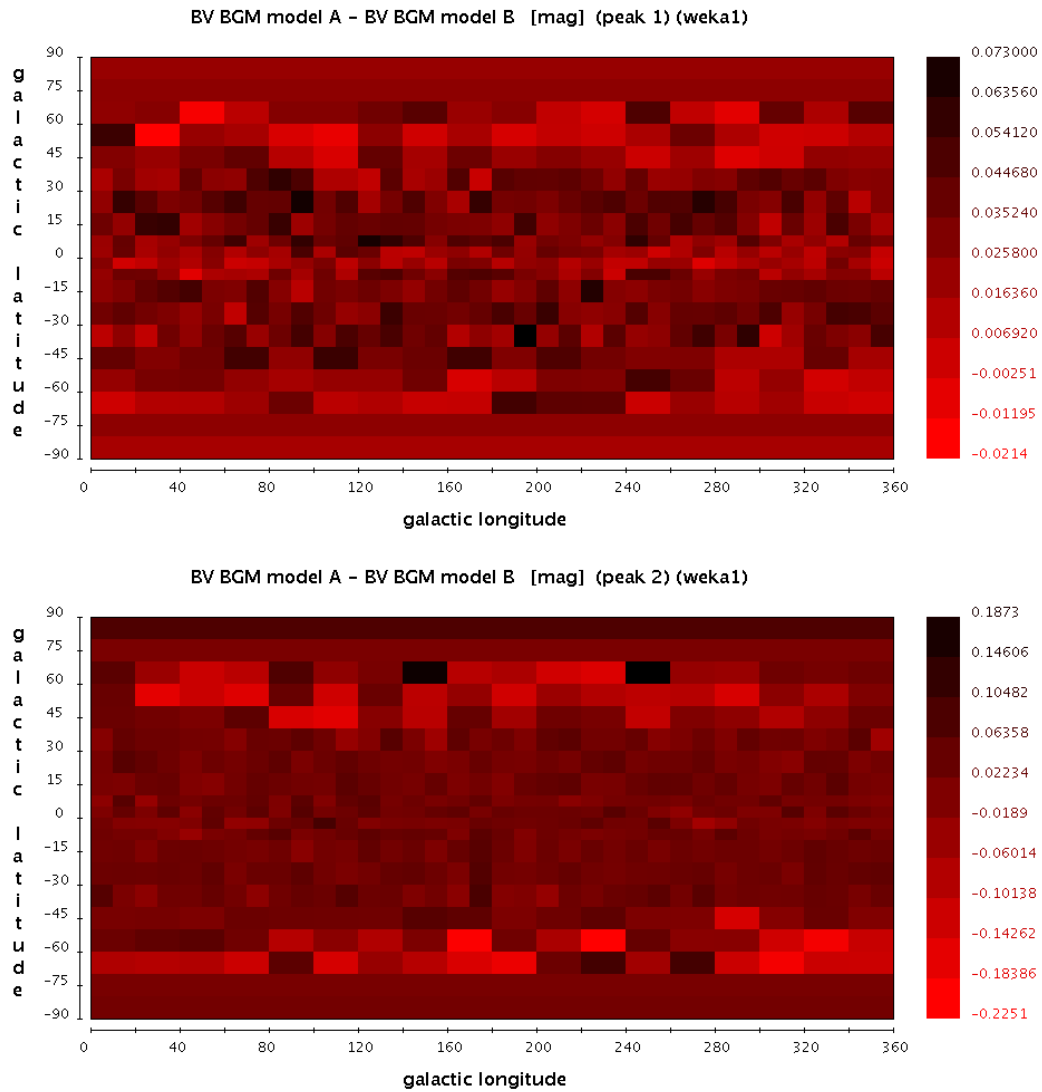


Figure 5.37: The sky maps where the new BGM model A is compared to new BGM model B. The differences of the mean $(B - V)_T$ colours between model and data for the stars belonging to the blue peak of $(B - V)_T$ distribution (top) and to the red peak of $(B - V)_T$ distribution (bottom).

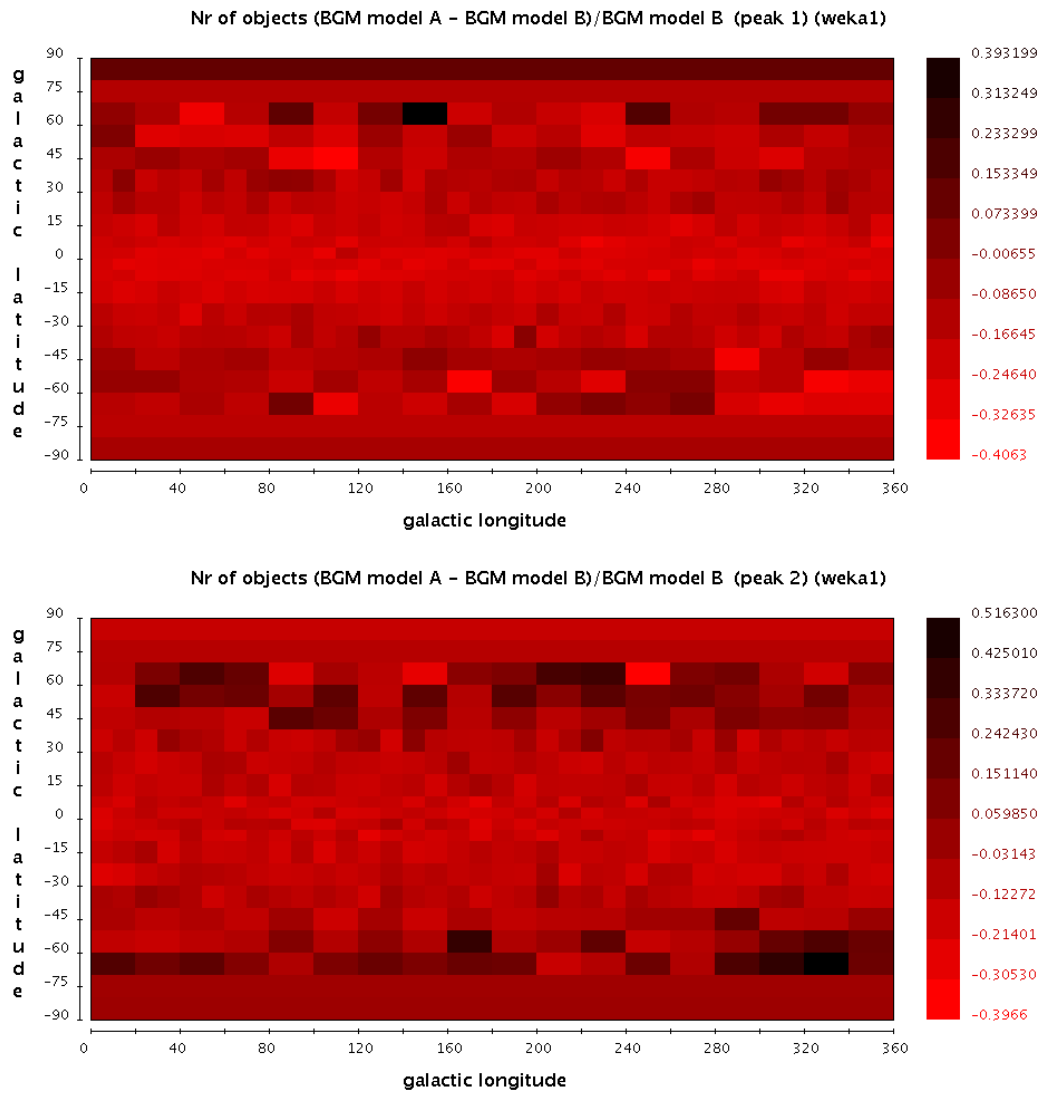


Figure 5.38: The sky maps where the new BGM model A is compared to new BGM model B. The relative number of objects $((\text{model A} - \text{Tycho})/\text{Tycho})$ corresponding to the blue peak of $(B - V)_T$ distribution (top) and the red peak of $(B - V)_T$ distribution (bottom).

Chapter 6

Conclusions

In this PhD project, we have designed, implemented and tested a new version of the Besançon Galaxy Model. In order to accomplish that goal we have performed a coding task which has provided an important change in the star production philosophy. Our work is constrained to the thin disc population only. Although the remaining populations are treated as in the old model, the improvement in the thin disc model proposed here applies to more than 95 % of the stellar content of the solar neighborhood. In the near future the new scheme will be extended to the other populations as well.

The most important improvement of the new model presented here is that we have turned the initial mass function (IMF), the star formation rate (SFR) and stellar evolutionary tracks into free user-specified parameters. It means that the new code produces synthetic stars according to the evolutionary scenarios selected by the user which can be changed from run to run. That has expanded the field of our investigation, because by comparing the results from our new model with observations we are able to test several scenarios of the evolution of our Galaxy. The second most important improvement of the new model is that we have implemented binarity. It means that in its present form, the new BGM is able to produce binary systems remaining in the agreement with the constraints on the local mass density in stars and the user's observational constraint (spatial resolution). It is considered a significant improvement, since binaries can account for about 50 % of the total stellar content of the Milky Way.

We have updated several of the model's inputs as for example the age-metallicity relation, the atmosphere models or the total dynamical mass. Additionally we have enriched our analysis by testing the two more detailed 3D extinction models available in the literature. Different solutions for the age of the thin disc, the local stellar mass density, the age-velocity dispersion σ_W relation and the radial scale lengths of the thin disc have been also tested.

In order to constrain the ingredients of our new model we have used two observational sets, the Tycho-2 data and the local LF (luminosity function). We have tested different scenarios of many inputs of the model as presented in chapter 5. Our strategy was to compare our new model and Tycho-2 data in the context of star counts and $(B - V)_T$ distributions for three selected standard regions at different latitudes, each time that any model's input has been changed (the strategy followed in chapter 5). When any of the evolutionary parameters was modified the synthetic LF was calculated and compared to the observed ones. Whenever we have seen that a more general comparison was needed we have performed the whole sky analysis.

One of the most crucial parts of our investigation was to look for the best fit IMF and SFR

able to reproduce the whole sky Tycho-2 data. Ten different IMF have been tested along with three SFR, a constant and two decreasing ones (see section 5.2.2). Here we summarize our main conclusions.

We confirm that when a constant SFR was assumed, no matter which IMF was used, we were not able to reproduce the Tycho-2 star counts and $(B - V)_T$ distributions within the Galactic plane. The model always shows a significant excess of the blue stars. This result strongly favours a decreasing SFR. Those conclusions are coherent with the results from the fitting of the local LF. A constant SFR produces too many bright objects no matter which IMF have been used. We conclude that the constant SFR was the main reason why the old model Robin et al. (2003) gave a significant excess of bright blue stars. Later on we have checked that the two decreasing SFR we tried, the decreasing exponential SFR of Aumer and Binney (2009) and the SFR of the model A from Just and Jahreiß (2010) (see Fig. 3.3), led to similar results when compared to Tycho-2 data.

The conclusions we have derived about the IMF when comparing the Tycho-2 data with our synthetic catalogues are the following:

- Vallenari et al. (2006) IMF, when combined with the decreasing SFR of Aumer and Binney (2009), produces too many stars within the Galactic plane and almost acceptable results at higher latitudes. The excess of star counts is also observed in the fit to the local LF.
- Kroupa (2008) IMF produces an artificial bump of blue and bright stars which is not seen in Tycho-2 sample, suggesting that the slope proposed by this author for the high masses range is not correct.
- Just and Jahreiß (2010) IMF used with two different decreasing SFR (including their best fit SFR) is not able to reproduce correctly the Tycho-2 $(B - V)_T$ distribution within the plane, however at higher latitudes it performs good.
- The fit provided by Haywood et al. (1997a) IMF is poor at intermediate latitudes and within the plane.
- Kroupa-Haywood v7 IMF one of the IMF proposed by us gives a good fit to Tycho-2 data when combined with the decreasing SFR of Aumer and Binney (2009). However its fit to the LF above $M_V > 5$ mag is quite bad.
- From the comparisons of colour distributions between our new model and Tycho-2 data we conclude that Kroupa-Haywood v6 and Haywood-Robin IMF combined with the decreasing SFR of Aumer and Binney (2009) provide the best fit. We have checked that these two new combinations of IMF and SFR also fit well the local LF.

We have applied our two best fit IMF to our default model and this way we got the default model A (Haywood-Robin IMF) and B (Kroupa-Haywood v6 IMF). We have shown that the first one performs better in the blue peak of the $(B - V)_T$ distribution, while the second fits better the giants peak.

From the task of fitting the best IMF and SFR we have learned that constraining the bright stars of our simulations just by the LF is hard, because of big error bars there. Tycho-2 has served us as a stronger constraint in that range. As already mentioned from comparisons with Tycho-2 we got our two best fit IMF. We have seen that LF produced by them differ at the

bright tail of the LF, $M_V=(0;4)$ mag. It might suggest that in the bright domain Jahreiß and Wielen (1997) LF provides too many stars, whereas Reid et al. (2002) LF too few objects. It is possible that the real LF falls somewhere in between the data points of the LF derived by two authors, both using the new Hipparcos data.

We have tried two different values of the local stellar mass density and investigated the influence of that parameter on the resulting star counts and the produced LF. The results of our analysis might suggest that in order to fit better the Tycho-2 data with our default model A more mass density should be assumed in the local neighborhood than $0.039 M_\odot/pc^3$.

Using Tycho-2 data we have also constrained other ingredients. We have seen that simulations without binaries when compared to Tycho-2 star counts and colours perform worse within the plane. The excess of blue stars is bigger than in case of simulations with binaries and also the lack of binarity shifts the red peak of colour distribution making it less similar to the observed one.

We conclude that the extinction model is a crucial input of any Galaxy model and that the Marshall et al. (2006) extinction model probably underestimates the extinction at the very short distances where large dark clouds are present (such as Aquila rift, Taurus cloud, etc).

One of our biggest improvements with respect to the old model was that we have shifted the red peak of the $(B - V)_T$ distribution. This was achieved by updating the atmosphere models. As we have learned the BaSeL 2.2 library gives too red colours for giants when compared to Tycho-2, while the new BaSeL 3.1 library moves the red peak by about 0.1 mag towards bluer colours making it more similar to Tycho-2 giants.

We have updated the age-metallicity relation in the new model to the one proposed by Haywood (2006). It reproduces better both, the blue and the red peak of the colour distribution.

We have tried two different values of the total dynamical mass (Crézé et al. (1998) and van Leeuwen (2007)) and decided to keep the van Leeuwen (2007) value for that parameter as it leads to slightly better results at the Galactic pole.

Two age-velocity relations have been tested, one from Gómez et al. (1997) and the other from Holmberg et al. (2009). We have seen that when using Holmberg et al. (2009) age-velocity relation we produce too many giants at the Galactic pole and too many bright stars within the plane. We have concluded that Gómez et al. (1997) age-velocity relation provides a better fit to Tycho-2 data in case of our best fit IMF and SFR and we kept it in our default model A and B.

From the present work, once more we realize that the thin disc parameters are correlated and they interact with each other making the task of Galaxy modeling very challenging. Due to this multi-dependency to find the best solution for all free parameters is very demanding, thus requiring a huge amount of observational constraints.

The simulation of the Galaxy is a complex task due to both the theoretical concepts and the heavy computations that must be applied. We think that with the present work we have contributed to that challenging task. We have delivered a model, which is an ideal tool to test various scenarios of Galaxy formation and evolution. And this kind of tools will be greatly appreciated in the era of Gaia data.

Chapter 7

Bibliography

Bibliography

- F. Arenou. The simulated multiple stars. *Gaia DPAC*, January 2010.
- M. Aumer and J. J. Binney. Kinematics and history of the solar neighbourhood revisited. *MNRAS*, 397:1286–1301, August 2009. doi: 10.1111/j.1365-2966.2009.15053.x.
- S. A. Becker, Jr. I. Iben, and R. S. Tuggle. On the frequency-period distribution of Cepheid variables in galaxies in the Local Group. *Astrophysical Journal*, 218:633–653, December 1977. doi: 10.1086/155720.
- T. Bensby, A. R. Zenn, M. S. Oey, and S. Feltzing. Tracing the Galactic Thick Disk to Solar Metallicities. *The Astrophysical Journal*, 663:L13–L16, July 2007. doi: 10.1086/519792.
- G. Bertelli, A. Bressan, C. Chiosi, F. Fagotto, and E. Nasi. Theoretical isochrones from models with new radiative opacities. *Astronomy and Astrophysics*, 106:275–302, August 1994.
- G. Bertelli, L. Girardi, P. Marigo, and E. Nasi. Scaled solar tracks and isochrones in a large region of the Z-Y plane. I. From the ZAMS to the TP-AGB end for 0.15-2.5 M_{\odot} stars . *Astronomy and Astrophysics*, 484:815–830, June 2008. doi: 10.1051/0004-6361/20079165.
- G. Bertelli, E. Nasi, L. Girardi, and P. Marigo. Scaled solar tracks and isochrones in a large region of the Z-Y plane. II. From 2.5 to 20 M_{\odot} stars. *Astronomy and Astrophysics*, 508: 355–369, December 2009. doi: 10.1051/0004-6361/200912093.
- BGM website. Model of stellar population synthesis of the Galaxy. World Wide Web electronic publication. URL <http://model.obs-besancon.fr/>.
- O. Bienayme, A. C. Robin, and M. Creze. The mass density in our Galaxy. *Astronomy and Astrophysics*, 180:94–110, June 1987.
- J. Binney and M. Merrifield. *Galactic Astronomy*. 1998.
- J. Binney and S. Tremaine. *Galactic Dynamics: Second Edition*. Princeton University Press, 2008.
- L. Casagrande, C. Flynn, L. Portinari, L. Girardi, and R. Jimenez. The helium abundance and $\Delta Y/\Delta Z$ in lower main-sequence stars. *MNRAS*, 382:1516–1540, December 2007. doi: 10.1111/j.1365-2966.2007.12512.x.
- L. Casagrande, R. Schönrich, M. Asplund, S. Cassisi, I. Ramírez, J. Meléndez, T. Bensby, and S. Feltzing. New constraints on the chemical evolution of the solar neighbourhood and Galactic disc(s). Improved astrophysical parameters for the Geneva-Copenhagen Survey. *Astronomy and Astrophysics*, 530:A138, June 2011. doi: 10.1051/0004-6361/201016276.

- V. Castellani, A. Chieffi, and O. Straniero. The evolution through H and He burning of Galactic cluster stars. *Astrophysical Journal Supplement Series*, 78:517–536, February 1992. doi: 10.1086/191637.
- G. Chabrier. Galactic Stellar and Substellar Initial Mass Function. *The Publications of the Astronomical Society of the Pacific*, 115:763–795, July 2003. doi: 10.1086/376392.
- G. Chabrier. The Initial Mass Function: from Salpeter 1955 to 2005. In E. Corbelli, F. Palla, & H. Zinnecker, editor, *The Initial Mass Function 50 Years Later*, volume 327 of *Astrophysics and Space Science Library*, page 41, January 2005.
- G. Chabrier and I. Baraffe. Structure and evolution of low-mass stars. *Astronomy and Astrophysics*, 327:1039–1053, November 1997.
- C. Chiosi, E. Nasi, and S. R. Sreenivasan. Massive stars evolution with mass-loss. I - 20-100-solar-mass models. *Astronomy and Astrophysics*, 63:103–124, February 1978.
- L. M. Close, N. Siegler, M. Freed, and B. Biller. Detection of Nine M8.0-L0.5 Binaries: The Very Low Mass Binary Population and Its Implications for Brown Dwarf and Very Low Mass Star Formation. *The Astrophysical Journal*, 587:407–422, April 2003. doi: 10.1086/368177.
- M. Cr ez e, E. Chereul, O. Bienayme, and C. Pichon. The distribution of nearby stars in phase space mapped by Hipparcos. I. The potential well and local dynamical mass. *Astronomy and Astrophysics*, 329:920–936, January 1998.
- David Gilbert. JFreeChart: A free Java chart library. World Wide Web electronic publication. URL <http://www.jfree.org/jfreechart/>.
- E. F. del Peloso, L. da Silva, G. F. Porto de Mello, and L. I. Arany-Prado. The age of the Galactic thin disk from Th/Eu nucleocosmochronology. III. Extended sample. *Astronomy and Astrophysics*, 440:1153–1159, September 2005. doi: 10.1051/0004-6361:20053307.
- R. Drimmel and D. N. Spergel. Three-dimensional Structure of the Milky Way Disk: The Distribution of Stars and Dust beyond $0.35 R_{\text{solar}}$. *The Astrophysical Journal*, 556:181–202, July 2001. doi: 10.1086/321556.
- A. Duquennoy and M. Mayor. Multiplicity among solar-type stars in the solar neighbourhood. II - Distribution of the orbital elements in an unbiased sample. *Astronomy and Astrophysics*, 248:485–524, August 1991.
- ESA. The Hipparcos and Tycho Catalogues. *ESA SP-1200*, Volume 1, 1997.
- K. Fuhrmann. Nearby stars of the Galactic disc and halo - V. *MNRAS*, 414:2893–2922, July 2011. doi: 10.1111/j.1365-2966.2011.18476.x.
- A. E. G omez, S. Grenier, S. Udry, M. Haywood, L. Meillon, V. Sabas, A. Sellier, and D. Morin. Kinematics of Disk Stars in the Solar Neighbourhood. In R. M. Bonnet, E. H og, P. L. Bernacca, L. Emiliani, A. Blaauw, C. Turon, J. Kovalevsky, L. Lindgren, H. Hassan, M. Bouffard, B. Strim, D. Heger, M. A. C. Perryman, & L. Woltjer, editor, *Hipparcos - Venice '97*, volume 402 of *ESA Special Publication*, pages 621–624, August 1997.
- N. Grevesse and A. J. Sauval. Standard Solar Composition. *Space Science Reviews*, 85:161–174, May 1998. doi: 10.1023/A:1005161325181.

- M. Haywood. Revisiting two local constraints of the Galactic chemical evolution. *MNRAS*, 371: 1760–1776, October 2006. doi: 10.1111/j.1365-2966.2006.10802.x.
- M. Haywood. The model of stellar evolution of the galactic disc: The IMF at low masses. *Astronomy and Astrophysics*, 282:444–451, February 1994.
- M. Haywood, A. C. Robin, and M. Creze. The evolution of the Milky Way disc. I. Vertical structure and local constraints. *Astronomy and Astrophysics*, 320:428–439, April 1997a.
- M. Haywood, A. C. Robin, and M. Creze. The evolution of the Milky Way disc. II. Constraints from star counts at the galactic poles. *Astronomy and Astrophysics*, 320:440–459, April 1997b.
- E. Høg, C. Fabricius, V. V. Makarov, S. Urban, T. Corbin, G. Wycoff, U. Bastian, P. Schwendiek, and A. Wicenec. The Tycho-2 catalogue of the 2.5 million brightest stars. *Astronomy and Astrophysics*, 355:L27–L30, March 2000.
- J. Holmberg, B. Nordström, and J. Andersen. The Geneva-Copenhagen survey of the solar neighbourhood. III. Improved distances, ages, and kinematics. *Astronomy and Astrophysics*, 501:941–947, July 2009. doi: 10.1051/0004-6361/200811191.
- M. L. Houdashelt, R. A. Bell, and A. V. Sweigart. Improved Color-Temperature Relations and Bolometric Corrections for Cool Stars. *The Astrophysical Journal*, 119:1448–1469, March 2000. doi: 10.1086/301243.
- H. Jahreiß and R. Wielen. The impact of HIPPARCOS on the Catalogue of Nearby Stars. The stellar luminosity function and local kinematics. In R. M. Bonnet, E. Høg, P. L. Bernacca, L. Emiliani, A. Blaauw, C. Turon, J. Kovalevsky, L. Lindegren, H. Hassan, M. Bouffard, B. Strim, D. Heger, M. A. C. Perryman, and L. Woltjer, editors, *Hipparcos - Venice '97*, volume 402 of *ESA Special Publication*, pages 675–680, August 1997.
- A. Just and H. Jahreiß. Towards a fully consistent Milky Way disc model - I. The local model based on kinematic and photometric data. *MNRAS*, 402:461–478, February 2010. doi: 10.1111/j.1365-2966.2009.15893.x.
- P. Kroupa. The Local Stellar Initial Mass Function. In S. Deiters, B. Fuchs, A. Just, R. Spurzem, and R. Wielen, editors, *Dynamics of Star Clusters and the Milky Way*, volume 228 of *Astronomical Society of the Pacific Conference Series*, page 187, 2001.
- P. Kroupa. The IMF of Simple and Composite Populations. In J. H. Knapen, T. J. Mahoney, & A. Vazdekis, editor, *Pathways Through an Eclectic Universe*, volume 390 of *Astronomical Society of the Pacific Conference Series*, page 3, June 2008.
- T. Lejeune, F. Cuisinier, and R. Buser. Standard stellar library for evolutionary synthesis. I. Calibration of theoretical spectra. *Astronomy and Astrophysics Supplement series*, 125: 229–246, October 1997. doi: 10.1051/aas:1997373.
- T. Lejeune, F. Cuisinier, and R. Buser. A standard stellar library for evolutionary synthesis. II. The M dwarf extension. *Astronomy and Astrophysics*, 130:65–75, May 1998. doi: 10.1051/aas:1998405.
- P. B. Lucke. The distribution of color excesses and interstellar reddening material in the solar neighborhood. *ap*, 64:367–377, March 1978.

- D. J. Marshall, A. C. Robin, C. Reylé, M. Schultheis, and S. Picaud. Modelling the Galactic interstellar extinction distribution in three dimensions. *Astronomy and Astrophysics*, 453: 635–651, July 2006. doi: 10.1051/0004-6361:20053842.
- J. G. Mengel, P. Demarque, A. V. Sweigart, and P. G. Gross. Stellar evolution from the zero-age main sequence. *Astrophysical Journal Supplement Series*, 40:733–791, August 1979. doi: 10.1086/190603.
- D. Mihalas and P. M. Routly. *Galactic astronomy*. 1968.
- I. N. Reid, J. E. Gizis, and S. L. Hawley. The Palomar/MSU Nearby Star Spectroscopic Survey. IV. The Luminosity Function in the Solar Neighborhood and M Dwarf Kinematics. *The Astronomical Journal*, 124:2721–2738, November 2002. doi: 10.1086/343777.
- C. Reylé and A. C. Robin. Early galaxy evolution from deep wide field star counts. II. First estimate of the thick disc mass function. *Astronomy and Astrophysics*, 373:886–894, July 2001. doi: 10.1051/0004-6361:20010680.
- C. Reylé, D. J. Marshall, A. C. Robin, and M. Schultheis. The Milky Way’s external disc constrained by 2MASS star counts. *Astronomy and Astrophysics*, 495:819–826, March 2009. doi: 10.1051/0004-6361/200811341.
- A. Robin and M. Crézé. Stellar populations in the Milky Way - A synthetic model. *Astronomy and Astrophysics*, 157:71–90, March 1986.
- A. C. Robin, C. Reylé, S. Derrière, and S. Picaud. A synthetic view on structure and evolution of the Milky Way. *Astronomy and Astrophysics*, 409:523–540, October 2003. doi: 10.1051/0004-6361:20031117.
- A. C. Robin, D. J. Marshall, M. Schultheis, and C. Reylé. Stellar populations in the Milky Way bulge region: towards solving the Galactic bulge and bar shapes using 2MASS data. *Astronomy and Astrophysics*, 538:A106, February 2012. doi: 10.1051/0004-6361/201116512.
- G. Schaller, D. Schaerer, G. Meynet, and A. Maeder. New grids of stellar models from 0.8 to 120 solar masses at $Z = 0.020$ and $Z = 0.001$. *Astronomy and Astrophysics*, 96:269–331, December 1992.
- M. F. Sterzik and R. H. Durisen. Are Binary Separations related to their System Mass? In C. Allen and C. Scarfe, editors, *Revista Mexicana de Astronomia y Astrofisica Conference Series*, volume 21 of *Revista Mexicana de Astronomia y Astrofisica*, vol. 27, pages 58–62, August 2004.
- A. V. Sweigart and P. G. Gross. Evolutionary sequences for red giant stars. *Astrophysical Journal Supplement Series*, 36:405–437, March 1978. doi: 10.1086/190506.
- B. M. Tinsley. Chemical evolution in the solar neighborhood. II - Statistical constraints, finite stellar lifetimes, and inhomogeneities. *Astrophysical Journal*, 208:797–811, September 1976. doi: 10.1086/154666.
- B. A. Twarog. The chemical evolution of the solar neighborhood. I - A bias-free reduction technique and data sample. *Astrophysical Journal Supplement Series*, 44:1–29, September 1980. doi: 10.1086/190683.

- University of Waikato. WEKA: Data Mining Software in Java. World Wide Web electronic publication. URL <http://www.cs.waikato.ac.nz/ml/weka/>.
- A. Vallenari, S. Pasetto, G. Bertelli, C. Chiosi, A. Spagna, and M. Lattanzi. Kinematics and stellar content of the Milky Way populations toward the North Galactic Pole. *Astronomy and Astrophysics*, 451:125–139, May 2006. doi: 10.1051/0004-6361:20054712.
- F. van Leeuwen, editor. *Hipparcos, the New Reduction of the Raw Data*, volume 350 of *Astrophysics and Space Science Library*, 2007.
- Ž. Ivezić, B. Sesar, M. Jurić, N. Bond, J. Dalcanton, C. M. Rockosi, B. Yanny, H. J. Newberg, T. C. Beers, C. Allende Prieto, R. Wilhelm, Y. S. Lee, T. Sivarani, J. E. Norris, C. A. L. Bailer-Jones, P. Re Fiorentin, D. Schlegel, A. Uomoto, R. H. Lupton, G. R. Knapp, J. E. Gunn, K. R. Covey, J. A. Smith, G. Miknaitis, M. Doi, M. Tanaka, M. Fukugita, S. Kent, D. Finkbeiner, J. A. Munn, J. R. Pier, T. Quinn, S. Hawley, S. Anderson, F. Kiuchi, A. Chen, J. Bushong, H. Sohi, D. Haggard, A. Kimball, J. Barentine, H. Brewington, M. Harvanek, S. Kleinman, J. Krzesinski, D. Long, A. Nitta, S. Snedden, B. Lee, H. Harris, J. Brinkmann, D. P. Schneider, and D. G. York. The Milky Way Tomography with SDSS. II. Stellar Metallicity. *The Astrophysical Journal*, 684:287–325, September 2008. doi: 10.1086/589678.
- P. Westera, T. Lejeune, R. Buser, F. Cuisinier, and G. Bruzual. A standard stellar library for evolutionary synthesis. III. Metallicity calibration. *Astronomy and Astrophysics*, 381:524–538, January 2002. doi: 10.1051/0004-6361:20011493.
- R. Wielen. The kinematics and ages of stars in Gliese’s catalogue. *Highlights of Astronomy*, 3: 395–407, 1974.

Appendix A

Appendix A: Constant vs. decreasing SFR

This appendix is a part of the discussion made in the section 5.2.2. We present here the results obtained with our new default model when a constant and decreasing exponential SFR of Aumer and Binney (2009) were tested along with six representative IMF (Haywood et al. (1997a), Haywood-Robin, Vallenari et al. (2006), Kroupa (2008), Just and Jahreiß (2010) and Kroupa-Haywood v6). In Fig. A.1, A.2, A.3, A.4, A.5 and A.6 we show the $(B-V)_T$ distribution towards our three established regions and in Fig. A.7 and A.8 the fitting of synthetic LF produced by all mentioned combinations. As it is discussed in section 5.2.2 constant SFR produces too many bright objects no matter which IMF have been used.

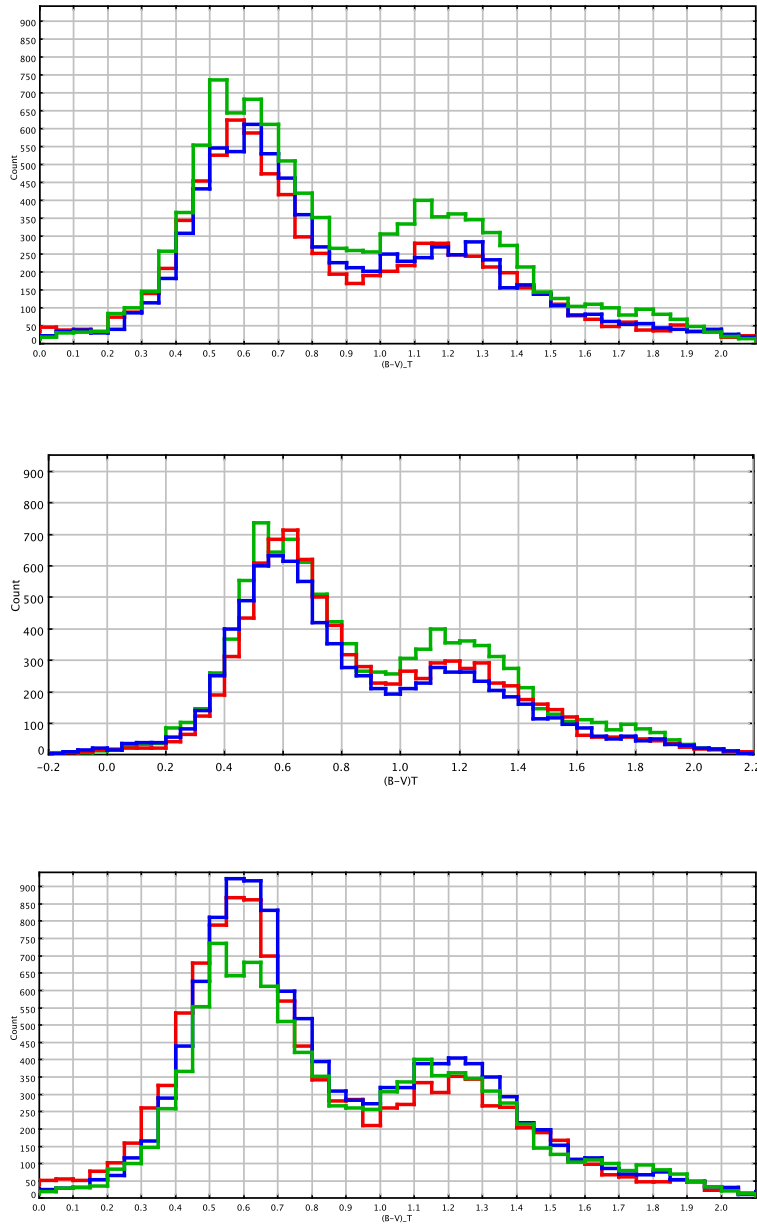


Figure A.1: $(B - V)_T$ distribution towards the Galactic North Pole, where we compare simulations obtained with constant SFR (red) and a decreasing exponential SFR of Aumer and Binney (2009) (blue). In green Tycho-2 data, the top panel corresponds to Kroupa (2008) IMF, in the middle Haywood-Robin IMF and at the bottom Just and Jahreiß (2010) IMF.

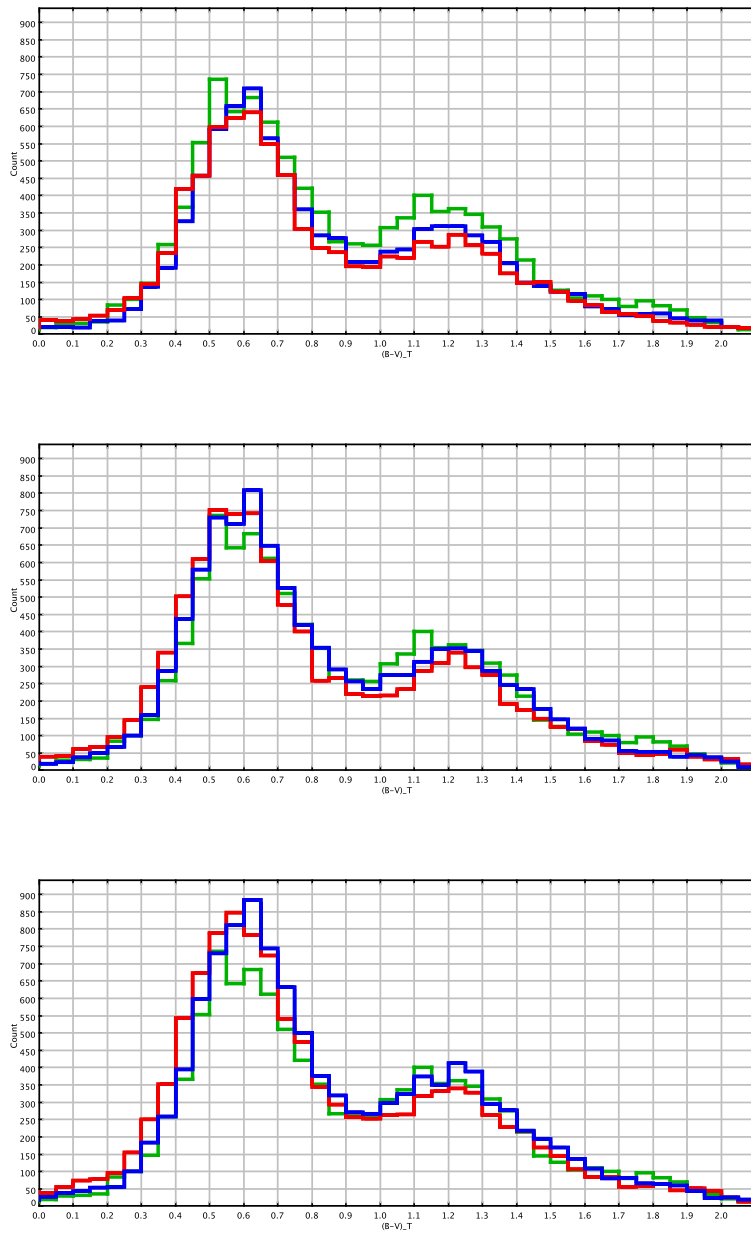


Figure A.2: $(B - V)_T$ distribution towards the Galactic North Pole, where we compare simulations obtained with constant SFR (red) and a decreasing exponential SFR of Aumer and Binney (2009) (blue). In green Tycho-2 data, the top panel corresponds to Haywood et al. (1997a) IMF, in the middle Kroupa-Haywood v6 IMF and at the bottom Vallenari et al. (2006) IMF.

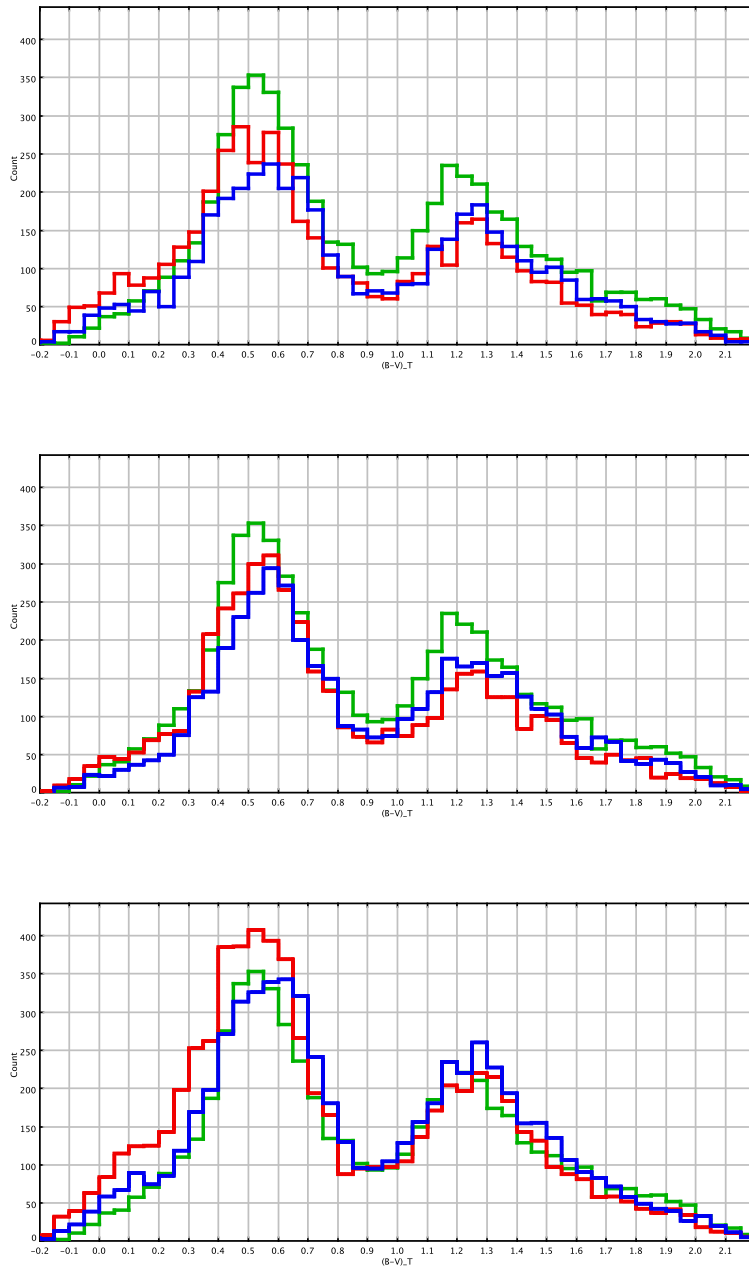


Figure A.3: $(B - V)_T$ distribution of the region 2 corresponding to the intermediate latitudes, where we compare simulations obtained with constant SFR (red) and a decreasing exponential SFR of Aumer and Binney (2009) (blue). In green Tycho-2 data, the top panel corresponds to Kroupa (2008) IMF, in the middle Haywood-Robin IMF and at the bottom Just and Jahreiß (2010) IMF.

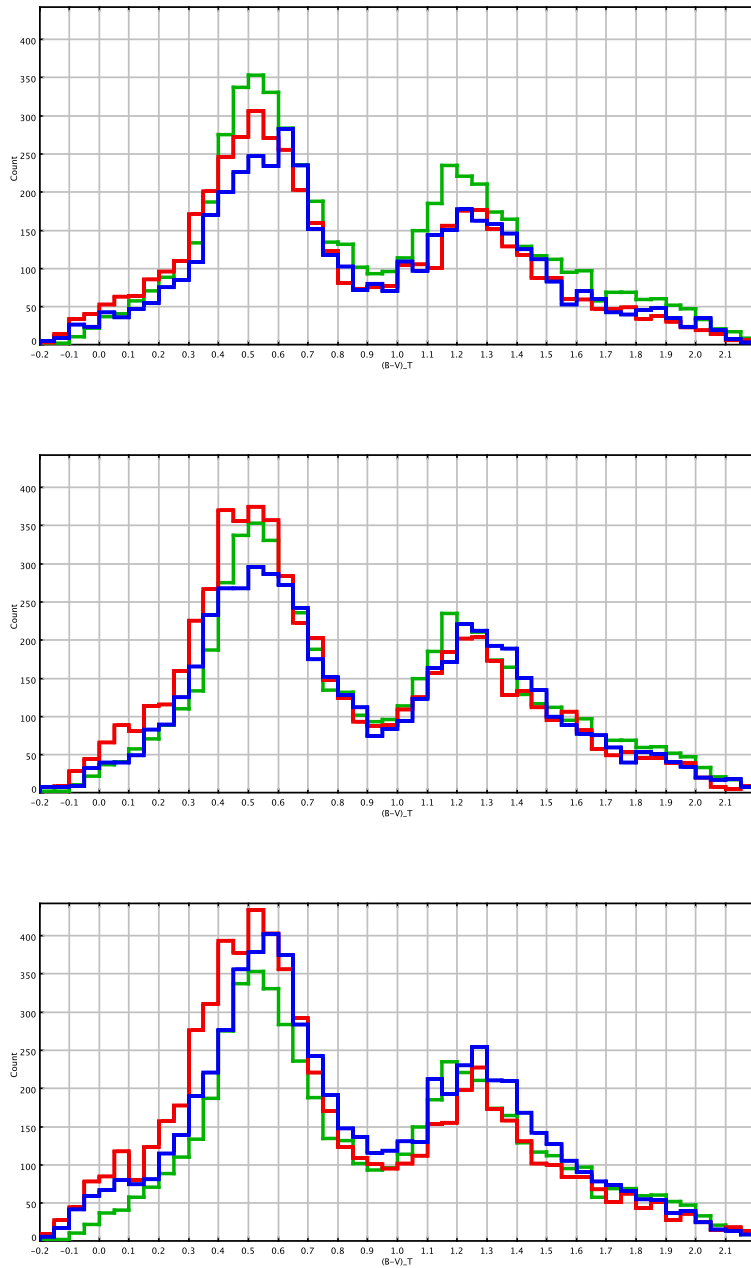


Figure A.4: $(B - V)_T$ distribution of the region 2 corresponding to the intermediate latitudes, where we compare simulations obtained with constant SFR (red) and a decreasing exponential SFR of Aumer and Binney (2009) (blue). In green Tycho-2 data, the top panel corresponds to Haywood et al. (1997a) IMF, in the middle Kroupa-Haywood v6 IMF and at the bottom Vallenari et al. (2006) IMF.

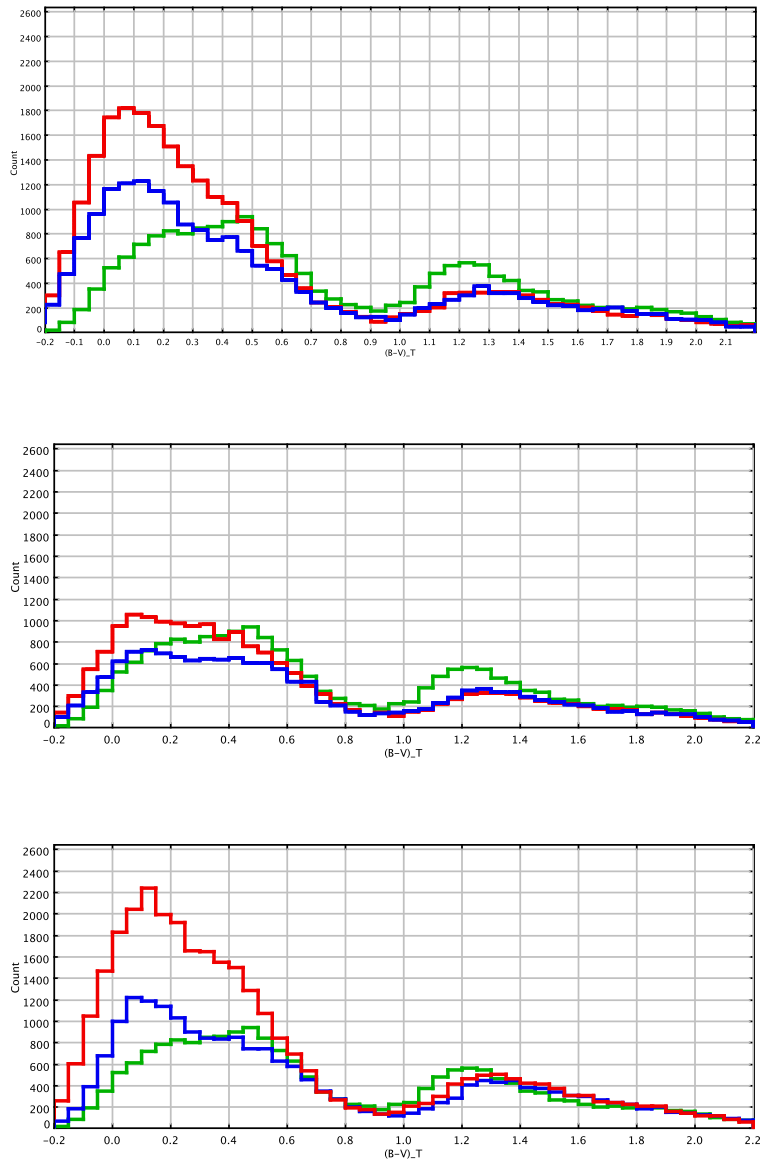


Figure A.5: $(B - V)_T$ distribution of region 3 within the plane, where we compare simulations obtained with constant SFR (red) and a decreasing exponential SFR of Aumer and Binney (2009) (blue). In green Tycho-2 data, the top panel corresponds to Kroupa (2008) IMF, in the middle Haywood-Robin IMF and at the bottom Just and Jahreiß (2010) IMF.

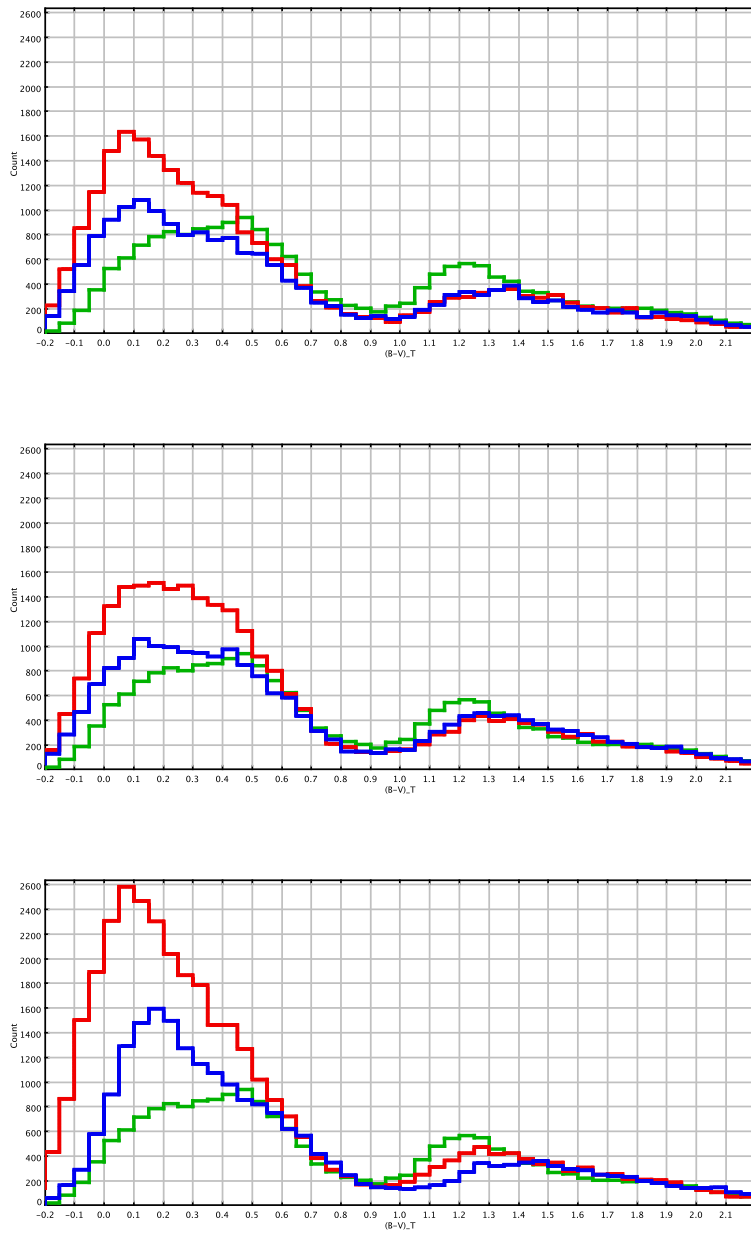


Figure A.6: $(B - V)_T$ distribution of region 3 within the plane, where we compare simulations obtained with constant SFR (red) and a decreasing exponential SFR of Aumer and Binney (2009) (blue). In green Tycho-2 data, the top panel corresponds to Haywood et al. (1997a) IMF, in the middle Kroupa-Haywood v6 IMF and at the bottom Vallenari et al. (2006) IMF.

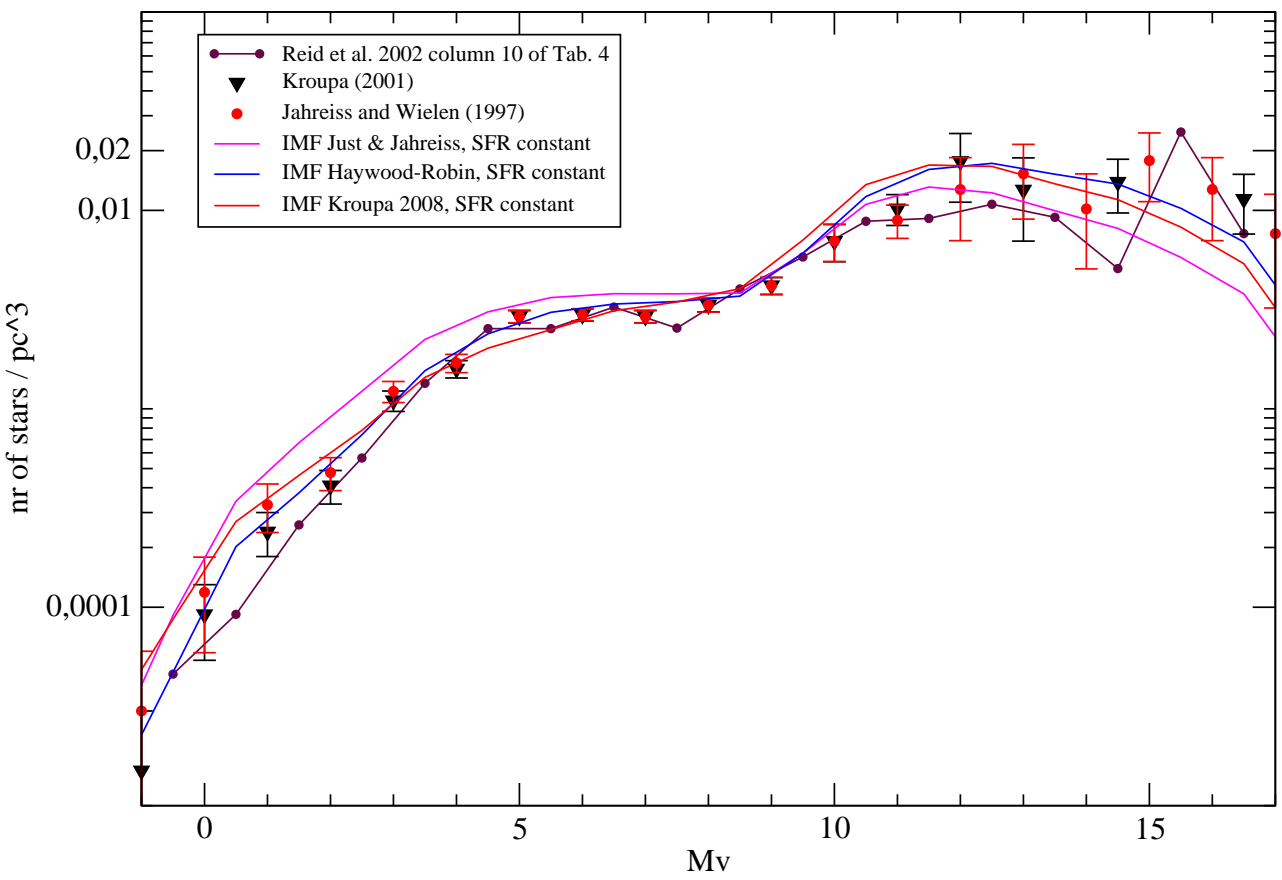


Figure A.7: Fitting the observed LF with the synthetic LF obtained with our default model where constant SFR was applied together with three different IMF.

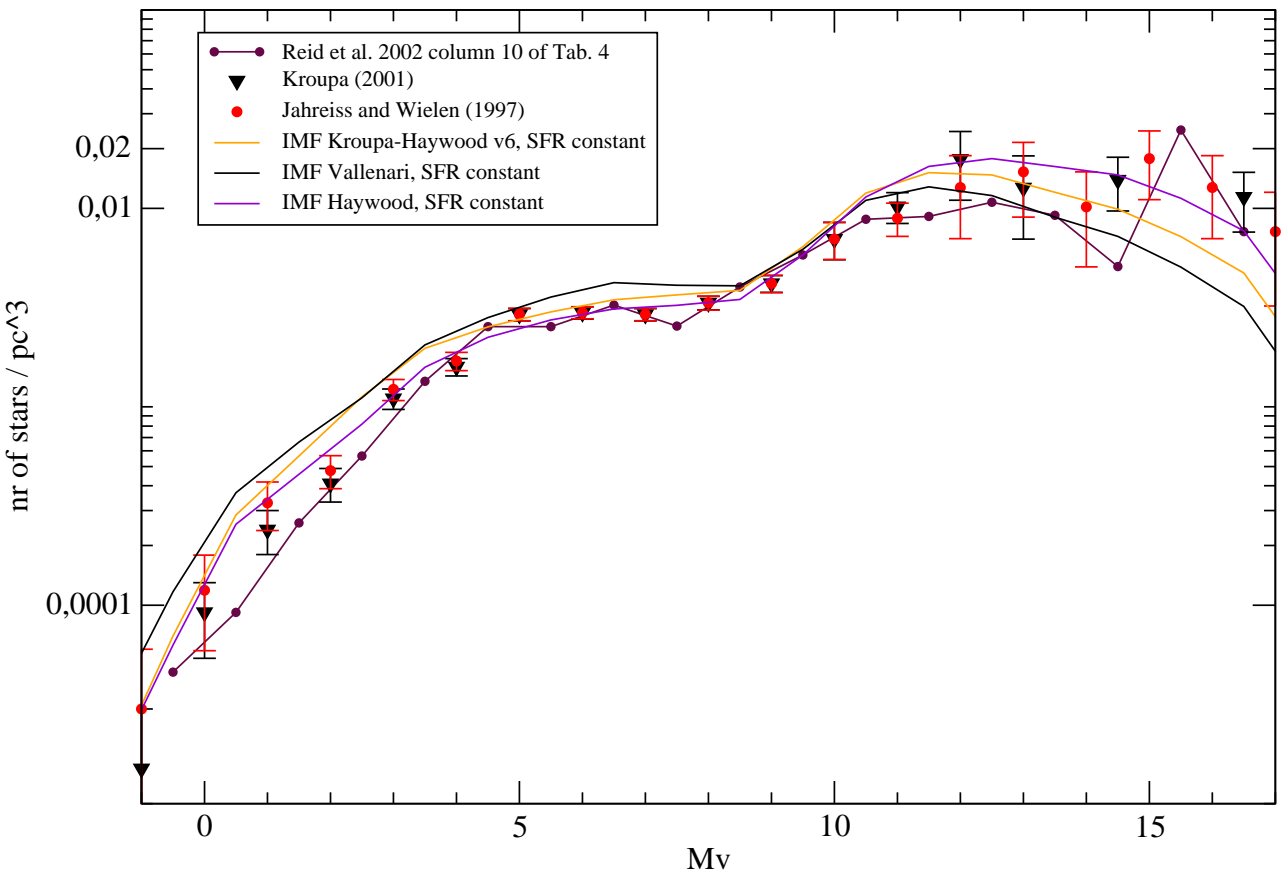


Figure A.8: Fitting the observed LF with the synthetic LF obtained with our default model where constant SFR was applied together with three different IMF.

Appendix B

Appendix B: Kroupa-Haywood IMF vs. Tycho-2

In this appendix we present the results of our simulations when the decreasing exponential SFR of Aumer and Binney (2009) was combined with Kroupa (2008) IMF and the five versions of Kroupa-Haywood IMF presented in section 3.1. These results are the part of the discussion about the best fit IMF and SFR made in the section 5.2.2. It has to be reminded that all simulations presented here were done using our default model, whose ingredients are presented in Table 5.1 and that IMF and SFR were the only inputs which have varied. Thus all simulations presented here contain binaries. The full discussion about each IMF presented here can be found in section 5.2.2. Here we will summarize that among the six presented IMF, Kroupa-Haywood v6 turns out to give the best fit to Tycho-2 $(B - V)_T$ distributions at all latitudes. This IMF also fits the local LF.

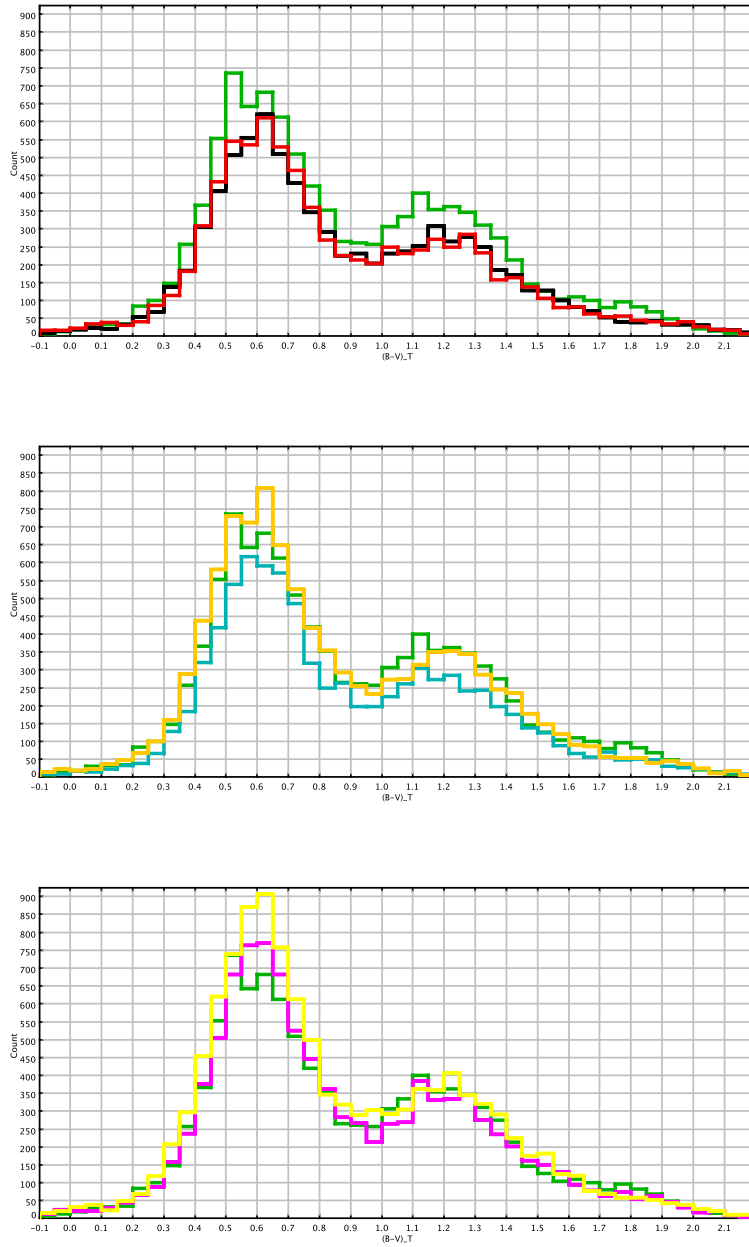


Figure B.1: $(B - V)_T$ distribution towards the Galactic North Pole. In green Tycho-2 data, in red simulations with Kroupa 2008 IMF, in black Kroupa-Haywood v1 IMF, in light blue Kroupa-Haywood v4 IMF, in orange Kroupa-Haywood v6 IMF, in magenta Kroupa-Haywood v7 IMF and in yellow Kroupa-Haywood v8 IMF. In all models we have imposed a decreasing exponential SFR of Aumer and Binney (2009).

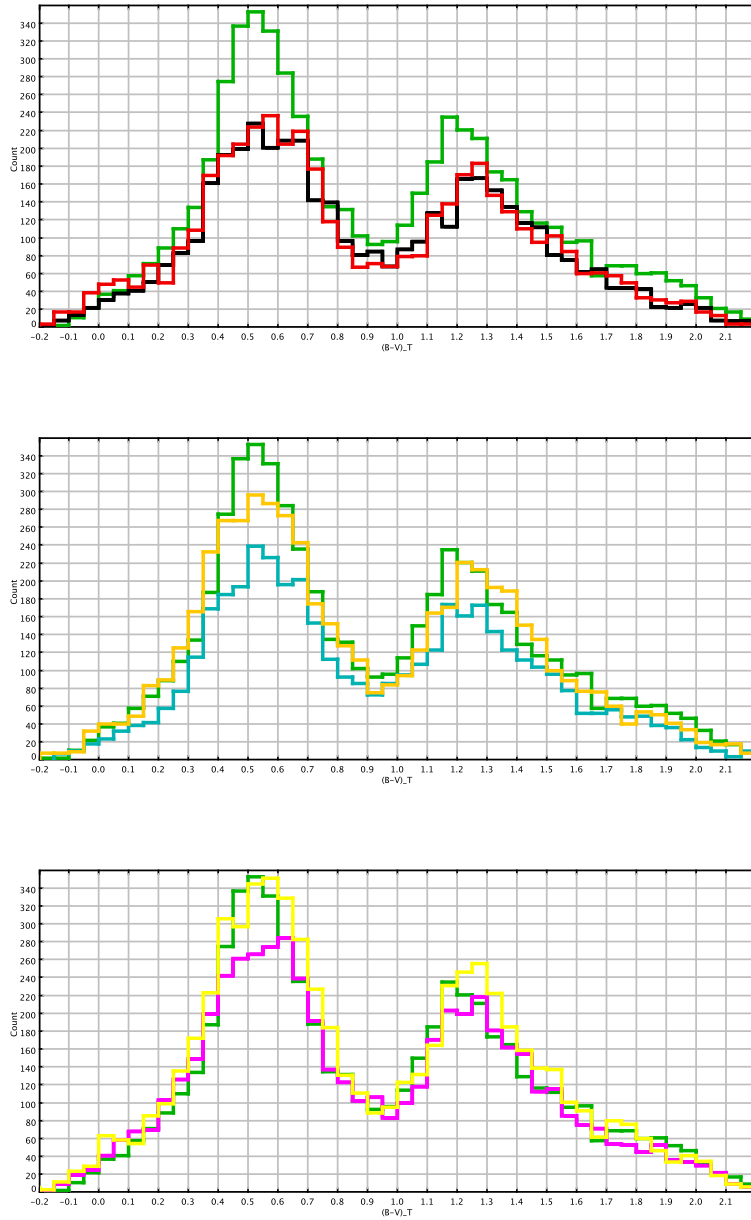


Figure B.2: $(B - V)_T$ distribution of the region 2 corresponding to the intermediate latitudes. In green Tycho-2 data, in red simulations with Kroupa 2008 IMF, in black Kroupa-Haywood v1 IMF, in light blue Kroupa-Haywood v4 IMF, in orange Kroupa-Haywood v6 IMF, in magenta Kroupa-Haywood v7 IMF and in yellow Kroupa-Haywood v8 IMF. In all models we have imposed a decreasing exponential SFR of Aumer and Binney (2009).

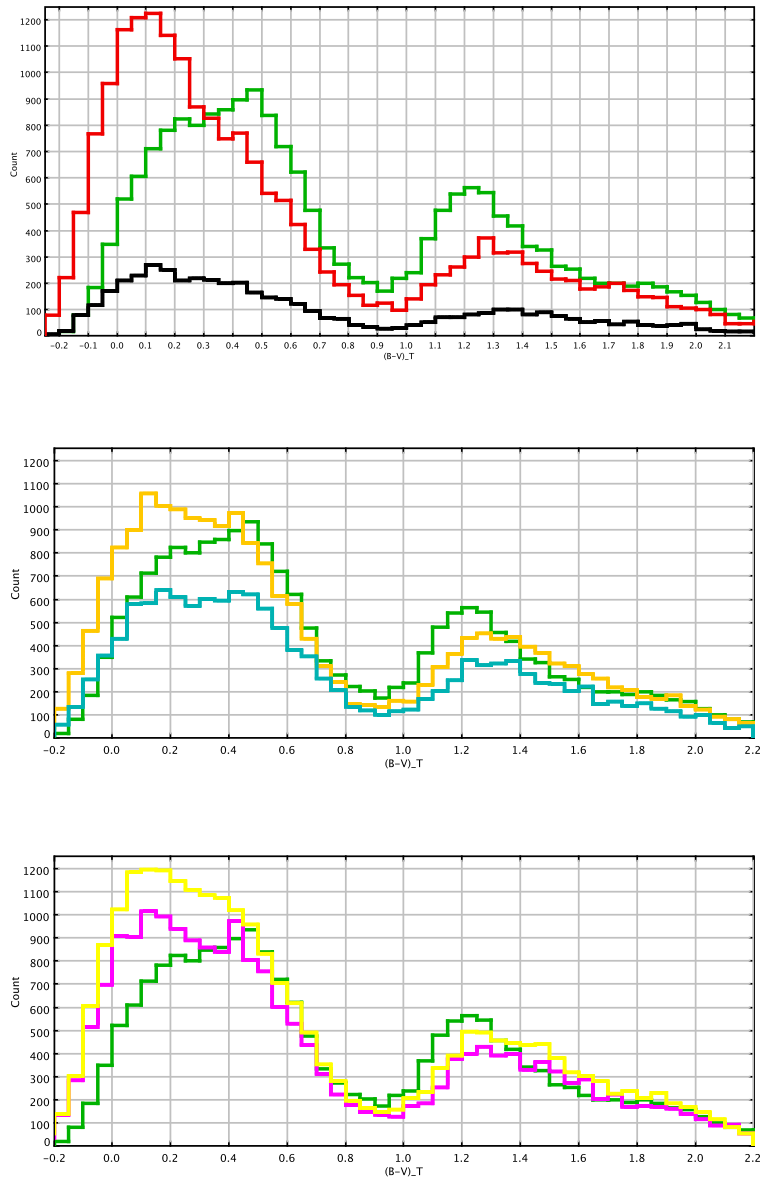


Figure B.3: $(B - V)_T$ distribution of the region 3. In green Tycho-2 data, in red simulations with Kroupa 2008 IMF, in black Kroupa-Haywood v1 IMF, in light blue Kroupa-Haywood v4 IMF, in orange Kroupa-Haywood v6 IMF, in magenta Kroupa-Haywood v7 IMF and in yellow Kroupa-Haywood v8 IMF. In all models we have imposed a decreasing exponential SFR of Aumer and Binney (2009).

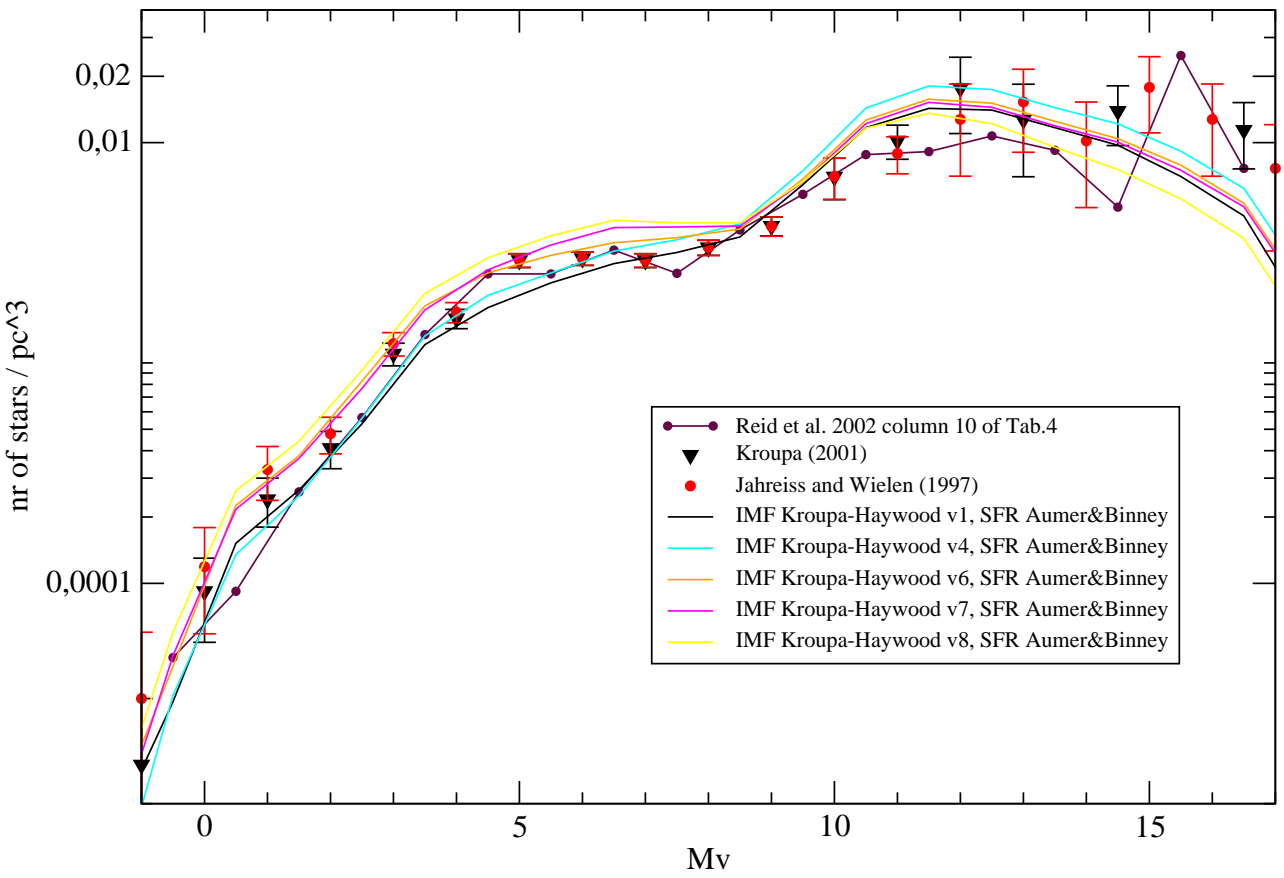


Figure B.4: Fitting the observed LF with the synthetic LF obtained with our default model and five different versions of Kroupa-Haywood IMF.